

Seismic Evaluation of Existing Stone Unreinforced Masonry Walls Using
Predictive Parameters for Strengthening Interventions

Hassan Ayoubi

A Thesis
in
The Department
of
Building, Civil, and Environmental Engineering

Presented in Partial Fulfillment of the Requirements
for the Degree of Master of Applied Science in Civil Engineering at
Concordia University
Montreal, Quebec, Canada

August 2021

© Hassan Ayoubi, 2021

CONCORDIA UNIVERSITY

School of Graduate Studies

This is to certify that the thesis prepared

By: Hassan Ayoubi

Entitled: Seismic Evaluation of Existing Stone Unreinforced Masonry Walls Using
Predictive Parameters for Strengthening Interventions

and submitted in partial fulfillment of the requirements for the degree of

Master of Applied Science in Civil Engineering

complies with the regulations of the University and meets the accepted standards with respect to originality and quality.

Signed by the final Examining Committee:

<u>Khaled Galal</u> <i>Chair's name</i>	Chair
<u>Dr. M. Packirisamy</u> <i>Examiner's name</i>	Examiner
<u>Dr. Anjan Bhowmick</u> <i>Examiner's name</i>	Examiner
<u>Dr. Lucia Tirca</u> <i>Supervisor's name</i>	Supervisor
<u>Dr. Ashutosh Bagchi</u> <i>Supervisor's name</i>	Supervisor

Approved by Dr. Michelle Nokken
Chair of Department or Graduate Program Director

August 8, 2021 Dr. Mourad Debbabi
Dean of Faculty

ABSTRACT

Seismic Evaluation of Existing Stone Unreinforced Masonry Walls Using Predictive Parameters for Strengthening Interventions

Hassan Ayoubi

The seismic evaluation of existing unreinforced masonry (URM) structures is deemed essential due to their historical value and the vulnerability they present when subjected to earthquake shaking. Most of these buildings, constructed in the last century, do not comply with the current seismic codes and masonry standard. This study focusses on the assessment of URM walls subjected to lateral loading and more in detail to the behaviour of structural components such as the piers and spandrels. The behavior of structural elements, comprising the shear and bending failure modes, are investigated; these failure modes can be detected through the crack propagation initiated in building's masonry walls. Then, a parametric study on a series of capacity formulations of piers and spandrels is performed and each failure mode is investigated independently in the aim of assessing the accuracy in capturing their strength. Three experimental test data are used to validate the efficiency of formulations for diagonal shear and data from five testing programs are used to validate the proposed formulations used to predict the maximum shear force resulting from flexural behavior of piers. Subsequently, a deterministic model for piers is built using an open-source software to generate data required to build a linear relationship between different parameters and the performance criteria expressed in terms of strength and ductility. A case study comprising an URM facade wall of an existing 2-storey school building in Montreal is also conducted and certain strengthening interventions are presented. Further, the generated data is used to build probabilistic models that operates on Bayesian Networks. Nonlinear analysis using the target and the predictive variables are carried out. Machine learning algorithms are applied to acquire the entropy reduction factors which helps determining the most predictive variables used to assess the performance of piers.

Acknowledgements

I would like to thank my Supervisors Dr. Lucia Tirca and Dr. Ashutosh Bagchi for guiding me through this process. The financial support provided by Concordia University and IC-Impacts Research Centre of Excellence Network Canada is gratefully acknowledged. I would like to thank the Congregation of Notre Dame, the owner of Villa Maria Building, and architect Keven Blondin for their generous support in the project. Finally, I would like to thank my friends and family for helping me go through this journey.

TABLE OF CONTENTS

List of Figures	viii
List of Tables	x
Chapter 1: Introduction.....	1
1.1 General / Background.....	1
1.2 Objective and Scope.....	1
1.3 Methodology in Brief.....	2
1.4 Thesis Organization.....	3
Chapter 2: Literature Review.....	5
2.1 General review	5
2.1.1 Complexity of Historical Masonry Buildings.....	5
2.1.2 Levels of Experimental Testing on Masonry Walls	7
2.2 Modeling and Analysis of Masonry Buildings under Seismic Loads.....	10
2.2.1 Modelling Approaches.....	10
2.2.2 Collapse Mechanisms in Masonry Buildings	11
2.2.3 Types of Analysis	12
2.2.4 Modeling Examples and Comparisons	13
2.2.5 Example of damage assessment of URM churches	16
2.3 Probabilistic Model Using Bayesian Networks and Machine Learning	20
2.3.1 Probability in machine learning.....	20
2.3.2 Bayesian Interpretation	20
2.3.3 Independency and the Chain Rule	23
2.3.4 Random Variables: Discrete, Continuous, and Density Functions.....	25
2.3.5 Discretization Functions	25
2.3.6 Mutual Information and Entropy Reduction.....	27

2.3.7	Supervised Machine Learning Algorithms	28
2.4	URM structures in Montreal and Failure Mechanisms	29
2.4.1	Seismic Data in Montreal.....	30
2.4.2	Assessment of Existing Structures Using Macro Modeling Approaches	33
Chapter 3:	Preliminary Parametric Study on the Shear and Flexural Capacity Simplified Formulations for URM Walls	44
3.1	Shear and Flexure Dominant Behavior in Masonry Pier Elements	44
3.1.1	Diagonal Shear Mode	45
3.1.2	Rocking and Toe Crushing Flexural Modes	47
3.2	Validation of the Formulations	48
3.2.1	Experimental Data for Testing the Shear Capacity.....	49
3.2.2	Experimental Campaign for Flexural Capacity	62
3.3	Shear and Flexural dominant behavior in Spandrels Elements.....	78
3.3.1	Parameters for Masonry Spandrels	81
3.3.2	Capacity Equations for Shear Dominant Failure	82
3.3.3	Capacity Equations for Flexure Dominant Failure	83
3.3.4	Parametric Analysis of the Shear Failure Mode	84
3.3.5	Parametric Analysis of the Flexural Failure Mode	89
3.4	Results	91
3.4.1	Pier Analysis	91
3.4.2	Spandrel Analysis	95
Chapter 4:	URM Capacity Estimation Using Distributed Plasticity Models for Linear Data Correlations	97
4.1	Distributed Plasticity Model.....	97
4.1.1	Numerical Model Using OpenSees.....	97
4.1.2	Model Calibration & Validation	100

4.2	Data Generation and Linear Correlation of Parameters for Strengthening Interventions	107
4.2.1	Correlations for Shear Dominant Failure Mode	107
4.2.2	Correlations for Flexural Dominant Failure Mode	110
4.3	Case Study - Piers Extracted from the Facade Wall of Villa Maria School Building .	114
4.3.1	Villa Maria School - Extraction of Parameters Using Available Resources	115
4.3.2	Preliminary Experimental Tests on Lime Mortar	118
4.3.3	Villa Maria School - Extraction of Parameters Using Available Resources	123
4.3.4	Distributed Plasticity Model in OpenSees	125
Chapter 5: Nonlinear Probabilistic Model and Machine Learning Approach to Parameter Identification for URM Piers Strengthening.....		
5.1	Data generation and curation.....	129
5.2	Nonlinear Probability Model and Acyclic Graphs	134
5.2.1	Model of the Shear dominant Behavior in Piers.....	134
5.2.2	Model of the Flexural dominant Behavior in Piers.....	143
5.3	Nonlinear Data Analysis and Wall Performance	149
5.4	Case Study: Performance Analysis of the Piers Based on the Linear and Nonlinear Data Analysis Models.....	153
5.4.1	Information for Pier1 with Shear Dominant Behavior	153
5.4.2	Information for Pier2 with Flexural Dominant Behavior	155
Chapter 6: Conclusions, Limitations and Scope for Future Work.....		
6.1	Conclusions.....	157
6.2	Limitations	160
6.3	Scope for Future Work.....	163
References		168
Appendix A		188

List of Figures

- Figure 2.1: Cross sections of different masonry walls in Italy showing the complexity of stone types, mortar, number of layers, and the thickness of wall (Penna, 2015).
- Figure 2.2: Prism test using two bricks (Churilov et al., 2012).
- Figure 2.3: Venn diagrams for two set of events E_1 and E_2
- Figure 2.4: The connection between parent and child nodes creating the conditional probability.
- Figure 2.5: The intersection of the two sets E_i and A and the application of product rule
- Figure 2.6: The nodes included within the Markov Blanket for the target variable shown within the circumference of the circle.
- Figure 2.7: The Western Quebec Seismic Zone showing the historical seismic activity in the region (NBCC 2015).
- Figure 2.8: Soil classifications for Montreal area (Rosset & Chouinard, 2009)
- Figure 2.9: Relative seismic hazard in Quebec for 1-2 story structures (NBCC 2015).
- Figure 2.10: Equivalent frame discretization
- Figure 2.11: Failure mechanisms that occur in masonry piers due to lateral and vertical loads. a-Diagonal shear, b-Sliding shear, c-Flexural rocking, d-Toe crushing.
- Figure 3.1: a) Shear capacities versus vertical stresses for specimens A1 and A2 b) B1 and B2 c) WS prototypes d) WI prototypes e) WR prototypes f) SW prototypes.
- Figure 3.2: a) The variation of shear capacities with the vertical stress levels for samples FS-NI b) FS-I c) S-NI d) S-I e) H1 and H2 f) H2, H3 and H4 g) H2, H5, H6 and H7.
- Figure 3.3: a) Shear capacities versus the vertical stresses in samples P3 and P4 b) 10-A and 10-B c) 10-B & 10-C d) CL6 and CS5 e) CS5 and CS6 f) CS7 and CS8 g) CS5 and CS7 h) CS6 & CS8.
- Figure 3.4: a) Flexural cracks in a spandrel and b) Shear cracks in a spandrel
- Figure 3.5: a) Shear and moment diagrams following the force distribution in spandrels b) Distribution of plastic hinges in an equivalent frame model.
- Figure 3.6: a) Variation of shear force w.r.t. axial force in spandrels W2 & W3 b) thickness of lintels in spandrels W3 & W4 c) length of spandrels S1 & S2 d) height of spandrels S1, S3, S4 & S6.
- Figure 3.7: a) Indices for the four capacity formulations regarding aspect ratios b) stone textures c) vertical stresses d) scale factors
- Figure 3.8: a) Indices for the five capacity formulations regarding the aspect ratios b) boundary conditions
- Figure 3.9: a) Indices for the five capacity formulations regarding the vertical stresses b) typology c) wall thicknesses d) scale factors e) mortar injection
- Figure 4.1: Fiber section discretization
- Figure 4.2: Coupling of shear law into the fiber section
- Figure 4.3: Concrete02 material as defined in OpenSees (McKenna et al., 2000)
- Figure 4.4: Hysteretic material as defined in OpenSees (McKenna et al., 2000)
- Figure 4.5: A) squat pier; B) slender pier as tested after Anthoine et al.(1994)
- Figure 4.6: Constitutive law for Concrete02 for piers A and B
- Figure 4.7: The difference between the total response and the flexural response in the squat pier
- Figure 4.8: Constitutive law for Hysteretic material after calibration
- Figure 4.9: Response of the squat pier to the cyclic loading dominated by shear behavior.
- Figure 4.10: Response of the slender pier to cyclic loading dominated by flexural behavior.
- Figure 4.11: a) Variation of D_{max} and D_{ult} w.r.t the height b) V_{max} w.r.t. vertical forces c) D_{max} w.r.t. length d) V_{max} w.r.t. length e) D_{max} w.r.t. thickness f) V_{max} w.r.t. thickness
- Figure 4.12: a) Variation of V_{max} w.r.t. height b) V_{max} w.r.t. compressive strength.
- Figure 4.13: a) Variation of V_{max} w.r.t. tensile strength b) V_{max} and V_{ult} w.r.t. elastic tension modulus c) V_{max} w.r.t. vertical forces d) V_{max} w.r.t. length
- Figure 4.14: Variation of maximum base shear strength V_{max} with the thickness of the pier
- Figure 4.15: The central building of Villa Maria high school (main facade)
- Figure 4.16: Villa-Maria school elevation
- Figure 4.17: Main floor plan for Villa Maria school

Figure 4.18: Second floor plan for the Villa Maria school

Figure 4.19: Facade wall of the Villa Maria school with extracted dimensions in meters

Figure 4.20: a) NHL hydraulic lime used in the mix of mortar b) Sand used in the mortar

Figure 4.21: a) Mixing the mortar using a mechanical turbine b) ASTM certified molds c) Tapping the mortar at half the portion d) Finishing the surface of the mortar e) Curing f) Weight measuring.

Figure 4.22: a) Measuring the dimensions b), c) Compressive strength test d) Typical failure in the mortar cubes.

Figure 4.23: a) Limestone masonry samples collected from the field near the building prepared for density test b) Measurement of the weight in water using a chain hooked to the weight balance.

Figure 4.24: Illustration of pier1 (left) and pier2 (right) selected from the facade wall.

Figure 4.25: The cyclic behavior of Pier1

Figure 4.26: The cyclic behavior of Pier2

Figure 5.1: a) Frequency of V_{max} in terms of specified intervals b) PDF of V_{max} c) CDF of V_{max} d) Frequency of V_{max} for the specified intervals e) PDF of V_{max} f) CDF of V_{max} .

Figure 5.2: a) Data scatter for V_{max} versus N for the shear dominant behavior b) vs t for the shear dominant behavior c) vs f_t for the shear dominant behavior d) vs N for the flexural dominant behavior e) vs H/L for the flexural dominant behavior

Figure 5.3: Discretization of the variables and the different functions used.

Figure 5.4: Model using Naive Bayes Network with the mutual information.

Figure 5.5: a) Markov Blanket b) Aug. Markov Blanket c) SC vs structure/target precision ration for the Markov Blanket d) SC vs structure/target precision ration for the Aug. Markov Blanket model e) Markov Blanket with $SC=0.22$ f) Aug. Markov Blanket with $SC=0.175$

Figure 5.6: a) Performance of Naive Bayes model b) Markov Blanket c) Aug. Markov Blanket d) Marginal probabilities for the variables in the Markov Blanket

Figure 5.7: a) Scatter points for ductility factor and H b) ductility factor and L

Figure 5.8: Manual discretization of the ductility factor using the PDF b) SC for Markov Blanket vs structure/target precision.

Figure 5.9: Acyclic graph for the Markov Blanket model b) Performance of the Markov Blanket model

Figure 5.10: Discretization of the variables for the flexural dominant behavior of the piers

Figure 5.11: Naive Bayes Network

Figure 5.12: a) Markov Blanket model b) Markov Blanket model with $SC=0.2125$

Figure 5.13: a) Augmented Markov Blanket model b) Augmented Markov Blanket model with $SC = 0.24$

Figure 5.14: a) SC for the Markov Blanket model b) SC for the Aug. Markov Blanket model.

Figure 5.15: a) Performance of the Naive Bayes b) Markov Blanket c) Aug. Markov Blanket d) Marginal probabilities for Aug. Markov Blanket model

Figure 5.16: Indices for entropy reduction for the target variable V_{max} for shear dominant behavior

Figure 5.17: Indices for entropy reduction for the target variable μ for shear dominant behavior

Figure 5.18: Indices for entropy reduction for the target variable V_{max} for flexural dominant behavior

Figure 5.19: a) Probability distribution for V_{max} with the existing parameters extracted from Pier1 b) after the improvement of the factor f_t .

Figure 5.20: a) Probability distribution of μ with the existing parameters extracted from Pier1 b) after the improvement of the factor f_t .

Figure 5.21: a) Probability distribution of the variable V_{max} with the existing parameters of Pier2 b), c) after the improvement of f_t d) after the improvement of t .

List of Tables

- Table 3.1: Preliminary mechanical parameters for masonry assemblages*
- Table 3.2: Geometry, vertical stresses, and capacity results from the experimental tests on piers*
- Table 3.3: Results of maximum shear, ultimate and yielding displacement ratios and shear capacity ratios resulting from the formulations.*
- Table 3.4: Variation of capacity shear indices and divergence factors in terms of the different parameters for each specimen*
- Table 3.5: Preliminary mechanical parameters for masonry assemblages*
- Table 3.6: Geometry, vertical stresses, and capacity results from the experimental tests on piers*
- Table 3.7: Results of maximum shear, ultimate and yielding displacement ratios and shear capacity ratios resulting from the formulations.*
- Table 3.8: Variation of capacity shear indices and divergence factors in terms of the different parameters of the piers*
- Table 3.9: Preliminary characterizations of the spandrels used in the full-scale experiment.*
- Table 3.10: Experimental results from the in-plane cyclic tests on the piers*
- Table 3.11: Results of maximum shear from the simplified formulations*
- Table 3.12: Mechanical properties of the masonry panels*
- Table 3.13: Experimental results from the in-plane cyclic tests on the piers*
- Table 3.14: Results of maximum shear from the simplified formulations*
- Table 3.15: Ratio of experimental to the numerical shear capacity values*
- Table 3.16: Data from the in-plane cyclic tests on the piers*
- Table 3.17: Mechanical parameters for the selected samples*
- Table 3.18: Numerical capacity values for spandrels associated with flexural failure.*
- Table 3.19: Ratio of experimental to the numerical shear capacity values*
- Table 4.1: Unreinforced masonry capacity formulations associated with shear behavior used to calibrate the numerical model.*
- Table 4.2: Hysteretic parameters after calibration to represent the shear behavior of the pier.*
- Table 4.3: Incremental displacements for the quasi-cyclic loading on the top of the pier*
- Table 4.4: The correlation values between the major parameters and the strength criteria of the piers with shear dominant behavior*
- Table 4.5: The correlation values between the major parameters and the strength criteria of the piers with flexural dominant behavior*
- Table 4.6: Different mortar to sand ratios used in the mix with their associated water to mortar ratios.*
- Table 4.7: Compressive strength for the three batches at 7 days*
- Table 4.8: Compressive strength results for three batches at 50 days*
- Table 4.9: Capacity formulations for shear dominant behavior*
- Table 4.10: Parameters needed to build the distributed plastic model in OpenSees*
- Table 5.1: Generated variables for the shear dominant behavior*
- Table 5.2: Generated variables for the flexural dominant behavior*
- Table 5.3: Indices based on mutual information for entropy reduction of the target variable V_{max} for the shear dominant behavior.*
- Table 5.4: Indices based on mutual information for entropy reduction of the target variable μ for the shear dominant behavior.*
- Table 5.5: Indices based on mutual information for entropy reduction of the target variable V_{max} for the flexure dominant behavior.*

Chapter 1: Introduction

1.1 General / Background

Understanding the lateral response of stone masonry structures under ground shaking events is a complex procedure. Experimental testing of stone masonry elements is expensive and structural modeling using advanced software requires experimental test results to calibrate numerical models. The factors that contribute to the structure's behaviour are the material quality, the construction type and year, the site class, and the ground motions characteristics. Analysing the behavior of masonry structures subjected to previous earthquake events, it helps to understand the probable failure mechanisms of these buildings. To preserve the simplicity of the analysis, macro-modeling techniques such as the equivalent frame method has proven to be a great substitute for more complex and time demanding procedures such as the finite element analysis or the micro-modeling techniques.

The motivation behind this work is to generate characteristic indices that describes the influence of certain parameters on the behavior of the structural elements in URM buildings.

1.2 Objective and Scope

The work in this thesis will cover the following areas:

- Performing a parametric study on the relationship between the available capacity formulations for unreinforced masonry walls (URM) and their characteristics to assess their performance on capturing the maximum base shear.

- Linear data assessment using correlation factors on URM piers to build a relationship between the wall characteristics and its performance.
- Nonlinear data assessment using mutual information factors and machine learning formulations through Bayesian networks applied to URM piers as an expansion of linear analysis.

An URM pier model is developed and calibrated based on experimental test results using the OpenSees software(McKenna et al., 2000) . The numerical model was particularly developed to replicate the in-plane cyclic behavior on stone masonry elements. The numerical model is the bases for data generation used in both the linear and nonlinear analysis, as well as, to investigate the impact of factors that influence the model behaviour. A case study of a low-rise stone masonry building located in Montreal is presented.

1.3 Methodology in Brief

For attaining the objectives, the following tasks would be performed:

- The information about piers is collected from a series of experimental tests used to extract parameters that influence the behavior. Four formulations for estimating the capacity representing the shear dominant behavior, and five formulations representing the flexural dominant behavior are collected from the literature and used for model calibration. Values extracted from the formulations are averaged and compared to the experimental values through ratio factors. The same work pattern is applied on spandrels, but no major conclusions are returned due to the shortage in the tests done on these elements.
- A model of two piers with a shear dominant behavior and flexural dominant behavior, respectively, are calibrated based on experimental tests using an equivalent frame method

with distributed plasticity. The two behavioral types are captured within the confinement of fiber element defined in OpenSees. Then, the models are used to generate data considering random variations of the characteristics of the walls under assessment which are utilized for the linear and nonlinear data analysis of the wall behavior.

- The linear analysis of the data uses a limited number of data points which is dependent only on the target variable, while the other parameters are fixed. As the correlation factors are extracted, it is feasible to extract the more influential variables on the performance of the piers measured in terms of base shear and displacement.
- The nonlinear analysis uses a large data set with many variables related to the target variable. After the discretization of the data, supervised machine learning algorithms dependent on the Bayesian networks are used to interpolate the connections between the variables and the corresponding mutual information that indicates the strength of their relationship. Those factors will indicate the most influential variables on the performance of the piers measured in terms of base shear and displacement. The advantage of the nonlinear data analysis is the more realistic approach due to the connections between those variables which are neglected in the linear data analysis.

1.4 Thesis Organization

The research work is arranged in six chapters. The first chapter is a brief introduction including the scope of work and the methodology. The second chapter is the literature review that explains about the existing unreinforced masonry structures and their complexity. It is given a summary of analysis types used in this study and reason behind the selection of the equivalent frame method. It also covers the seismic hazard for Montreal and the types of failure mechanisms of URM walls

(piers). Chapter three covers the parametric study performed on capacity formulations for the shear and flexural dominant behaviors in piers and spandrels. It shows comparison indices between the accuracy of those formulations and major characteristics of the structural elements. Chapter four presents the model calibration of two piers each experiencing a different mode of failure using OpenSees. The whole procedure used in the calibration and the determination of different parameters is presented. Using linear analysis, the most influential characteristic of the wall are identified. In the same chapter, a case study on Villa Maria School building in Montreal is shown including experimental testing on the mortar used to extract the compressive strength of the walls and the selection of the capacity formulation explained in chapter three. Chapter five includes the nonlinear data analysis conducted on two piers of different dimensions. A large data set was generated to apply the Bayesian networks needed to assess the mutual information and entropy reduction factors between the wall characteristics and the wall performance. Finally, chapter six presents conclusions based on the research presented below, and the future work.

Chapter 2: Literature Review

From the literature, an overview of the types of existing unreinforced masonry structures (URM) is presented along with the modeling approaches and collapse mechanisms associated with such buildings. It also describes the seismic hazard in Montreal with direct relevance to URM buildings of short period associated with low-rise construction. A detailed summary of equivalent frame models is presented showing all the failure modes. Different examples of surveys and experimental campaigns are presented to aid the descriptions and provide evidence for the findings of the presented research.

2.1 General review

2.1.1 Complexity of Historical Masonry Buildings

Masonry buildings are complex structures that have been used historically through subsequent centuries up to date. A wide variety of applications of masonry constructions span from small residential buildings to schools, museums, and churches. Over the time, these building structures survived environmental loads, as well as, human interventions caused by changes of occupancy or architectural interventions that, in general, reduce the number of interior walls and increase the number of walls with openings. Environmental exposure and lack of maintenance may have led to major changes in the properties of the material as well as the behavior of the whole structure. For example, earthquakes, settlements, storms, and structural modifications such as adding stories, extending floor areas, and partial reconstructions may lead to the use of different materials and methods of construction in the same building. Adding to the complexity issue, multi-leaf walls encompass hidden masonry stones which are not visible during site inspections or non-destructive tests and might vary from one wall to another due to the inadequacy of the construction. This will

impose many errors in the analysis of the building specially that the destructive tests are very limited due to the low capacity or due to the historical significance of masonry structures.

Another important parameter to be considered is the structure of wall's cross sections. According to a study in Italy, Binda et al., (2005) have emphasized the role of cross section in determining the response of the structure and the type of the failure associated with it. The study provides a classification of different cross sections including the mortar contribution with enhanced demonstration of the model shape, which stresses the importance of such study on the selection of repair procedures. Examples of masonry wall sections are illustrated in Fig. 2.1.

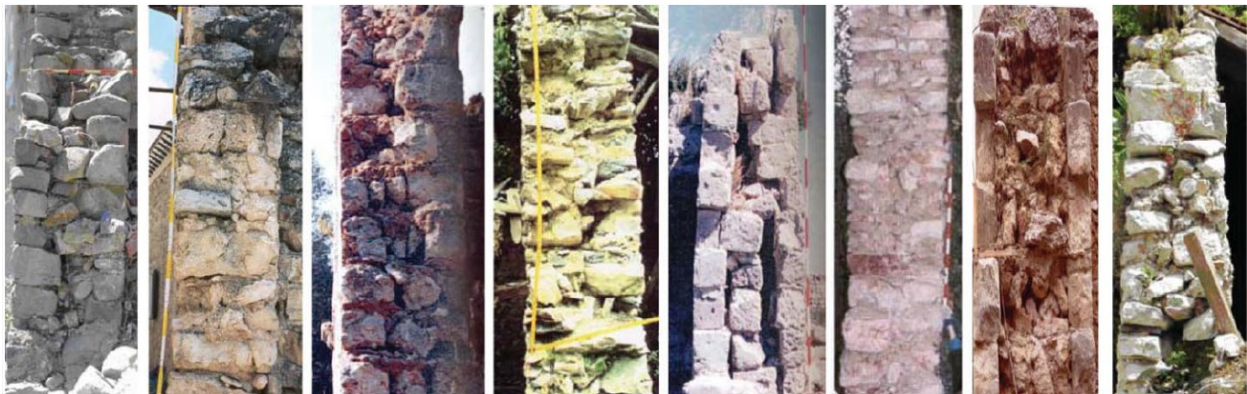


Figure 2.1: Cross sections of different masonry walls in Italy showing the complexity of stone types, mortar, number of layers, and the thickness of wall (Penna, 2015).

Many types of stones are used in masonry constructions. As such, three main stone categories are identified according to the source: 1) field stones that are random in shape and sizes and are usually used for infill between two walls; 2) rubble stones that are strong rocks (e.g., granite) and are used in undressed walls with irregular texture and thick mortar joints, and; 3) quarry stones that are more workable (e.g. sandstones) and are used in walls with regular texture and thin mortar joints. Stones perform well in compression but are weak in tension. Usually, they show a wide-ranging of mechanical properties that depends on the type and age of elements.

2.1.2 Levels of Experimental Testing on Masonry Walls

The variations of construction types of masonry buildings lead to the necessity for performing a wide set of experimental tests on masonry walls to determine the properties of each material used, and the behavior of structural elements within the building that contributes to the overall response mechanism. Tests on bricks and mortar conducted according to MKS standards were performed by Churilov & Dumova-Jovanoska, (2012). Geometrical measurements of brick units were done to calculate the unit weight and degree of porosity. A compression test on two bricks glued with cement was performed considering four array sets shown in Figure 2.2. An average compression strength of 10.8MPa, 4MPa, 6.4MPa and 6.1MPa on, respectively was obtained. Another test was conducted on cube shaped units and higher compression resistance was shown. A flexural tensile strength test is also carried out, but very low values reaching 0.9MPa mean average resulted from the four sets tested. For these tests, the mortar specimens were cured for 28 days and tested for tensile and compressive strengths using lime mortar as a common material for historical buildings, and cement mortar as reference samples. A significant difference in the results showing a very weak strength in tension and compression for lime mortar samples was obtained.



Figure 2.2: Prism test using two bricks (Churilov et al., 2012).

As part of the EUCENTRE project, characterization tests (Magenes et al., 2010) were conducted on specimens replicating the undressed double-leaf stone masonry walls that were typical for full-scale buildings. These tests included the vertical compression test and diagonal compression test

that were used to extract the elastic and plastic properties of the wall due to flexural and shear forces, respectively. The mechanical properties vary according to the through-wall connections, the material properties, and the construction quality considering the heterogeneity of the geometry and the material. Six specimens were chosen for each test with different dimensions after being cut from a large wall cured for 75 days (according to strength tests done on mortar cured for different days). Transducers were installed on specimens to calculate the strain in different direction (horizontal, vertical, transverse), while some specimens were set-up for compression forces applied vertical (vertical compression tests) and others for lateral forces to measure the diagonal compression. It was noticed that the test results were scattered, but still plausible in terms of comparison with other tests and codes such as Eurocode 8 and the Italian code. Within the same experimental campaign on masonry walls, an in-plane cyclic shear test (Magenes et al., 2010) have been conducted on five sample walls divided between two slenderness ratios corresponding to slender and squat piers, and two levels of axial loads corresponding to different number of stories. The diagonal shear failure was dominantly controlling the crack formations in most of the prototypes. Strength parameters, displacement capacities, and hysteretic energy dissipation properties were extracted to quantify the behavior of the piers. A bending rocking behavior occurred in the first slender specimen built with stronger mortar, without any evidence for sliding phenomenon taking place in any wall. Also cracks where correlated with the drift ratios showed an almost linear relation with an ultimate failure at a crack of 4-5mm.

A quasi-static cyclic load test was performed on two types of spandrels to compare their behavior (Graziotti et al., 2014). A test set-up was prepared to simulate the boundary conditions in the real prototypes. A full-scale H-specimen was loaded vertically and uplifted at the right pier to provide a statically determined model of a base rotation specimen. A compression force was provided to

the spandrel to simulate the action of steel ties. Two specimens were recognized one with thick and one with thin lintel beneath the spandrel. By increasing the drift (uplifting the pier) and applying a quasi-static cyclic load it resulted data to plot the shear-displacement diagram as well as the failure mechanism realized. In the first specimen (thick lintel) the spandrel showed diagonal shear failure with increase of shear forces till the end of the test. An elasto-plastic behavior was stated with well-defined yielding point. In the second specimen (thin lintel) a more diffusive diagonal shear failure was observed, with a sudden drop in the shear forces due to the dislocation of units which continued to a 70% drop at the end of the test. Obviously, the think lintel helped increased the energy dissipation in the spandrel beam.

In addition to the work done on spandrel samples under quasi-static cyclic loading and using the same set-up, two H specimen walls were tested to observe their behavior under seismic load (Graziotti et al., 2012). Both H walls have the same thick lintel beneath the spandrel. The first specimen was tested without any horizontal compression forces on the spandrel, while the second H wall specimen was tested considering a compression force applied on the spandrel that was decreased during the test. The first H wall showed flexural failure during the monotonic increase of drifts with cracks distributed along the interface between the spandrel and the piers. Plotting the shear force-displacement diagram, it shows a sudden drop in the forces at a certain point after starting the quasi-static cyclic loads due to the deboning of the lintel after reaching its friction limit. After that, the shear demands remained constant till the end of the test. The second H wall showed a diagonal shear failure with increase in the shear demands indicating a higher strength and more energy dissipation.

2.2 Modeling and Analysis of Masonry Buildings under Seismic Loads

2.2.1 Modelling Approaches

Stone masonry buildings are known for their vulnerability when subjected to ground motions as they lack the required seismic design and suffer from random architecture, which leads to irregular load distribution and induced eccentricity. All these experimental lab tests are used to determine the elastic and plastic properties of the masonry elements that will be assigned to the structural model while simulating the behavior of a full-scale masonry building. It is important to build such models to study the seismic response of masonry structures. These results will contribute to enhancements in the design codes, rehabilitation decisions, and prediction of seismic responses during future events. Using data from experimental tests the numerical model can be calibrated for analysing real masonry building structures. Many modeling approaches were proposed through the years (Lourenco, 2002). It is important to stress that each method has an advantage over the others. Examples of potentials models are:

- Discontinuum models include detailed micro-modeling or simplified micro-modeling that is carried on through interface finite elements or discrete elements. This approach holds a large quantification burden due to the large amount of data assigned to the model, which means time consumption, and large probability of error; however, it can be used for small structures when all the data are available and good software is used.
- Continuum models include finite elements where detailed mesh is utilized to better simulate the behavior of structural elements and the failure mechanism. This method uses lumped masses, beam elements (equivalent frames), and macro-elements as 2D and 3D models, respectively. This method can be used for practitioners to obtain good response estimation if

the model is adequately calibrated though it has some uncertainties due to many assumptions taken.

Lourenco (2002) proposed to model parts of the structure rather than the full structure; to avoid the use of 3D modeling for the whole structure as it might impose several uncertainties, and to skip the linear elastic analysis that does not describe the plastic deformation of masonry buildings. The discontinuum modeling techniques are rarely used in practice as it requires detailed information. In the following chapters, the continuum modeling techniques will be used.

2.2.2 Collapse Mechanisms in Masonry Buildings

Observing the types of failure in the stone masonry structures subjected to lateral loads, (Andrea, 2015) and (Magenes, 2006) distinguished three failure modes that occur due to a structural composition of the building:

- The first mode is the partial failure of multi-leaf masonry walls due to the poor connection between the layers which is normally associated with the collapse of the external leaf.
- The second mode is the local failure, which is due to out-of-plane stresses in a particular member of the structure. This happens when a good bond between the layers of the multi-leaf wall exists; however, bad connections (wall-wall & wall-floor/roof) between the members exist.
- The third mode is the global failure that is activated due to the connections between the members that allows in-plane stresses to develop, which is transferred through the elements.

The global response of the masonry building can show a complex behavior which involves the interaction between the walls and the diaphragms and thus requires advanced knowledge on modeling procedures followed to simulate such output.

2.2.3 Types of Analysis

There are four types of analysis defined for the design and assessment of masonry buildings using the displacement-based procedures (Abrams, 2001):

- Linear Static analysis: application of equivalent static loads through calculating the demand base shear on the building corresponding to the fundamental period. It allows only the elastic behavior of the material. This is the simplest method used which does not account for the non-linear behavior of the structure thus overestimating the loads that will provide the same maximum displacement.
- Linear Dynamic analysis: application of dynamic loads using modal response spectrum and calculating the peak responses using the CQC methods. It allows only the elastic behavior of the material, which does not account for the non-linear behavior of the structure thus overestimating the loads that will provide the same maximum displacement.
- Non-linear Static analysis (Pushover): application of equivalent static loads described above while allowing the response to reach the plastic behavior of the material until failure. The fundamental period will change during the plastic behavior that can be accounted for using different types of load distribution. A control node must be selected. A final load displacement curve is obtained that allows to determine the displacements at yielding and failure corresponding to the base shear.

- Non-linear Dynamic (Time History) analysis: application of dynamic loads using time history ground motions which make the response highly sensitive to the changes in these records (that is why the use of multiple records is recommended). A precise simulation of the degradation parameters during the loading and unloading cycles must be assigned to the model to perform such analysis. If the input criteria are assigned correctly to the model, an accurate response is generated.

From the literature, several studies considered the pushover and time history analyses to investigate the response of masonry structures.

2.2.4 Modeling Examples and Comparisons

To build an accurate model, one should be able to simulate the response of the masonry structure expressed in terms of lateral displacement / interstorey drift, floor acceleration, and types of failure mechanisms as follows:

- Floor accelerations and displacements at positions determined within the building height such as the top floor level and other floors. These data allow to build the force-displacement curve that determines the limits and the stiffness degradation due to energy dissipation.
- Limits and failure loads experienced by the structures causing the yielding displacements, usually correlated with the first initiation of cracks and ultimate displacements.
- Failure mechanism that defines the crack initiation and propagation through the structural elements representing different mechanisms within the global response such as the bending/rocking, diagonal shear, and sliding shear according to their location in the elements.

Finite elements modeling is based on the idea of providing a continuum mesh of elements using a homogenization technique to transfer the diversity of masonry wall materials into similar particles with connections. Betti et al. (2014) used the ANSYS code to build a FE (finite element) model representing a two-story masonry building with wood diaphragm. The non-linear behavior simulates an elasto-plastic curve with brittle failure in tension resulted from non-linear static pushover analysis. The method was able to simulate the cracking initiating load, the failure mechanism, and the failure load, which provides important criteria about the stiffness degradation. However, the FE model could not reproduce the floor accelerations at the top of the building leaving a gap in the modal characteristics of the structure. This deficiency in the results is mainly due to the complications in the input data, which requires a high level of accuracy in the finite element modeling procedures. For the same building, a macro-element model was built assuming a rigid spandrel beam where the deformations are only allowed in the piers while rotations at the level of the floors are restrained. This type of macro-modeling technique overestimates the resistance due to the existence of flexible diaphragm which allow rotations in the real case scenario. The model was able to capture the failure loads and the accelerations at the top of the building; however, it could not simulate the failure mechanism. The study thus suggested to use both the FE model and the macro-model to attain a full response simulation data.

In the guidelines for the PERPETUATE project (Lagomarsino and Cattari, 2015) in Europe that focused on historical buildings, a pushover analysis was suggested using the macro-element modeling as a global approach for simulating the behavior of these structures. Major points are presented for the modeling procedures:

- Proper choices of the seismic load patterns such as: uniform (proportional to the mass), proportional to mode shapes, pseudo triangular (proportional to mass x height), adaptive load pattern (load updated at each step according to the non-linear response).
- Control node selection to determine the convergence of numerical results.
- Identification of representative displacement curve (pushover curve) that determines the capacity of the structure with respect to the base shear.

Special recommendations were given in case of flexible diaphragms and the use of time history analysis is recommended for confirming the results. A study conducted on a six-story unreinforced masonry building in Bosnia and Herzegovina (Ademović & Oliveira, 2012) aimed to simulate the response of this typical construction built in the 1960's, using finite element and macro-element modeling techniques. The building has concrete bearing walls in the underground basement level which opens the door to mixed construction simulation models that is still beyond the scope of this research. Providing the mechanical and geometrical properties, the two models were built using two different commercial software and studied by means of pushover and time history analysis. The building experienced a damage initiation at the ground floor due to stiffness difference between the concrete and the masonry elements that was simulated using both models. Comparing the capacity curves, the macro-models showed a little bit higher stiffness and ultimate force within a reasonable difference. Presenting the large computational burden required by the finite element model with respect to the slight difference in response and dynamic properties shows that the macro-modeling is a plausible approach to be used in the modeling of masonry buildings.

Cardoso et al. (2005) studied the Pambalino building structure located in Lisbon downtown. The building was made with internal wooden truss member representing interior walls and the floors,

and exterior walls were irregular calcareous masonry walls. Two types of nonlinear deformations are modelled to simulate the response of the structure. The cracking of the masonry leading to a ductile behavior, and the failure of the connections between the wooden truss and the exterior floor leading to brittle behavior. An iterative method was performed using 3D linear dynamic analysis in SAP2000. In each step, the stiffness was changed and reductions in the connections is applied with respect to the anticipated collapse mode. Using a long period ground motion, the building showed failure in the connections starting from the upper floor, which resulted in a local failure of the facade. This technique is adequate to locate the weak links responsible for local failure mechanism. However, inaccurate results might be obtained because the ground motion duration/ the number of ground motion cycles were not captured in the analysis and the energy dissipation by members cannot be calculated using the hysteretic loops because of the iterative procedure. This method cannot be used for regular masonry texture where the nonlinear behavior of the joints must be considered.

2.2.5 Example of damage assessment of URM churches

A study conducted on 700 churches in the L'Aquila after the earthquake in 2009 (Lagomarsino, 2012) showed good results in terms of detection of failure mechanisms and pointing out the vulnerability of masonry structures. This vulnerability assessment mainly allows for building a relationship between the input seismic forces and the occurring damage in a way to make a common phenomenon or failure mechanism between a common type of construction. This study yields a damage index that helps in the comparison between similar buildings and provides a direct hint about the collapse severity. Identifying the macro-elements based on the crack propagation in the façade, roof, apse, and the belfry of investigated churches is an important step for modeling these structures. In illustration of failure mechanisms, it was necessary to provide a damage grade

ranging between 0 (least damage) to 5 (complete damage) that reflects the condition of the macro-element. Separating each failure mechanism alone and adding the damage on macro-elements due to all possible failure modes yields the damage index ranging between 0 (least damage) to 1 (complete damage) which displays the average damage condition of each church. Using the survey records from many structures and adding the data to a specialized database allowed for the generation of the vulnerability index I_v ranging between 0 (least damage) to 1 (complete damage) that forms a correlation between the damage level of the building and the macro-seismic intensity of the ground record thus building the vulnerability curves and matrices. These data are used for emergency condition assessment of buildings and the decision making considering the future retrofitting procedures with the help of built structural models. Results from macro-seismic intensity effects shows the vulnerability of churches for high intensity ground motions as well as for low intensity ground records indicating the spread of damage even for areas far from the epicenter of the earthquake.

The ground motion of L'Aquila earthquake showed a short duration with 95% release of energy within less than 10 seconds. The fault shaking hit at a shallow depth of 10 km, which caused an intense shaking limited to certain zones of the region where local seismic amplifications are realized affected by the soil texture and the site conditions. Also, the vertical component of the earthquake appears in such cases which can cause crushing of the vertical piers in the churches and the loss of stability in the domes that are damaged in more than 80% of the cases.

Most of the churches under the survey goes back to the Middle Ages mainly formed of a single nave and a rectangular façade. After the 1703 earthquake in the same area, simple repairs took place for these structures including partial reconstruction of certain members, partial reconstruction using material familiar at that time, enlargements in the internal and external rooms,

or even performing an entire rebuilt project of the churches due to extreme damage. These modifications lead to increased vulnerability of the building due to the formed discontinuities between different members because of the enlargements, and reduced stiffness with the amplified height of the walls. Another type of construction for latter buildings was realized to include wooden ties inserted within the masonry units and anchored externally using metal plates to prevent the local failure of the connections and the central parts of long span walls weakened by openings and characterized by their medium sized irregular layout. Also, the roofs were fixed to the walls by means of wooden keys to activate the in-plane behavior. However, a major deterioration problem appears to invade the structures due to decay in wood elements and the effect of mass amplification resulting from reinforced concrete and steel constructions that increases the vertical demand and causes uneven distribution of stresses on the walls. In Summary, the most common failure mechanisms observed are as follows (Lagomarsino, 2012):

- Overturning mechanism of facade walls is usually characterized by local out-of-plane behavior that happens at any height of the wall. In case of many churches in L'Aquila, the failure occurs in the unconnected regions either due to lack of internal lateral or roof external wooden ties. Another common phenomenon is the collapse at the upper portion such as gables due to the less friction resistant because of less compression forces. Although a discontinuity between lateral walls is realized due to difference in the masonry types used at the corners which prevents the transfer of forces, the lateral wooden ties still activate in-plane stresses within the wall where fractures lines are realized. However, this resistance system is deteriorated enough with short overlaps in some cases causing it to lose its affectivity before the overturning of the whole wall in one shot. Some walls are strengthened used concrete covering that increases the

stiffness and prevent partial failure of the wall transferring the stresses into the base columns that could either take the lateral loads or overturn.

- Roof strengthening interventions using solid, thick, and rigid concrete slabs replacing the wooden trusses has negative effects on the behavior of structures. Heavy slabs have the tendency to slide over the walls, causing dynamic amplifications with the increase of the demand especially at the top of the building. Thus, the activated in-plane stresses are transferred to the lateral walls and the facade, which might not be able to carry these loads and leads to wider damage area. Usually, this damage is limited to local area in the case of weaker connections and prevents the uplift of the gable adding compressive stresses that might crush the masonry units. For these reasons it is recommended to substitute this strengthening technique with less rigid and lighter trusses.
- Collapse in apses that represent the oldest part of the church built with large, squared stones, is quite a common technique in such structures. An external leaf failure mechanism was activated in certain cases due to the followings: i) the weak connections with the internal leaves, ii) the presence of pilasters that divided the wall in different portions, reducing the bond and creating discontinuities, and iii) the addition of vertical stresses due to concrete interventions at the roof.
- Belfries that could be either plane or 3D bell cells formed of piers and arches are the most vulnerable elements in churches due to their positioning at the highest location of the building which provide high sensitivity for seismic shakings. Limited strengthening interventions in such structural elements can lead to hinge formations while preventing the overturning, however using stiffer strengthening can lead to rigid behavior and concentrate the damage in the piers which is not recommended.

An important asset of this survey (Lagomarsino, 2012) was to determine the macro-elements that are activated during ground motion events. These elements with the material tests performed in the lab or on site will contribute to calibrate or develop software that is able to model such structures to assess the behaviour and quantify the damage from a performance-based evaluation approach. The classification of structural elements is an important step to determine the appropriate modeling technique considered.

2.3 Probabilistic Model Using Bayesian Networks and Machine Learning

2.3.1 Probability in machine learning

The aim of machine learning is to automate the process of understanding and predicting data with minimal human interference. Basically, the process relies on a general function with different parameters and variables that need to be inferred in the best fit approach to explain our data. Probability in machine learning is deemed efficient due to the large uncertainty level in the information about an engineering problem (Ang and Tang, 1975). The less we know about our subject, the more useful the probabilistic approach in acquiring that information. In the field of unreinforced stone masonry structures, the degree of uncertainty substantially increases due to the higher number of unknown factors needed to construct the model. Therefore, it is very reasonable to seek this approach in solving this problem whether to validate predictive capacity formulations or to enhance the seismic performance of URM walls.

2.3.2 Bayesian Interpretation

Bayesian interpretation (Pearl, 1988) of the probability of an event depends on prior data which allows the modification of the outcome with the obtainment of new information. A useful tool that relies on this concept is BayesiaLab Software (Conrady and Jouffe, 2015) which utilizes the

probabilistic approach in Bayesian networks to create acyclic models (Nielsen and Jensen, 2009). To understand the Bayes Rule (Gelman et al., 2013), it is important to get familiar with the conditional probability, marginal probability, and joint probability.

$$\Pr\left(\frac{E_1}{E_2}\right) = \frac{\Pr(E_1 E_2)}{\Pr(E_2)}, \quad \Pr(E_2) \neq 0. \quad (2.1)$$

↑ Conditional Prob.
 ↙ Joint Prob.
 ↘ Marginal Prob.

This relationship can be derived from a simple Venn diagram illustrated in Figure 2.3 that shows the connection between two sets of events within a common sample space. The probability of occurrence of event E1 conditioned on E2 is thus inferred as the probability of intersection between these two events divided by the probability of E2. This is also referred to as the Product Rule.

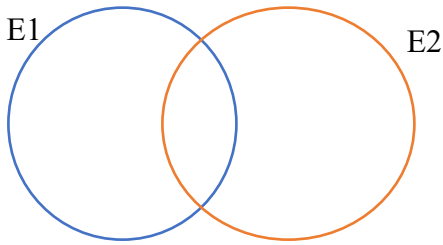


Figure 2.3: Venn diagrams for two set of events E1 and E2

Expanding the Product Rule will give us the Bayes Rule. The relationship between any two variables in the Bayesian network will thus follow this rule. The probability of E_i and the probability of A are the marginal probabilities based on the collected data whether directly from the field or through a calibrated deterministic model. Once the connection is established between the variables it develops the conditional probabilities that can be interpreted in both directions.

$$\Pr\left(\frac{E_i}{A}\right) = \frac{\Pr\left(\frac{A}{E_i}\right) \cdot \Pr(E_i)}{\Pr(A)} \quad (2.2)$$

Labels in the diagram:
 - Conditional Prob. points to $\Pr\left(\frac{A}{E_i}\right)$
 - Prior Prob. points to $\Pr(E_i)$
 - Posterior Prob. points to $\Pr\left(\frac{E_i}{A}\right)$
 - Evidence points to $\Pr(A)$



Figure 2.4: The connection between parent and child nodes creating the conditional probability.

In Figure 2.4, a connection is drawn between the two variable E_i and A . Referring to E_i as the parent node, it shall contain the marginal probabilities of E_i . A is the child node, which is dependent on the parent node E_i , thus it will contain the conditional probabilities of A/E_i . $P(E_i)$ & $P(A/E_i)$ are collected based on given data and human expertise. In most cases the desired information is the probability of E_i/A or $P(E_i/A)$ which is calculated using the Bayes Rule shown previously. The marginal probability of A or $P(A)$ can be calculated using the following mathematical procedure:

$$\Pr(A) = \sum_{i=1}^n \underbrace{\Pr\left(\frac{A}{E_i}\right) \cdot \Pr(E_i)}_{\Pr(AE_i)} \quad (2.3)$$

The Summation Rule stated above, which is also referred to as the marginalization constant, can be inferred from the Venn diagram in Figure 2.5 containing the two set E_i and A .

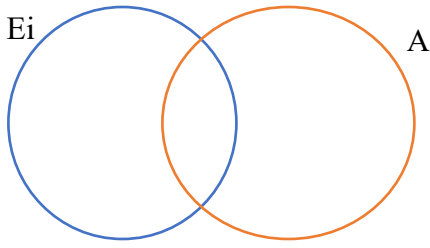


Figure 2.5: The intersection of the two sets E_i and A and the application of product rule

According to Fig. 2.5, the probability of A can be stated as:

$$P(A) = P(A \cap E_i) + P(A \cap \sim E_i) \quad (2.4)$$

given that set $\sim E_i = 1 - E_i$ or the complementary set to E_i . We can also express the joint probabilities as follows:

$$P(A \cap E_i) = P(A/E_i) \times P(E_i) \quad (2.5)$$

$$P(A \cap \sim E_i) = P(A/\sim E_i) \times P(\sim E_i) \quad (2.6)$$

Substituting the equations, we can get the probability of A as:

$$P(A) = P(A/E_i) \times P(E_i) + P(A/\sim E_i) \times P(\sim E_i) \quad (2.7)$$

Those values can be easily calculated relying on the Complementary Rule in probability given that the sets are collectively exhaustive.

2.3.3 Independency and the Chain Rule

Correlation does not mean causation. More factors should be considered to validate the causality between the variables under examination. For any interpretation of information within a set of data, to be valid, it must pass the non-bias check through the random selection of samples and the independency of the events through conditional ignorability. To elaborate on that, the Neyman Rubin model (Sekhon, 2009) explains this phenomenon in more details. The random selection of

different data can eliminate the bias which might appear if the sample is big enough to represent the actual variable. However, this will only create association between the data and not causality. A further step is required to form independency between the variables through conditioning on certain parameters are selected based on expertise opinion. Independent associated variables can thus be said to have causality that is formed by the fact of isolating the testing data set and making sure that the variable is changing without any external influence similar to a scientific lab experiment.

This can be represented in the following equation:

$$(Y_0, Y_1) \perp T/X \tag{2.8}$$

given that Y_0 and Y_1 are the outcomes, T is the input and X is the condition.

Having satisfied these conditions to ensure the upgrade from association to causation, the Chain Rule can now be applied which in terms expresses the joint probability of the set of variables within the sample space as the product of the conditional probabilities of each variable.

$$\begin{aligned} \Pr(E_1 E_2 \dots E_n) &= \Pr(E_1/E_2 \dots E_n) \Pr(E_2 \dots E_n) \\ &= \Pr(E_1/E_2 \dots E_n) \Pr(E_2/E_3 \dots E_n) \Pr(E_3 \dots E_n) \\ &= \Pr(E_1/E_2 \dots E_n) \Pr(E_2/E_3 \dots E_n) \dots \Pr(E_{n-1}/E_n) \Pr(E_n) \end{aligned} \tag{2.9}$$

In a more practical perspective, the Chain Rule can yield the probability of a set of incidences or the applicability of a set of parameters simultaneously. This accounts for a specific condition where we know all the observations in our model at a certain time or state.

2.3.4 Random Variables: Discrete, Continuous, and Density Functions

We can identify two types of random variables (Davenport and Root, 1987) within the set of observations. The first one is discrete random variables that announce themselves as categorical. They represent a finite set of variations that describe each state and can be represented by a probability mass function. Another type is the continuous random variables that are a series of numbers that are not bounded by determined states and can be represented by a probability density function. Relying on the mean and the standard deviation of the set of data, the following equation represents the probability density function (PDF) of a univariate normal random variable x and parameterized by the mean value μ and the standard deviation σ . This function will be used to discretize the data in later stages.

$$f_x(x) = N(x; \mu, \sigma^2) = \frac{1}{\sqrt{2\pi}\sigma} \exp\left(-\frac{1}{2}\left(\frac{x-\mu}{\sigma}\right)^2\right) \quad (2.10)$$

Another representation of the continuous data is through the cumulative density function (CDF) which sums the probabilities to a maximum value of 1. It is simply the integration of the PDF as given in the equation below.

$$F_x(x) = \int_{-\infty}^x \frac{1}{\sqrt{2\pi}\sigma} \exp\left(-\frac{1}{2}\left(\frac{x'-\mu}{\sigma}\right)^2\right) dx' \quad (2.11)$$

2.3.5 Discretization Functions

The analysis of the data is dependent on the discretization process which transform continuous variables into a finite number of intervals (Dash et al., 2011). Thus, it would be possible to limit the data to a certain number of conditions that is less computationally exhaustive and sufficiently representative for the information in the system. Each of the methods listed below has its

advantages and disadvantages and therefore its utility depending on the task required to be accomplished.

Equal Distance: it discretizes the data to equal intervals regardless of the amount of information present in each. It is a useful tool for variables with same domain variation where the classification can be attributed equally over the full range of data. However, this could be a problem in representing anomalies due to glitches in the records that needs to be filtered. A more satisfying tool in this case could be the Normalized Equal Distance method that removes outliers.

Equal Frequency: it discretizes the data to intervals with equal amount of information. This is a state of absence of knowledge about the conditions characterized by maximum entropy. For this reason, this method is only recommended after the structure of the data is already learned.

K-Means: it discretizes the data using only the targeted variable through generated random K means and clustering the data to the nearest mean. The actual mean is then selected based on the formed clusters. Then the process is repeated until the generated and the selected means overlap. This method is useful when we do not have a target variable such as the case of unsupervised learning.

Tree: it discretizes the data while taking into consideration the variable at hand and the target variable. Therefore, this method creates bias towards the target variable and is useful for supervised learning. The thresholds are selected based on the best utility that serves in that direction.

Those methods will be used in the model to assess the data generated by the deterministic model of the pier. The discretization process can highly influence the results of the probabilistic model and thus the testing of several trails is important to ensure the use of most practical data based on our expertise in the civil engineering structural domain.

2.3.6 Mutual Information and Entropy Reduction

Calculating mutual information (Paninski, 2003) rather than mere correlation overcomes the linear limitation of the commonality between the variables. Thus, the relationship does not have to be a factor measuring the slope of variation between the information, it can now create a relationship for any type of correlation between data depending on the entropy level and the degree to which it reduces the uncertainty in the next variable. Then the influence of the variables on a certain target node can be specified with less limitations and better representations of the actual data.

Correlation coefficients describes the linear relationship between two or more variables. If those coefficients are zero however, it does not mean that the variables are independent as there are nonlinear forms of relationships that can be established. The mutual information coefficients based on the calculations of entropy is independent of the type of the relationship and is thus able to represent linearity and nonlinearity without any limitations in that regard. The limitations are found within the capacity of each probability cell which requires a minimum number of observations per variable to produce valid information. There are some tools available in the BayesiaLab software to overcome such limitations. The entropy is calculated as:

$$H(X) = - \sum_{x \in X} P(x) \log_2 P(x) \quad (2.12)$$

Here, x is the interval within the selected variable and $P(x)$ is the probability of the interval. The second base logarithm is used as the unit of information the software is bit. The Entropy is thus a random number that lays on a scale between zero entropy where one interval has all the data and maximum entropy where the data is distributed equally between all the discretized intervals. In the same manner the conditional entropy for the target variable is calculated as:

$$H(X/Y) = - \sum_{x_i \in X \& y_i \in Y} P(x_i) \cdot H(x_i/y_i) \quad (2.13)$$

Using the entropy level determined at the level for variable, it can be used to predict its influence on the target variable through calculating the mutual information as:

$$I(X, Y) = H(X) - H(X/Y) \quad (2.14)$$

Now simply by dividing the mutual information to the marginal entropy for the predictive and the targeted variables, it is possible to calculate the gain in information about the variables and therefore estimate the predictive importance of the variables regarding the targeted goal of the study.

2.3.7 Supervised Machine Learning Algorithms

Supervised machine (Maglogiannis, 2007) learning is focused on a particular direction where the purpose of the algorithms is to generate a causal relationship between a number of predictive variables and the target variable. Once the model is built, it would be possible to predict the target based on the new observations we receive. There are several algorithms that are specific to supervised machine learning which differ in the way they handle the variables and their subsequent relationships within the network. In here, we will define three functions that are used to study the data from the piers.

Naïve Bayes Network (Chen et al., 2020): the basic function in the Bayesian network that is formed of one parent node which is the target node and a set of child nodes which are the predictive nodes. This algorithm simply connects the target variable to all the other variables found in the graph. It is considered as a first step in understanding the data and acquiring a global view of the model.

Markov Blanket (Fu and Desmarais, 2010): a function that concentrates on the nodes that predict the behavior of the target variable shown in Figure 2.6. In other words, it contains the nodes that can isolate the target node or make it independent by having knowledge of their states. Those

nodes are usually the direct parent nodes, the child nodes, and the other parents of the child nodes. In this way, Markov Blanket highlights the most predictive nodes thus maintaining the simplicity of the acyclic model without having to include the full data set. This could save time and remove computational burden off the system.

Augmented Markov Blanket: it is considered as an extension to the Markov Blanket algorithm that applies an additional learning to the connected nodes in the Markov Blanket. This will create additional connections between the predictive nodes that are used to identify the target variable which will enhance the performance in the model.

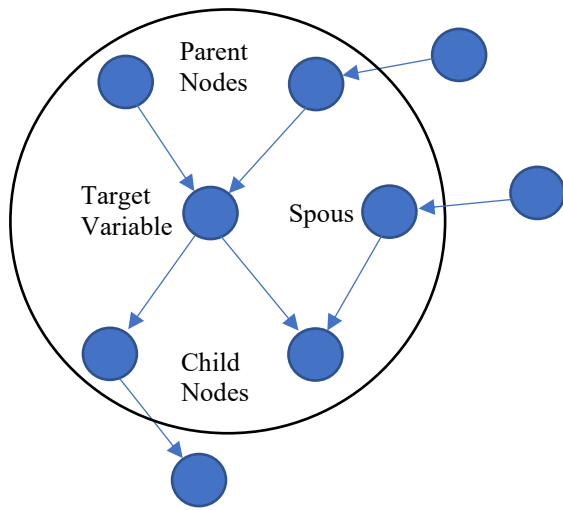


Figure 2.6: The nodes included within the Markov Blanket for the target variable shown within the circumference of the circle.

2.4 URM structures in Montreal and Failure Mechanisms

Stone masonry buildings form the aesthetic of cities and mark the city heritage. Many of these building structures are located in active seismic zones and are prone to damage due to their high vulnerability to lateral loads and the lack of design criteria at the time of construction (Elmenschawi & Shrive, 2015). To rise the safety requirements, building codes are updated regularly and the seismic hazard level in many regions of Canada has been increased. For example, only in the last

decades, the seismic risk was increased from 10% in 50 years probability of exceedance (NBCC 1995) to 2% in 50 years probability of exceedance (NBCC 2005). Hence, a significant number of existing stone masonry structures are deficient and at risk under potential seismic loading.

2.4.1 Seismic Data in Montreal

The Western Quebec region had experienced several major earthquakes distributed as shown in Figure 2.7 (NRC, 2015). Most of the larger magnitude shakings ranges between a magnitude of 5 and 6 on Richter Scale. An earthquake of magnitude 5.9 occurred in Saguenay in 1988 that was also felt in Montreal and produced minor damages. The average occurrence of small earthquakes (< M4) for this region is estimated to be once every 5 days.

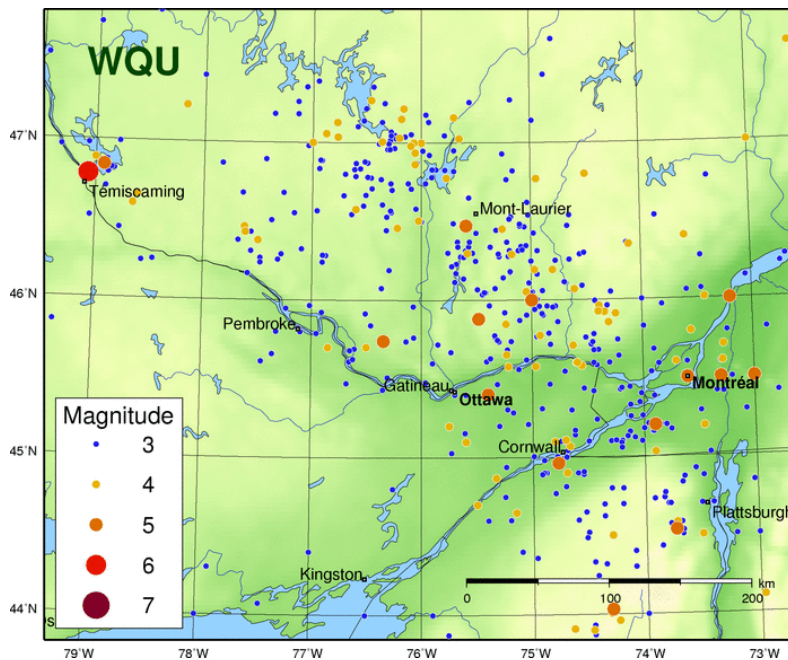


Figure 2.7: The Western Quebec Seismic Zone showing the historical seismic activity in the region (NBCC 2015).

Brought by the industrial revolution in the mid-1800s, more than 54% of the construction in Montreal took place between the years 1860 and 1913 with 45% of the available stock having 3 to 5 stories classified as low-rise structures (Nollet et al., 2004). Most of these buildings consisted of

exterior bearing walls and flexible wooden diaphragms. Among Canadian cities, Montreal has a great number of stone masonry buildings which are typically low-rise structures built in the 19th and the 20th century. According to a study conducted in the Old Montreal area, it was shown that more than 44% of buildings are unreinforced masonry structures and represent the dominant category among steel and concrete materials (Nollet et al., 2004). Even though Montreal is in a moderate seismic zone located on the North American plate, it has witnessed several earthquakes in the past and will potentially experience them again in the future.

According to a study conducted on eight URM walls of 2 meters high and 0.54 meters thick (Elmenschawi et al., 2010), the natural period ranges between 0.08 seconds to 0.12 seconds. In general, low-rise URM buildings in Quebec can have an average fundamental period of 0.18 seconds (Abo-El-Ezz et al., 2013).

The soil classification in Montreal is shown in Figure 2.8. Dominated by Site classes B and C, which indicate rock and dense soil sublayers of the earth, some locations in the north of Montreal are Site class D (stiff soil). Buildings built on Site classes B and C are less vulnerable to ground shaking.

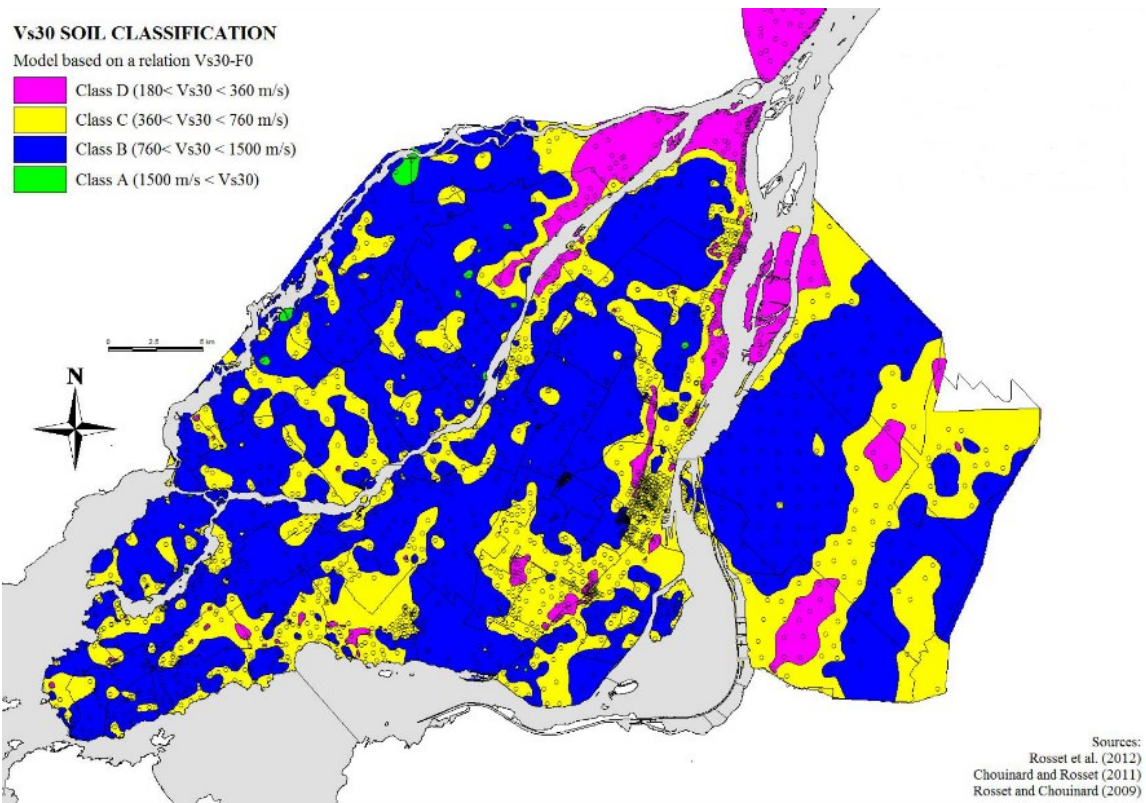


Figure 2.8: Soil classifications for Montreal area (Rosset & Chouinard, 2009)

The low-rise URM building structures are amongst the most vulnerable to the seismic hazards. It is evident that the threat from such ground shakings is noticeable on certain spots along the river creeks close to Quebec City and Montreal (Figure 2.9). Cities in Canada and particularly in Quebec are known for their existing stone masonry buildings and heritage structures.

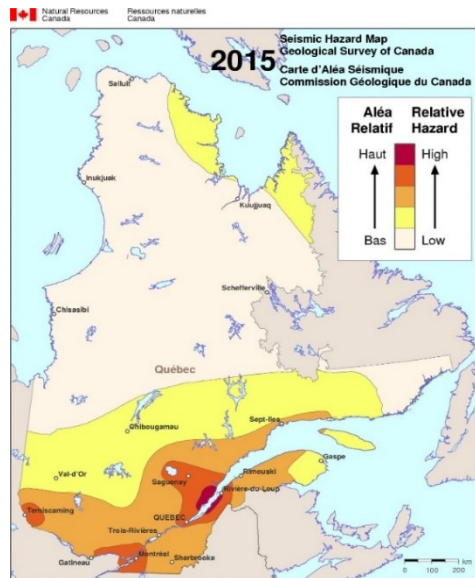


Figure 2.9: Relative seismic hazard in Quebec for 1-2 story structures (NBCC 2015).

2.4.2 Assessment of Existing Structures Using Macro Modeling Approaches

2.4.2.1 Modeling Discretization

Unreinforced masonry (URM) building structures are complex structures due to several reasons. The multiple construction phases and the diversity of walls cross sections makes it a large challenge to identify the exact mechanical and dynamic properties of those panels (Binda et al., 2005). Even though destructive and non-destructive tests have been conducted, it is still difficult to gather comprehensive data for all the structural components. Thus, using detailed models such as micro modeling and finite element techniques will still embed errors in the model that might lead to misinterpretation of the results. For this reason such sophisticated models are only recommended for small number of masonry constructions (Lourenco, 2002). On the other hand, macro models reveal a very useful approach to eliminate the complex details, where most of the errors occur, and provide a simplified method to deal with such tasks given that a proper calibration has been achieved. Several studies show that macro modeling techniques that use the equivalent frame methods are deemed successful to capture the behavior of masonry elements. The equivalent

frame method was first proposed by (Tomazevic, 1978). Then, this method was developed into the Simplified Analysis Method (SAM) that was proposed by (Magenes and Calvi, 1997b) and refined later by (Magenes and Della Fontana, 1998). Figure 2.11 shows a 2D equivalent frame model where piers and spandrels follow a predefined constitutive law that is exemplified through bilinear up to multi-linear curves depending on the level of precision. Further, Magenes (1999) proposed a 3D model to analyse the stone masonry structures.

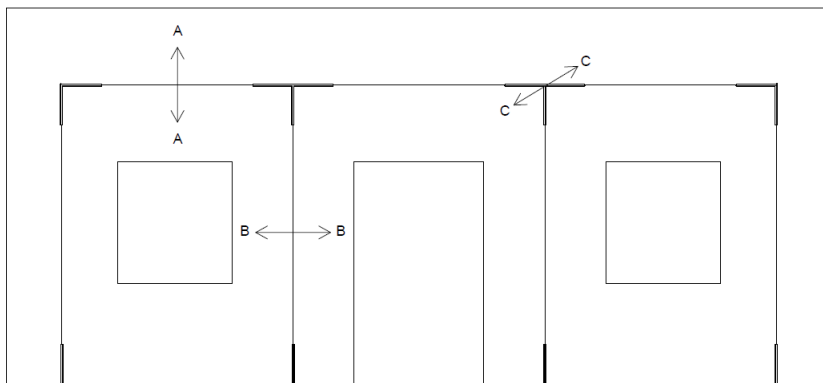


Figure 2.10: Equivalent frame discretization

The SAM is applicable to masonry walls with regular openings which allows to extract distinctive structural elements required to develop the equivalent frame model. The discretization of a masonry wall in the effective zones follows the original dimensions of structural elements centered within the masonry panels. The length of the element is determined following the method proposed by Dolce (1991). The plastic zones are allowed to occur in piers and spandrel beams under the gravity load in combination with lateral forces. Illustrated in Figure 2.10, Piers (section BB) are the vertical elements considered as the main force resistance components in a masonry wall. Spandrels (section AA) are the horizontal beams connecting to adjacent piers responsible for the

coupling effect. The connections between piers and spandrels are considered as rigid (section CC) as no failure is expected (Bucchi et al., 2013).

2.4.2.2 Equivalent Frame Modeling Approaches

Different modeling approaches has been considered to build an equivalent frame that is able to simulate the behavior of masonry piers. They can all be summed into two categories: the lumped plasticity models and the distributed plasticity models. Lumped plasticity models tend to define the nonlinear properties of the material within a defined hinge that is positioned at a certain fraction of the element length. The location is determined based on the mode of behavior associated with the element and the stiffness of the section. This could also be affected by the calibration procedure following a particular experimental test. For example, a single failure mode interaction surface is used to represent the combined failure mechanism defined in hinges located at the center and both ends of the elements with an application in SAP2000 (Petrovčić and Kilar, 2013). Another model considers a shear behavior in a hinge defined in the middle of the element and the flexural behavior defined at the ends of the element connected with rigid links and utilizing tailored hysteretic laws with an application in ABAQUS (Rinaldin et al., 2016).

The distributed plasticity models disperse the nonlinear properties throughout the element where the flexural and shear responses are overlapped within the same section. (Raka et al., 2015) applied the force-based element to capture the behavior of URM walls using a fiber section to couple the moment-axial interaction with the shear behavior. The force-based element has an advantage of preserving the equilibrium between the forces generated from both modes, and limiting the model into one element what reduces the number of degrees of freedom (Marini and Spacone, 2006). With decent application in OpenSees, the fiber elements account for the moment-axial force

interactions while a shear phenomenological law is implemented and coupled with the force-based element (Martino et al., 2000).

2.4.2.3 Modes of Failure

Failure modes in typical masonry walls fall into two major categories. The shear behavior illustrated in diagonal tension failure and the sliding shear failure. The second one is the flexural behavior illustrated in rocking failure and the toe crushing phenomenon (Pasticier et al., 2008). Demonstrated in Figure 2.12 are the cracking patterns associated with each mode of failure.

Figure 2.12.a shows the diagonal cracks along the head and bed joints at the interface of mortar and unit masonry. Another type is the diagonal cracks through the unit stones that does not happen often due to the very weak properties of the used mortar. Diagonal cracks usually take place in squat specimens with high level of pre-stress. Figure 2.12.b represents the horizontal cracks along the bed joints that is more likely to happen with squat specimens with low level of pre-stress. Tianyi et al., (2006) conducted experimental tests on a full-scale two-story building subjected to cyclic loads applied on walls with large and small openings. It is noted that shear mechanism experienced by squat piers is characterized by brittle behavior with high maximum strength, low displacements, and high energy dissipation.

Rocking failure shown in Figure 2.12.c demonstrates how gaps are formed at the opposite corners against the application of the lateral load. This mode of failure occurs with slender specimens at low level of pre-stress before the loss of tension resistance due to bending. Toe crushing failure in Figure 2.12.d occurs due to high levels of pre-stress on the slender specimen causing it to crush at the bottom toe opposite the lateral load. Also, horizontal cracks due to tension and spalling of masonry units due to compression can happen. Full scale tests on piers with different aspect ratios are subjected to in-plane cyclic loads (Magenes et al., 2010). Flexural behavior experienced by

slender piers exhibits large displacements, low maximum strength, and most importantly low energy dissipation throughout the hysteretic loop.

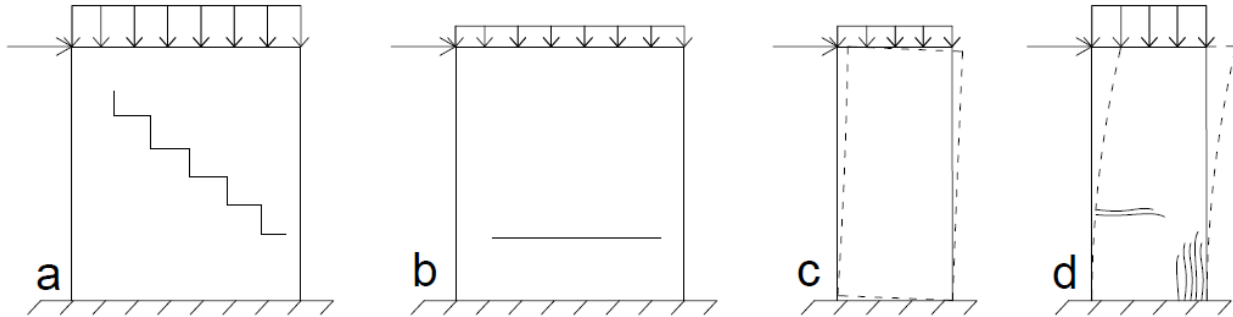


Figure 2.11: Failure mechanisms that occur in masonry piers due to lateral and vertical loads. a- Diagonal shear, b-Sliding shear, c-Flexural rocking, d-Toe crushing.

Masonry panels are characterized with several parameters that contribute to their seismic behavior. Small or large openings in walls results in different aspect ratios for piers defined as squat or slender specimens as mentioned earlier. The texture of the masonry units can also play an important role in the lateral response whether it is shown with smooth surface, irregular with partially worked surface, or rubble stones placed irregularly within thick layers of mortar. The third parameter is the cross-section of the walls that can range between single-leaf and multi-leaf construction with different properties of internal and external layers (Binda et al., 2005). Several types of stone masonry are available in the existing historical buildings such as the sedimentary rocks being the most popular including sandstones, limestones, clay-stones, etc. Another type is igneous rocks including granite-stones (Como, 2013). Mortar influences the strength of masonry panels substantially. Tests on rubble masonry panels (Milosevic et al., 2012) showed that the shear strength was magnified up to ten times in samples with hydraulic lime compared to those with air lime mortar. Dry joints are also used in some construction practices. The influence of scaled specimens with different boundary conditions including cantilever or fixed-fixed restrains is also

considered (Tomažević, 2000). Those parameters are controlled by the relative stiffness between piers and spandrels. It is more likely to find structures with boundary conditions in between those extremities, however it is simpler to adjust the tests for either one. The variations in the number of stories in masonry buildings imposes different gravity loads on the wall under examination. Thus, a set of pre-stress levels are established for experimental tests.

2.4.2.4 Example for Equivalent Frame Modal Calibration Using Experimental Tests on Full Scale Structures

Rota et al., (2011) conducted a study based on fragility curves to determine the vulnerability of low-rise masonry buildings to earthquakes by comparing the annual probability of damage for different prototypes. This work was also reported by Penna (2015). The values of average annual damage factor in the descending order where the masonry stone layout, floor condition, and the presence/absence of connections between planes is displayed. Masonry buildings with regular layout, rigid floors, and with the presence of connections showed the least damage factor indicating better resistance to earthquake shakings. Considering these issues in the construction of such masonry buildings, the EUCENTER and University of Pavia performed several tests on three full-scale two-story buildings strengthened in three different levels, using an irregular layout double leaf walls with flexible diaphragms. The behaviour of these prototypes is described below.

- The first prototype, made without any proper strengthening, showed an out-of-plane failure that can be fixed using simple procedures for enhancing the connections between the structural members. This can be modeled using simple analysis methods where parts of the structure can behave separately after being identified through observed cracks or a certain 3D laser scanning technique. The material properties are set to be elastic while the plastic behavior is limited to the contact interfaces between masonry elements and timber using friction laws during plastic

deformation. The out-of-plane behavior seems to be highly controlled by the opening distributions and locations.

- The second prototype was partially strengthened to prevent the local failure mechanism activated in the first test. The strengthening included the addition of a steel ring beam at the floor level improving slab-walls connections, addition of reinforced masonry beam at the roof level improving the roof-walls connections and adding another layer of timber to the roof. This strengthening intervention increases the in-plane behavior of the building but still allows for flexibility in the horizontal diaphragm.
- The third prototype was strongly strengthened by casting a concrete slab at the floor level and adding anchors through the walls attached to the slab, adding a concrete beam at the roof level, and adding multiple layers of plywood to the roof diaphragm. This method allowed for rigid behavior of the building. The ground motion selected for the three sample structures was the same record of 1979 Montenegro earthquake applied gradually until reaching the ultimate response allowing for comparison through different steps.

The modeling of the 2nd and the 3rd buildings was performed using the Tremuri software launched in 2001 by the University of Genoa (Lagomarsino et al., 2013). Tremuri is a specialized program for modeling of masonry structures with flexible diaphragms. Using the concept of equivalent frame model implemented in different seismic codes such as Eurocode 8, ASCE/SEI and NTC 2008 (Italian Building Code), a clear definition of spandrels and piers is presented and used to define the 2D wall elements that were assembled with special nodal connections to form the 3D model of the building. Also, a versatile modeling of the diaphragm allows the simulation of stress and strain distribution that affect the stiffness and the deformations in the floors and the connected walls as well.

The equivalent frame modelling approach utilized in the software divides the structural members into spandrel beams, piers, and rigid nodes that form the connections between the latter elements (Penna et al., 2014). The geometrical discretization used is calibrated based on damage patterns from experimental tests where the piers appeared to have the same height of the adjacent opening. For the 2nd building, uniform distribution seems to fairly match the initial stiffness, while keeping the maximum base shear underestimated. For the 3rd building, uniform distribution overestimates both the initial stiffness and maximum base shear in the negative branch. Modal and adaptive patterns better estimate the behavior in the 3rd building with almost similar response due to existence of only 2 stories that decrease the effect of higher modes.

2.4.2.5 Application of Equivalent Frame Modal Evaluation for Masonry Building using SAP2000

The equivalent frame method is a simplified modeling technique that tends to define a micro-structure such as masonry buildings formed of separated units (masonry and mortar) as macro-elements connected to form a frame that acts simultaneously with other defined frames to reflect the global behavior of the structure. Although the process appears to simplify the complexity of the materials, it has been proven valid due to the matching results with experimental simulation campaigns performed using this technique. The SAM method appears to have a proper implementation in the commercial SAP2000 software (Pasticier et al., 2008) which provides facilities for engineers to use it in designs.

Two main structural elements can be defined within the masonry walls that can form the equivalent frame in the model (Bucchi et al., 2013). The vertical piers that represent the principal resistance for dead load and seismic load located between the openings, and the horizontal spandrels that represents the coupling effect between piers playing a major role in the seismic resistance. Different configurations are then executed which depends on the spandrel's strength in tension.

Weak spandrels give cantilever piers, strut spandrels with one tension resisting member gives partially coupled piers, and beam spandrels give shear type piers. Considering the global in-plane behavior of the structural members in the masonry building, the third configuration is considered in the modeling. In SAM modeling method, the piers and spandrels are deformable allowing for displacement and rotation which considers the flexibility of the diaphragms giving it an advantage over other proposed methods, with rigid connections as no displacements are expected to take place in that location. The technique is accepted in various international codes such as EUROCODE 8 and the Italian Codes NTC08.

In a study released by Magenes and Della Fontana (1998), a simplified analysis method for modeling masonry walls using spandrels and piers is provided. The modeling technique showed good simulation of results obtained from a non-linear finite element analysis proven experimentally. Deformable piers and spandrels were assumed with rigid connections. The results were able to fairly match the internal forces distribution, the failure mechanism, and the displacements especially when a brittle behavior of the spandrels was considered. Using ANSR software (Mondkar and Powell, 1977), a limit to rotation was also provided where the load carrying capacity is lost beyond it. SAM was proven a good modeling method for brick walls with weak mortar joints, which can be used for 3D buildings in the case where no out-of-plane failure is expected to happen. However, cyclic tests are required for spandrel beams to extract their properties.

The force displacement behavior of the elements is defined through assigned hinges that simulates the plastic deformations while the elastic part is covered by defining the elastic properties to the elements directly (Pasticier et al., 2008). Pushover and the time-history analysis are performed with two different positioning of hinges along the elements. Shear hinges in the piers are located

at the mid-span while the rocking hinges are located at both ends of the piers. In the pushover analysis the force displacement curves for the piers are selected to be elastic perfectly plastic with brittle failure. For spandrels, the curves are selected to be elastic with brittle failure reaching a residual strength equal to quarter the original strength without any limit for displacement. In the time-history analysis, the force-deformation backbone is used to represent the behavior of the non-linear link. The parameters for stiffness degradation are defined based on a separate simulation analysis performed experimentally on a brick wall using SAP2000.

Inter-story drift limits (ISD) were determined based on the EUROCODE on the pushover curve:

- Yielding point (Limited Damage): $ISD/h = 0.007\%$
- $\frac{3}{4}$ of Ultimate displacement (Significant Damage): $ISD/h = 0.2\%$
- 20% reduction in ultimate strength (Near Collapse): $ISD/h = 0.3\%$

The limit states have low values due to the brittle properties assigned to the hinges. Considering the time history analysis, 14 response spectra are chosen as ground motion input (Pasticier et al., 2008). There is a big difference in the response between different earthquakes due to different response spectra utilized in the analysis. The incremental dynamic analysis (IDA) curves have higher shear strength than the pushover curves due to the use of real recorded shaking. The failure mechanism captures a weak story in the ground level.

In summary, several types of existing unreinforced masonry structures (URM) are presented showing the different characteristics associated with such buildings. In Montreal, a direct association is made with the popularity of low-rise existing structures and the ground records that can have major detriment on its lifetime. A brief description of machine learning approaches using the Bayesian Networks is presented showing the importance of such tools in data analysis. With

the aid of some examples, major failure modes and collapse mechanisms in URM structures are identified. Those will be utilized in the next chapters to help understand the behavior of some elements and to justify the methods followed to analyze the performance.

Chapter 3: Preliminary Parametric Study on the Shear and Flexural Capacity Simplified Formulations for URM Walls

The complexity of analysing the existing unreinforced masonry (URM) structures and the uncertainty factor associated with modeling practice makes it difficult to accurately simulate the behavior of this structure subjected to earthquake ground motions. A parametric study on the shear and flexural behavior of unreinforced masonry elements is performed in the aim of developing a correlation between the different characteristics of masonry piers responses and their seismic capacity equations. Then, the study focuses on defining the accuracy of the proposed formulations used to compute the strength of masonry panels regarding their dominant mode of failure. Four shear formulations and five flexural formulations for masonry piers, and seven shear formulations for spandrels are utilized to generate the in-plane cyclic experimental data and compare the results in terms of divergence ratios. It was found that each proposed equation can specialize in determining the lateral shear capacity of URM piers based on a variation of a set of major parameters that can highly influence its performance. Data collected from the literature was used to model the behaviour and validate the outcomes resulted from analysis to ensure the reliability of the formulations and the capability of modelling any type of URM piers and spandrels.

3.1 Shear and Flexure Dominant Behavior in Masonry Pier Elements

Simplified capacity formulations for flexural and shear behaviors are used to capture the strength of masonry piers. The formulations are tested against the different parameters to evaluate their competency for providing accurate results when compared to experimental data. In this work, sliding shear behavior is neglected, as the diagonal tension dominates the mode of failure associated with shear. In the first part, four diagonal shear formulations are introduced. In the second part five flexural formulations are used. Note that rocking and toe crushing are

complementary in many scenarios and both formulations are generally used for all cases. Each formulation is calibrated based on different experimental setups and leans on a certain factor derived from the mechanical properties of assemblages used to estimate the compression, tension, and shear strengths. The samples are masonry units assembled in a specific way to serve the purpose of the test. The outcomes of those tests function as the characterizations assigned to each masonry panel. It is noted that the special signs in the formulas are modified from their sources as to unify the equations.

3.1.1 Diagonal Shear Mode

The Canadian standard for masonry buildings CSA-S304 (CSA, 2014) suggests a formulation for diagonal shear capacity originally for brick and concrete masonry materials. However, the effectiveness of this formula, Eq. (3.1), to predict the shear strength in stone masonry will be examined.

$$V_{u,1} = (f_v b_w d_v + 0.25 P_d) \gamma_g \quad (3.1)$$

Herein, b_w is the wall thickness, d_v is the effective depth of the piers but should not be less than $0.8L_w$, where L_w is the length of the wall. In addition, $\gamma_g = A_e/A_g$ is a factor to account for partially grouted walls or non-solid units which was considered as 1.0 here because we have solid masonry units with full mortar joints where A_e and A_g are the effective and gross cross-sectional area of the pier respectively, P_d is the axial compression load on piers equal to $0.9 \times (\text{dead load} + \text{axial load due to bending in the coupling beams if is the case})$. It is important to note here that the effect of bending in the beams was neglected in this paper as the additional axial load is minor in low-rise structures; however, it must be considered in a more detailed analysis; f_v is the shear strength of wall assemblages.

Turnšek and Cacovic (Turnšek & Čačovič, 1971) suggested another formulation for diagonal shear that accounts for the maximum tensile strength at the middle of the pier. It is calibrated based on experimental tests performed in Ljubljana, Slovenia, on doubly fixed specimens with single leaf walls:

$$V_{u,2} = \frac{f_t L_w b_w}{\xi} \sqrt{1 + \frac{\sigma_o}{f_t}} \quad (3.2)$$

Here, f_t is the principal tensile strength, σ_o is the vertical stress, ξ is a parameter that depends on the aspect ratio h/L_w where h is height and L_w is the pier length. The variation of ξ is as follows: $\xi = 1.0$ for $h/L_w \leq 1.0$, $\xi = 1.5$ for $h/L_w \geq 1.5$, and $\xi = h/L_w$ for $1 < h/L_w < 1.5$.

Other expression for diagonal shear account on Coulomb criterion where a correction factor (Magenes & Calvi, 1997a) which refers to failure in piers with irregular texture that occurs at the interface between the mortar and the masonry units is added:

$$V_{u,3} = \frac{c + \mu_s \sigma_o}{1 + \alpha_v} (L_w b_w) \quad (3.3)$$

Here, c is the cohesion strength; μ_s is the friction coefficient; $(1 + \alpha_v)$ is a correction factor that accounts for the boundary conditions at the global behavior of the pier where $\alpha_v = H_o/L_w$ and H_o is the effective height of the pier to the location of zero moment and σ_o is the vertical stress

Lourenco (Lourenço et al., 2005) suggests another formulation for diagonal shear, calibrated based on dry-joints regular texture in single-leaf stone masonry walls. The specimens used in the tests had a 1000x1000x200mm dimension and were loaded monotonically, while applying different vertical load scenarios ranging from 0.15 to 1.25 MPa. The stone units are known as Montjuic (locally available in Barcelona) and have the following characteristics: $f_m = 82.7 \text{ MPa}$, $E = 15500$

MPa, $\rho = 25 \text{ KN/m}^3$, $f_t = 3.7 \text{ MPa}$, where f_m is the compressive strength of the assemblage and f_t is the principle tensile strength.

$$V_{u,4} = P \tan \phi \left[1 - \frac{h}{2L_w} \tan \phi \left(\frac{1}{1-\nu} \right) \right] \quad (3.4)$$

Here, P is the vertical force applied on the pier including its own weight; $\tan \phi = \mu_s$; $\nu = \sigma_o/f_m$; ϕ is the angle of the stress lines formed within the pier.

3.1.2 Rocking and Toe Crushing Flexural Modes

Using equilibrium at the plastic state of the column behavior, the following equation can be derived to account for the rocking flexural mode. The equation is given bellow (Magenes & Calvi, 1997b):

$$V_{u,5} = \sigma_o \frac{L_w^2 b_w}{2H_o} \left[1 - \frac{\sigma_o}{0.85 f_m} \right] \quad (3.5)$$

where L_w , b_w and H_o are the pier dimensions defined above and σ_o and f_m are the pier's mechanical characteristics.

For Rocking and Toe-Crushing the following two equations given bellow are provided in FEMA 356, (2000).

$$V_{u,6} = 0.9 \alpha \frac{L_w}{h} P \quad (3.6)$$

$$V_{u,7} = \alpha P \frac{L_w}{h} \left[1 - \frac{\sigma_o}{0.7 f_m} \right] \quad (3.7)$$

Here, $\alpha = 0.5$ for cantilever and $\alpha = 1$ for fixed-fixed boundary conditions. P is the axial vertical force applied on the pier and the other parameters: L_w , h , σ_o and f_m were defined above.

Using regression analysis, Lee et al., (2008) modified Eq. (3.7) and derived the following equation to capture the toe crushing failure mode:

$$V_{u,8} = 560\alpha P \frac{L_w}{h} \left[1 + \frac{\sigma_o}{0.5f_m} \right] \quad (3.8)$$

Then, Benedetti & Steli, (2008) suggest Eq. (3.9) for capturing the toe crushing failure mode, based on the equilibrium of the stresses at the plastic state of the pier. The formulation relies on the compressive strength and the ductility index of masonry samples under axial compression to compute the width of the compressed zone at the ultimate limit state.

$$V_{u,9} = \frac{P}{H_0} \left[\frac{L_w}{2} - j\beta_u \right] \quad (3.9)$$

where $j = \frac{3D^2 - 3D + 1}{6D^2 - 3D}$, $\beta_u = \mu \frac{P}{b_w f_m}$ and $\mu = \frac{1}{1 - 0.5D^{-1}}$

Here, j is the non-dimensional distance of the stress block centroid to the compressed side expressed in terms of D , where D is the ductility index for compressive strength, B_u is the width of the compressed zone dependent on the factor μ which is limited to the interval [1 to 2].

It is noted that the capacity formulations for flexural behavior are expressed in terms of compressive strength of masonry samples, unlike the ones for shear behavior that rely on various factors such as the shear strength, tensile strength, compressive strength, and the friction parameter.

3.2 Validation of the Formulations

Experimental data from several tests are utilized to serve as a validation for the formulations suggested by the codes and literature. The process for choosing the experiments depends on the availability of the data and its ability to serve the purpose of the study. It is required to test the effectiveness of the formulations in representing the behavior of masonry panels in terms of maximum strength along with the variations of the parameters. Thus, a correlation between the

efficiency of each formulation provided above which optimizes the results and increases the accuracy of the overall simulation of masonry structures is presented. In-plane cyclic tests are utilized as experimental data to extract the maximum shear force capacity of the piers, which is generally characterized by shear or flexural cracking patterns. Both failure modes are analyzed in the next two sections.

3.2.1 Experimental Data for Testing the Shear Capacity

Three following three tests are used to validate the efficiency of formulations for diagonal shear.

- The 1st testing data set was collected from experimental tests conducted at the University of Pavia and EUCENTRE (Magenes, Penna, Galasco, & Da Paré, 2010). From these tests, samples named as **A** and **B** were collected.
- The 2nd experimental data set was selected from tests conducted at the University of Minho Vasconcelos & Lourenço, (2006), where the lateral response of three different typologies of walls, labelled **WS**, **WI** and **WR**, were investigated, where **WS** represents dry walls i.e., sawn stones without any mortar, **WI** represents irregular stones with applied weak mortar, and **WR** sample represents rubble stones with applied weak mortar.
- The 3rd experimental data set consists of experimental tests on dry-joints masonry panels, conducted at the Structural Technology Laboratory of the Technical University of Catalonia, Barcelona Lourenço et al., (2005), using samples labeled as **SW**, was selected.

A summary of the preliminary mechanical properties of the aforementioned samples are listed in Table 3.1. As mentioned before the values must refer to masonry assemblages or masonry wallets. For this reason, modified values for the compressive strength are calculated to obtain the correction values from prism tests.

Table 3.1: Preliminary mechanical parameters for masonry assemblages

Specimen	f_m [MPa]	Modified f_m [MPa]	f_v [MPa]	f_t [MPa]	μ	c [MPa]
A, B	3.28	3.28	0.197	0.137	0.65	0.35
WS	73.00	65.7	N/A	N/A	0.65	0.00
WI	7.00	7.00	0.17	0.12	0.63	0.36
WR	5.00	5.00	0.16	0.11	N/A	N/A
SW	52.00	36.62	N/A	N/A	0.62	0.00

Regarding the 1st experimental data set, for samples **A** and **B**, the values of the cohesion strength, c , and the friction coefficient, μ_s were chosen based on Elmenshawi & Shrive, (2015). In-plane cyclic shear tests were performed on squat pier **A1** and **A2** with aspect ratio $h/L_w = 1$ and slender piers **B1** and **B2** with aspect ratio $h/L_w = 2$. Two vertical stresses values as 0.2MPa and 0.5MPa were applied to represent different number of stories. The boundary conditions on the piers resembles those in the full-scale tests, thus calculations will be relevant to its position in the full-scale building. The value of the effective pier height H_o is calculated following the work of Lang Lang, (2002), who used the relative stiffness between the piers and spandrels. Note that H_o is equal to $0.5h$ in case of cantilever and equal to h in case of fixed-fixed boundary conditions. Samples **A** and **B** use *double leaf wall sections with some through stones* resembling a typical construction in Italy using partially worked natural stones from Bergamo, originating from calcareous sedimentary sandstones, having $f_m = 165-172$ MPa, $\rho = 2579$ Kg/m³, f_f (flexural strength) = 19 MPa and modified mortar from a pre-mixed natural hydraulic lime by adding sand at a ratio of 2 Kg sand to 11 Kg mortar resulting in an average $f_m = 1.71-1.78$ MPa after 28 days curing.

Regarding the 2nd experimental data set, samples **WS**, **WI** and **WR** have the same geometry obtained from the average of 24 samples. The unit masonry used to build the walls are two-mica medium coarse granite meant to represent the ancient constructions in Northern Portugal. Three settings of vertical stresses are used on each type of the piers, for reflecting different loading scenarios listed as: 0.5MPa, 0.875MPa and 1.25MPa. Boundary conditions are set as cantilever

using steel rollers resulting in $H_o = h$. The values for f_m are based on prism tests Vasconcelos & Lourenço, (2009) for **WS** prototypes and modified for **WI** and **WR** to fit the numerical simulation. Using correction factors from (CSA, 2014) gives a new diagonal shear value of 65.7MPa for WS prototype. Values for shear and tensile strengths are calculated according to the formulas extracted from diagonal shear tests based on the maximum shear and principle stresses $f_v = 0.707 \times P/A_g$ and $f_t = 0.5 \times P/A_g$ (ASTM 519-02, 2002) and (RILEM, 1994). It is important to note that the pier samples are scaled 1:3 of the actual walls found in heritage buildings which can affect the results.

Regarding the 3rd experimental data set, samples **SW** are composed of 7 walls with 4 different vertical stress levels: 0.15MPa, 0.5MPa, 1MPa and 1.25MPa. The stone units used are Montjuic Stone being a local material of Catalonia and characterized by a homogenous surface with unit compressive strength of 82.7 MPa, density of 25 KN/m³, and unit tensile strength of 3.7MPa. A monotonic loading was applied on all the specimens with fixed-fixed boundary conditions limiting the effective height H_o to $0.5h = 500mm$. Two walls were tested for each vertical stress level except the highest one. The friction parameter was extracted from direct shear tests applied on the same unit stones (Lourenço & Ramos, 2004) to be 0.62 and the cohesion strength was taken as zero due to the absence of mortar. The compressive strength of prisms built using the same unit stones (Oliveira, 2003) are used to obtain the compressive strength of the walls depending on the correlation made by Krefeld, (1938) that defines correction factors for compressive strength of solid brick masonry due to the variation in the height/thickness ratio of the samples used. The four stones prisms with $h_p/b_w = 2$ have an average compressive strength of 52MPa while the tested walls have an $h/b_w = 5$ which gives a correction factor of 1.42 that modifies the compressive strength of the walls to $f_m = 52/1.42 = 36.62MPa$.

For all aforementioned tests, the specimens' geometry ($L_w \times h \times b_w$) and vertical stresses (not including own weight) are given in Table 3.2. The results from experimental tests for maximum shear capacity, V_u , yielding displacement (Δ_{y1}) and ultimate lateral displacements (Δ_{u1}) are also presented. All the samples are loaded using the displacement-based mode until failure occurred; Δ_{u1} is the ultimate displacement of the pier and Δ_{y1} is the yielding displacement of the pier extracted from experimental data. In specimens **A** and **B**, the only variables are the geometry and the vertical stresses which makes it valid to limit the comparisons for those two.

Table 3.2: Geometry, vertical stresses, and capacity results from the experimental tests on piers

Specimen	Geometry [mm]	Vertical Stress [MPa]	V_u [kN]	Failure Mode	Δ_{y1} [mm]	Δ_{u1} [mm]
A1	2500x2500x320	0.2	126.0	DS (diagonal shear)	1.62	9.60
A2	2500x2500x320	0.5	202.0	DS	1.82	7.85
B1	1250x2500x320	0.2	44.0	DS	1.22	17.00
B2	1250x2500x320	0.5	83.0	DS	2.96	9.35
WS1	1000x1200x200	0.5	36.9	DS	2.87	32.70
WS2	1000x1200x200	0.875	62.9	DS	3.36	32.31
WS3	1000x1200x200	1.25	86.3	DS	4.29	32.31
WI1	1000x1200x200	0.5	37.6	DS	2.83	37.40
WI2	1000x1200x200	0.875	55.7	DS	3.29	29.20
WI3	1000x1200x200	1.25	83.0	DS	3.59	25.66
WR1	1000x1200x200	0.5	36.4	DS	2.71	33.97
WR2	1000x1200x200	0.875	63.8	DS	3.81	24.15
WR3	1000x1200x200	1.25	66.0	DS	2.94	10.28
SW30.1	1000x1000x200	0.15	22.0	DS	3.00	17.00
SW30.2	1000x1000x200	0.15	23.0	DS	3.00	17.00
SW100.1	1000x1000x200	0.50	42.0	DS	2.50	13.00
SW100.2	1000x1000x200	0.50	49.0	DS	2.50	12.50
SW200.1	1000x1000x200	1.00	72.0	DS	4.00	16.00
SW200.2	1000x1000x200	1.00	69.0	DS	4.00	12.50
SW250	1000x1000x200	1.25	102.0	DS	2.50	9.00

The results from the experimental loading tests are then transformed into bilinear curve properties to facilitate the modeling procedure of these piers. In samples **WS**, **WI** and **WR** the texture and the vertical stresses are the main variables and thus their influence on the lateral behavior will be

considered. Specimens **SW** have four different levels of vertical stresses using same texture as **WS** thus it will be used as a confirmation for the results.

To determine the displacements of the piers, drift ratio limits from recent design codes for masonry construction are used to evaluate their accuracy and their practicality in terms of representing the masonry lateral behavior. The yielding displacement values, Δ_{y1} , are calculated from FEMA 356, (2000) using drift limit 0.075-0.1%, while the ultimate displacements Δ_{u1} are calculated using drift limit 0.4% for shear failures extracted from NTC08, (2008) and EN08-3, (2005). Using the mentioned codes, specimens **A** and **B** of 2500mm heights show yielding displacement of $\Delta_y = 2.5\text{mm}$ and ultimate displacement of $\Delta_u = 10\text{mm}$. Samples **WS**, **WI** and **WR** of 1200mm height show $\Delta_y = 1.2\text{mm}$ and $\Delta_u = 4.8\text{mm}$. The approximate experimental displacements of the piers in samples **SW** are extracted from the graphs (Oliveira, 2003) where the yielding values corresponds to the end of the linear phase and the ultimate values corresponds to shear capacities after 20% decay from the maximum shear developed in the wall. Following the codes mentioned earlier and given the height of 1000mm, it results $\Delta_y = 1.0\text{mm}$ and $\Delta_u = 4.0\text{mm}$.

Applying the preliminary mechanical properties on the four formulations provided in Eqs. (3.1), (3.2), (3.3) and (3.4), the results obtained for all specimens are shown in Table 3.3. The displacement ratios are calculated from dividing the experimental results by the ones obtained from the codes. The divergence index values obtained through dividing the experimental shear capacities by the numerical ones are also presented.

Table 3.3: Results of maximum shear, ultimate and yielding displacement ratios and shear capacity ratios resulting from the formulations.

Specimen	$V_{u,1}$ [KN]	$V_{u,2}$ [KN]	$V_{u,3}$ [KN]	$V_{u,4}$ [KN]	$V_u/V_{u,1}$	$V_u/V_{u,2}$	$V_u/V_{u,3}$	$V_u/V_{u,4}$	Δ_{y1}/Δ_y	Δ_{u1}/Δ_u
A1	123.10	188.20	145.68	89.72	1.02	0.67	0.86	1.40	0.65	0.96
A2	155.80	248.40	199.94	178.99	1.30	0.81	1.01	1.12	0.73	0.79
B1	76.10	62.74	75.01	20.29	0.58	0.70	0.58	2.17	0.49	1.70
B2	108.50	82.82	102.94	31.57	0.76	1.00	0.81	2.60	1.18	0.94
WS1	N/A	N/A	31.39	41.93	N/A	N/A	1.18	0.88	2.39	6.81
WS2	N/A	N/A	53.55	71.28	N/A	N/A	1.17	0.88	2.80	6.73
WS3	N/A	N/A	75.71	100.44	N/A	N/A	1.14	0.86	3.58	6.73
WI1	34.70	46.59	63.15	39.55	1.08	0.81	0.60	0.95	2.36	7.79
WI2	44.83	58.49	84.63	64.60	1.24	0.95	0.66	0.86	2.74	6.08
WI3	54.95	68.34	106.11	86.74	1.51	1.21	0.78	0.96	2.99	5.35
WR1	33.01	44.26	N/A	N/A	1.10	0.82	N/A	N/A	2.26	7.08
WR2	43.13	55.72	N/A	N/A	1.46	1.15	N/A	N/A	3.18	5.03
WR3	53.26	65.20	N/A	N/A	1.24	1.01	N/A	N/A	2.45	2.14
SW30	N/A	N/A	14.47	14.94	N/A	N/A	1.55	1.51	3	4.25
SW100	N/A	N/A	43.40	44.63	N/A	N/A	1.05	1.02	2.5	3.19
SW200	N/A	N/A	84.72	86.56	N/A	N/A	0.83	0.81	4	3.56
SW250	N/A	N/A	105.40	107.32	N/A	N/A	0.97	0.95	2.5	2.25

Samples **A** and **B** show good correlation to some extent regarding the displacement ratios where most of the numbers are close to one validating the drift limits offered by the codes except in specimen **B1** which diverge from the experimental results by extra 70% for ultimate displacement and 50% short for the yielding displacement. This could be justified by the fact that this slender specimen experienced a flexural behavior at the beginning of the lateral shaking before transforming into shear behavior and failing as so. Flexural behavior tends to be more flexible and allows more displacement estimated by the codes to have drift limit of 0.6%. Substituting this value will give a drift limit at ultimate displacement $\Delta_u = 15\text{mm}$ which is a more reasonable answer compared to the experimental results. The divergence values from the CSA formulation in Eq. (3.1) show good correlation with squat piers especially for low vertical stresses; hence providing a feasibility index of 1.02. Eq. (3.2) shows excellent correlation with the slender pier with high vertical stresses with an index of 1.00. Eq. (3.3) can simulate good values for the squat pier with high vertical stresses with an index of 1.01. Finally, Eq. (3.4) has better simulation for the shear capacities for the squat piers especially for high vertical stresses with an index of 1.12.

Samples **WS**, **WI** and **WR** are numerated 1 to 3 referring to the increased level of vertical stresses on the piers. The dominating failure mode is in the form of stepped diagonal cracks along the masonry-mortar interface which is the mode represented by the proposed formulations. Some of the specimens develop mixed failure modes including diagonal shear and flexural rocking at the bottom which will be tackled in the case of divergence of the results. The flexural failure in certain specimens is considered as outliers and their values were neglected. Some missing values for masonry assemblages limit the analysis to certain formulations depending on the required parameters. A substantial divergence index value in the results of yielding and ultimate displacements are noticed, which could be due to the scaling factor. Regarding the divergence index for shear capacity ratios, Eq. (3.4) shows fair correlation with the **WS** prototypes with a maximum of 14% difference from the experimental results. It also shows better simulation for the **WI** prototypes reaching a maximum of 96%. Not much difference was observed between different levels of vertical stresses on the piers. Eq. (3.3) shows fair results for the **WS** prototypes with a maximum divergence index of 18% and less fair results for the **WI** prototypes reaching 40% divergence index for lower level of stresses and 22% divergence index for the maximum level of stress. Eq. (3.1) shows a big variation within the levels of stresses imposed on the piers. For **WI** prototypes, the divergence index increases with the increase of the vertical stresses ranging between 8% and 51%. As for the **WR** prototypes, the best simulation is obtained for the lowest vertical stress and the weaker is obtained with the second level of vertical stress. Equation (3.2) shows similar divergence index for the lowest and highest vertical stress levels corresponding to **WI** prototype, while it shows a good simulation for the middle level reaching the index of 95%. As for the **WR** prototype the best simulation is for the highest level of vertical stress.

For **WS** samples, a step diagonal crack indicating a diagonal shear failure was observed in all the specimens. Coulomb criterion and Lourenco formulation have very similar values of capacity shears through the different vertical stress levels available. A 50% divergence index is realized at 0.15MPa vertical stress level and a 20% divergence index for 1.00MPa vertical stress level. The simulation of shear stress level at 0.5MPa and 1.25MPa, respectively, showed good matching, reaching 97% in some samples. As for the displacement ratios, again a large divergence in the results was obtained like the previous tests due to the scaled dimensions of the available specimens.

Graphical representation of the data acquired by the tests versus the ones obtained from the shear capacity formulations are plotted to enhance the visualization of the information. The comparisons will take place within each graph individually assessing the influence of vertical stress variations. Another comparison is between similar graphs with one variable to understand its influence on the results. Also, comparisons between graphs from different experiments if justified with enough similarities is used to include additional parameters.

Samples **A1** and **A2** represent the full-scale squat piers with irregular or partially worked texture. According to Fig. 3.1a, Coulomb criterion seems to have the best simulation for the experimental data (samples **A1** and **A2**) with perfect match at 0.5MPa vertical stress. Equation (3.2) shows higher values while Equation (3.4) shows lower results. CSA formulation gives a good match for 0.2 MPa vertical stress followed by a low slope of variation in shear capacity compared to the rest of the data. In Fig. 3.1b is depicted the response of samples **B1** and **B2**, representing the full-scale slender piers with irregular texture. CSA and Coulomb criterion show similar results both being higher than the experimental data. Equation (3.4) appears to have a wide divergence in the results being lower than the experimental data. Equation (3.2) shows a good match at 0.5 MPa but higher values at 0.2 MPa vertical stress on the pier. It is noticeable that the formulations perform better

with squat piers since those with more slenderness lean towards the flexural behavior which is evident in sample **B1**.

The samples WS, WI and WR represent scaled squat piers with sawn, irregular and rubble textures, respectively. In Fig. 3.1c is depicted the shear and tensile strength of WS dry walls (stones without any mortar) using Coulomb and Lourenco et al. equations; the other equations are not used due to the limit for dry stones pier. Both formulations deviated from the experimental curve with values more accurate at 0.2MPa.

Figure 3.1d shows the variation of shear capacities of proposed formulations in comparison to the experimental values for the for WI specimens. As depicted, the shear capacity using Eq. (3.4) provides good values compared to the experimental for vertical stresses of 0.5MPa and 1.25MPa. Conversely, Eq. (3.2) simulates well the results for the middle vertical stress level at 0.875MPa. Meanwhile, Eq. (3.1) also gives good shear results at 0.5MPa vertical shear, while it diverges for high stress values. Then, the shear computed using Eq. (3.3) provides much greater value than experimental data.

Figure 3.1e shows shear capacity of specimens WR computed according with Eqs. (3.1) and (3.2) against the shear capacity resulted from experimental tests. The other equations are not used due to the lack of friction criteria and compressive strength of rubble textures in the literature. As depicted, Eq. (3.1) gives good simulation for shear at 0.5MPa and less accurate for 1.25MPa and 0.875MPa in comparison with the experimental values. Conversely, the shear computed with Eq. (3.2) gives good results for 1.25MPa and diverges for 0.875MPa and 0.5MPa stress values.

Figure 3.1f displays the graph for SW samples that are scale with sawn texture and dry joints. Eqs. (3.3) and (3.4) provide close results for shear capacities when comparing with shear values from

experimental tests associated with 0.5MPa and 1.25MPa vertical stresses, while it diverges slightly for 0.15MPa and 1MPa stresses.

The information regarding the most common parameters collected based on the selected samples, as well as the ratios of shear resulted experimentally and that calculated using equations are presented in Table 3.4. The first four parameters provided in columns (1) – (4) are labeled primary parameters and these parameters are: (1) aspect ratio = pier height, h , divided by the width, L_w , (2) TR = texture of the unit stones used in the piers, (3) VS = Vertical Stress excluding the own weight and, (4) SC = scale of pier specimen. The following set of four parameters from (5) to (8), labeled secondary parameters, are: (5) BC = boundary conditions, (6) CS = cross section of the wall sample, (7) UST = unit stone material type depending on the origin and, (8) MT = mortar type depending on its strength. Although these parameters are considered as minor, they will be accounted in the analysis even if the conclusion about their influence is not conclusive. The last four columns represent the ratio of shear of sample from test to that resulted from the perspective of each formulation. The divergence factor (DF) is used to assess the overall performance of each equation regarding a major parameter, while the equation is provided below.

$$DF = \sum_1^n |V_u/V_{u,i} - 1| / n \quad (3.10)$$

where n is the number of samples and i is the number of the equation.

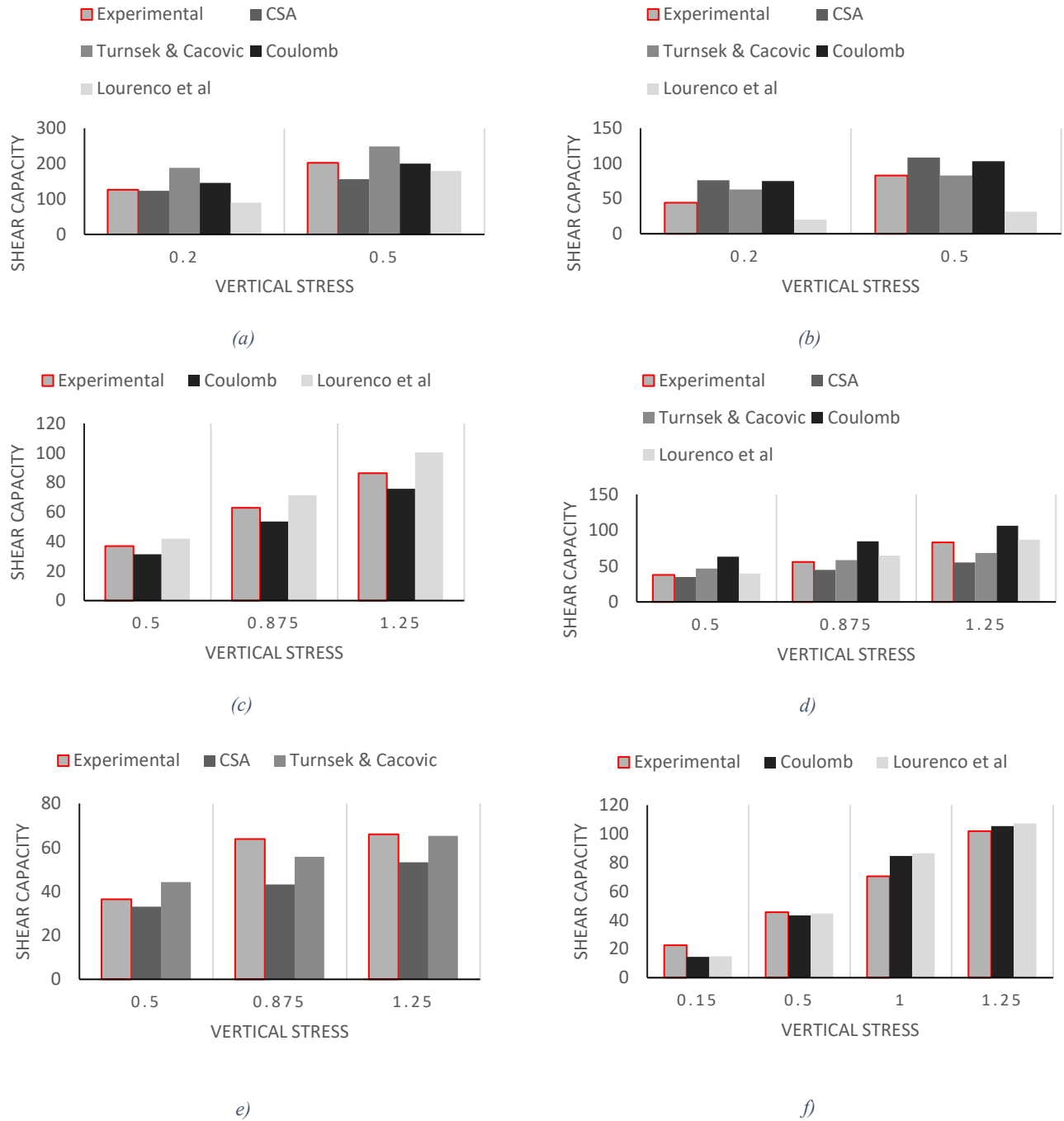


Figure 3.1: a) Shear capacities versus vertical stresses for specimens A1 and A2 b) B1 and B2 c) WS prototypes d) WI prototypes e) WR prototypes f) SW prototypes.

Using Eq. (3.1), given in CSA/S304, it shows better results with lower vertical stress levels based on the comparison of the major set **A1** and **A2** for an aspect ratio of 1.0, as per column (1). However, for an aspect ratio of 2 associated with samples **B1** and **B2**, the formulation shows better

results with higher stress levels. Beholding the major sets **A1** and **B1**, as well as, **A2** and **B2** suggests that the CSA/S304 equation, Eq. (3.1), provides better results for aspect ratio of 1, especially at lower levels of stress.

Table 3.4: Variation of capacity shear indices and divergence factors in terms of the different parameters for each specimen

Spec.	h/L _w	TR	VS	SC	BC	CS	UST	MT	V _u /V _{u1}	V _u /V _{u2}	V _u /V _{u3}	V _u /V _{u4}
	(1)	(2)	(3)	(4)	(5)	(6)	(7)	(8)	(9.1)	(9.2)	(9.3)	(9.4)
	Primary				Secondary				Indices			
A1	1	IR ¹	0.2	FS ⁴	RL ⁶	DL ⁹	SS ¹¹	W ¹⁴	1.02	0.67	0.86	1.40
A2	1	IR	0.5	FS	RL	DL	SS	W	1.30	0.81	1.01	1.12
DF									0.16	0.26	0.08	0.26
B1	2	IR	0.2	FS	RL	DL	SS	W	0.58	0.70	0.58	2.17
B2	2	IR	0.5	FS	RL	DL	SS	W	0.76	1.00	0.81	2.60
DF									0.33	0.15	0.31	1.39
WS1	1.2	SW ²	0.5	S ⁵	C ⁷	SL ¹⁰	G ¹²	DJ ¹⁵	N/A	N/A	1.18	0.88
WS2	1.2	SW	0.875	S	C	SL	G	DJ	N/A	N/A	1.17	0.88
WS3	1.2	SW	1.25	S	C	SL	G	DJ	N/A	N/A	1.14	0.86
DF									-	-	0.16	0.13
WI1	1.2	IR	0.5	S	C	SL	G	W	1.08	0.81	0.60	0.95
WI2	1.2	IR	0.875	S	C	SL	G	W	1.24	0.95	0.66	0.86
WI3	1.2	IR	1.25	S	C	SL	G	W	1.51	1.21	0.78	0.96
DF									0.28	0.15	0.32	0.08
WR1	1.2	RB ³	0.5	S	C	SL	G	W	1.10	0.82	N/A	N/A
WR2	1.2	RB	0.875	S	C	SL	G	W	1.46	1.15	N/A	N/A
WR3	1.2	RB	1.25	S	C	SL	G	W	1.24	1.01	N/A	N/A
DF									0.27	0.11	-	-
SW30	1	SW	0.15	S	FF ⁸	SL	SR ¹³	DJ	N/A	N/A	1.55	1.51
SW100	1	SW	0.5	S	FF	SL	SR	DJ	N/A	N/A	1.05	1.02
SW200	1	SW	1	S	FF	SL	SR	DJ	N/A	N/A	0.83	0.81
SW250	1	SW	1.25	S	FF	SL	SR	DJ	N/A	N/A	0.97	0.95
DF									-	-	0.2	0.19

¹ Irregular texture referring to unit stones partially worked.

² Sawn texture referring to unit stones fully worked.

³ Rubble texture referring to random shape unit stones.

⁴ Full scale specimen based on a typical stone masonry construction.

⁵ Scaled specimen based on a typical stone masonry construction.

⁶ Boundary conditions resembling actual construction practices.

⁷ Cantilever or fixed-free boundary conditions and ⁸ Fixed-fixed boundary conditions.

⁹ Double-leaf cross section wall and ¹⁰ Single-leaf cross section wall.

¹¹ Sandstone; ¹² Granite and ¹³ Siliceous rocks.

¹⁴ Weak mortar and ¹⁵ Dry joints.

Referring to samples: WI1, WI2, WI3, WR1, WR2, and WR3 that have an aspect ratio of 1.2, it shows that Eq. (3.1) provides better results as the level of vertical stresses decreases. Major sets

such as: **WI1** and **WR1**; **WI2** and **WR2**; **WI3** and **WR3**, where the variations between irregular and rubble textures is considered, indicate very similar results at lower stress levels and divergence in the results at higher stress levels with no privilege for any category.

Observing the set **A2** and **WI1** with irregular texture and close aspect ratios, it allows an enhancement in the results for the **WI1** sample from a 1.3 to 1.08 shear ratio index. This shows that the secondary parameters can influence the results. The $DF = 0.16$ for samples **A1** and **A2** which shows that Eq. (3.1) given in CSA/S304 better represents the full-scale squat piers.

The major sets **A1-A2** and **B1-B2** illustrate that Eq. (3.2) shows better results with higher vertical stress levels. Moving to major sets **A1-B1** and **A2-B2**, the results are enhanced for samples with an aspect ratio of 2 versus aspect ratio of 1 especially at high vertical stress levels. Major set **WI1**, **WI2**, **WI3** shows good correlation of results at mid vertical stress levels while the major set **WR1**, **WR2**, **WR3** indicates better results at high pre-stress levels. Major sets **WI1-WR1**, **WI2-WR2** and **WI3-WR3**, considering the variations between irregular and rubble textures have very similar behavior as Eq. (3.1). Observing the minor set **A2-WI1** it shows the same results indicating minor effect of secondary parameters when using Eq. (3.2). The $DF = 0.11$ for the samples **WR** indicates that it best represents the rubble texture.

Eq. (3.3) gives better results for higher vertical stress levels referring to the major sets **A1-A2** and **B1-B2**. While comparing the major sets **A1-B1** and **A2-B2** it is evident that the performance of Eq. (3.3) is more compelling for aspect ratio of 1. For major set **WS1**, **WS2**, **WS3** the performance is better as the level of vertical stress increases. The same behavior is associated with the major sample **WI1**, **WI2**, **WI3**. Observing the major sets **WS1-WI1**, **WS2-WI2** and **WS3-WI3** it imposes a better performance of the formulation regarding the sawn samples versus the irregular

samples. The major set **SW30-SW100-SW200-SW250** shows good results for 0.5MPa and 1.25MPa vertical stress levels, fair performance for 1MPa and poor performance for 0.15MPa. The minor set **A2-WI1** illustrates a big advantage to the sample **A2**. Minor sets **WI1-SW100** and **WI3-SW250** shows better results for the **SW** samples. This indicates that the secondary parameters have great influence on the performance of the Coulomb criterion. The $DF = 0.08$ for samples **A1** and **A2** shows a good correlation with the squat piers.

Eq. (3.4) has more accurate results at high vertical stress levels referring to the major set **A1-A2**. A greater divergence in the results is indicated by the major samples **A1-B1** and **A2-B2** that shows a poor performance with slender piers. Major sets **WI1**, **WI2**, **WI3** and **WR1**, **WR2**, **WR3** shows very similar shear ratio indices for different vertical stress levels on the piers. Observing the major sets **WS1-WI1**, **WS2-WI2** and **WS3-WI3** imposes a better performance for the irregular texture compared to the sawn texture. The major set **SW30**, **SW100**, **SW200**, **SW250** shows similar behavior to Eq. (3.3). The minor set **A2-WI1** indicates a slight advantage for the sample **WI1**. The minor sets **WI1-SW100** and **WI3-SW250** shows better results for the **SW** samples. This indicates that the secondary parameters have a small influence on the performance of the Coulomb criterion. The $DF = 0.08$ for the **WI** samples shows a good correlation with the irregular texture.

3.2.2 Experimental Campaign for Flexural Capacity

Experiments from five testing programs are used to validate the proposed formulations used to predict the maximum shear force resulting from flexural behavior of the piers. The first data collection is from tests conducted at the University of Brescia, Italy (Silva et al., 2014); hence 16 samples split between **FS-NI** and **FS-I** series were collected. The second testing program selected was conducted by Lee et al., (2008) using 7 samples referred to as the **H series** in this work. The third experiment program selected was performed at the École Polytechnique Federale de

Lausanne laboratory (Petry & Beyer, 2015a) using two samples named as the **P series**. The fourth are ten samples selected from the experimental campaign at the ZAG Laboratory (Bosiljkov et al., 2003) that are averaged into four samples named as **Sample 10** series and **Sample 11** series (Bosiljkov & Tomažević, 2006). The last samples are selected from the EUCENTRE and Pavia University Lab experimental campaign (Magenes et al., 2008b) as part of the ESECMaSE Project (Magenes et al., 2008a) regarded as the **CL** and **CS** series. The mechanical properties of the samples are extracted from preliminary characterization tests associated directly with the main campaign or inferred from similar typologies found in the literature. The results are listed in Table 3.5 including the compressive strength of the masonry walls wallets f_m and the densities of the masonry units ρ_s used in the construction of the walls.

Table 3.5: Preliminary mechanical parameters for masonry assemblages

Specimen	f_m [MPa]	ρ_s [kg/m ³]	ρ_{f1} [kg/m ³]	ρ_{f2} [kg/m ³]
FS-NI (Silva et al. 2014)	2.49	2660	2263	-
FS-I (Silva et al. 2014)	4.89	2660	2263	-
S-NI (Silva et al. 2014)	2.41	2660	-	2216
S-I (Silva et al. 2014)	4.28	2660	-	2216
H (Lee et al. 2008)	4.38	-	-	-
P (Petry & Beyer, 2015)	5.87	901	-	-
10A, 10B (Bosiljkov et al.2003)	4.05	901	-	-
10C (Bosiljkov et al.2003)	4.25	901	-	-
11A (Bosiljkov & Tomazevic 2006)	4.21	901	-	-
CL6 (Magenes et al., 2008a)	10	901	-	-
CS (Magenes et al., 2008b)	6.2	1852	-	-

Three-leaf specimens from the first campaign are used to assess the effect of mortar injection or strengthening on the behavior of the masonry piers. Thus **FS-I** samples denote the full-scale injected piers while the **FS-NI** stands for the full scale non-injected piers as a control. Same samples are scaled to a factor of 2:3 represented by the **S-NI** and **S-I** referring to the scaled non-injected and scaled injected piers respectively. Each series has four samples, each with different

vertical stress level. The outer layers of the walls are built using three types of stones with irregular texture: red stone, regular white and irregular white where their average density $\rho_s = 2660 \text{ kg/m}^3$. A natural hydraulic lime (NHL) weak mortar is initially used to fill the head and bed joints then a stronger NHL mortar is used for the strengthening through injection. The inner layer is made of limestone fragments and mortar with a density $\rho_{fl} = 2263 \text{ kg/m}^3$ for the non-injected specimens and $\rho_{f2} = 2216 \text{ kg/m}^3$ for the injected specimens. The boundary condition of all the samples is cantilever or fixed-free with a generally consider low aspect ratio. The major parameters that can be analyzed are the vertical stress level, the scaling factor and the effect of the mortar injection.

Seven **H** samples are built in the second campaign using clay masonry units or bricks. Three different cross sections are utilized differing between 1 leaf, 2 leaf and half-leaf walls. Cement mortar with medium strength is used in the head and bed joints. All the samples have a cantilever boundary condition. Prism test within the same experimental tests yielded an $f_m = 6.18 \text{ MPa}$ which is then modified for a wallet sample using modification factors (Krefeld, 1938) to give $f_m = 4.38 \text{ MPa}$. Two vertical stress levels are used on the piers to account for the floor levels in the buildings under examination. Four aspect ratios are available in those samples: squat, two slender and flat.

Specimens **P3** and **P4** are built using Swiss hollow clay masonry and cement based mortar (Petry & Beyer, 2015b). Two levels of vertical stress levels are used with a boundary condition resembling weak coupling due to weak restraints applied by the relatively low stiff spandrel on the adjacent piers. In this case $H_o = 1.5h$ and the pier is considered as a cantilever (Petry & Beyer, 2014a). The 1-leaf walls are built with masonry units of density $\rho_s = 901 \text{ kg/m}^3$ (Petry & Beyer, 2014b) using the full scale scheme.

At the ZAG Laboratory two typologies are considered in the case study. Samples **10-A**, **10-B** and **11-A** are fully mortared which indicates the placement of the medium strength mortar throughout

the head and bed joints. Sample **10-C** has only applied mortar in the bed joints. All samples are full scale built using clay brick masonry units. The boundary conditions are cantilever. The main parameters that can be analyzed from those samples are the vertical stress levels and the typology (Frumento et al., 2009).

At the EUCENTRE Laboratory sample **CL6** is selected. The sample was built using clay masonry with doubly fixed boundary conditions thus making $H_o = 0.5h$. The pier has a slender aspect ratio with a compressive strength $f_m = 10\text{MPa}$. Another four samples are selected built using calcium-silicate masonry units iterated between two aspect ratios (slender – squat) and two boundary conditions (cantilever – doubly fixed). The walls have a compressive strength $f_m = 6.2\text{MPa}$ and density $\rho_s = 1852 \text{ Kg/m}^3$ (Graziotti et al., 2016). The parameters regarding the vertical stress levels, boundary conditions for slender and squat piers and the aspect ratio for cantilever and doubly fixed piers can be inferred from this experiment.

The geometry of the specimens and the experimental results for the shear and ultimate displacement capacities are presented in Table 3.6. It is important to note that the gravity loads exclude the own weight of the walls that needs to be calculated using the densities of the masonry units mentioned earlier, except for the **H** series where the own weight of the walls is already included in the given values. Most of the specimens had the rocking failure mode followed by toe crushing mode, while some samples experience both modes. Another case is when the pier experiences flexural and shear failure patterns due to sudden loss in strength during the lateral shaking. Those samples are indicated to have a hybrid cracking pattern as illustrated in Table 3.6. The geometry of the piers is listed as $L_w \times h \times b_w$ that are used to calculate the volume and the aspect ratio. The ultimate displacements was compared to the values proposed by (EN08-3, 2005) for the flexural behavior of the piers. The following equation $\Delta_u = (0.008H_o/L_w) \times h$ is utilized to

calculate the ultimate displacement for all the selected samples in this study. The ratios of the experimental to the numerical ultimate displacements are presented in Table 3.7 along with the maximum shear capacity generated from the Eqs. (3.5), (3.6), (3.7), (3.8) and (3.9). Also, the ratios of the experimental to numerical maximum shear capacities are listed below to highlight the accuracy of the formulations. Values closer to one have the best correlations. Ratios that are within

Table 3.6: Geometry, vertical stresses, and capacity results from the experimental tests on piers

Specimen	Geometry [mm]	Stress [MPa]	V _u [KN]	Failure Mode	Δ _{u1} [mm]
FS-NI-0.5	1000x1200x500	0.50	74.67	R ¹	10.50
FS-NI-0.75	1000x1200x500	0.75	76.00	H ²	4.00
FS-NI-1	1000x1200x500	1.00	116.00	H	7.00
FS-NI-1.25	1000x1200x500	1.25	104.00	TC ³	3.00
FS-I-1	1000x1200x500	1.00	172.00	R	22.00
FS-I-1.25	1000x1200x500	1.25	208.00	R	18.00
FS-I-1.5	1000x1200x500	1.50	214.67	R	7.00
FS-I-2	1000x1200x500	2.00	257.33	R	7.80
S-NI-0.5	800x1000x330	0.50	28.00	R	5.50
S-NI-0.75	800x1000x330	0.75	68.00	R	7.00
S-NI-1	800x1000x330	1.00	53.33	R	7.00
S-NI-1.25	800x1000x330	1.25	73.33	R	6.50
S-I-1	800x1000x330	1.00	89.30	R	19.00
S-I-1.25	800x1000x330	1.25	102.67	R	14.00
S-I-1.5	800x1000x330	1.50	102.67	R	8.90
S-I-2	800x1000x330	2.00	117.30	TC	6.20
H1	2700x2700x190	0.086*	84.14	R	50.72
H2	2700x2700x190	0.250*	136.12	R, TC	43.92
H3	2700x2700x90	0.250*	103.75	R, TC	29.70
H4	2700x2700x250	0.250*	138.57	R, TC	59.12
H5	1200x2700x190	0.250*	35.89	R	77.55
H6	1800x2700x190	0.250*	63.43	R, TC	53.35
H7	3600x2700x190	0.250*	195.84	R, TC, SL ⁴	40.70
P3	2010x2250x200	1.04	121.00	R	15.53
P4	2010x2250x200	1.54	145.00	H	7.88
10-A	1028x1511x300	0.60	59.00	R	26.90
10-B	1028x1511x300	1.19	107.00	R	11.79
10-C	985x1508x300	1.19	109.99	R	12.37
11-A	2567x1750x297	0.59	290.00	R	23.98
CL6	1250x2600x300	0.50	84.5	R	50.70
CS5	1250x2500x175	1.00	96.2	R	43.20
CS6	1250x2500x175	1.00	41.3	R	44.20
CS7	2500x2500x175	1.00	218.8	R	30.10
CS8	2500x2500x175	1.00	155	R	21.00

¹R: Rocking ²H: Hybrid ³TC: Toe Crushing ⁴SL: Sliding

*Pre-stress values for H specimens include the own weight of the walls.

20% divergence from the experimental results are present in samples **FS-NI-0.5**, **S-I-1.5**, **CS6** and **CS8**. Only a small portion out of the 34 samples available in this study gave good results, which indicates that the estimation provided by EC8 is limited to certain application and cannot be generalized for most unreinforced masonry lateral displacements.

Table 3.7: Results of maximum shear, ultimate and yielding displacement ratios and shear capacity ratios resulting from the formulations.

Specimen	V_{u,5} [kN]	V_{u,6} [kN]	V_{u,7} [kN]	V_{u,8} [kN]	V_{u,9} [kN]	V_u/V_{u5}	V_u/V_{u6}	V_u/V_{u7}	V_u/V_{u8}	V_u/V_{u9}	Δ_{u1}/Δ_u
FS-NI-0.5	85.8	99.5	79.1	178.8	85.0	0.87	0.75	0.94	0.42	0.88	0.91
FS-NI-0.75	104.1	146.4	86.6	244.9	107.4	0.73	0.52	0.88	0.31	0.71	0.35
FS-NI-1	110.2	193.2	90.3	314.2	118.4	1.05	0.60	1.28	0.37	0.98	0.61
FS-NI-1.25	104.0	240.1	67.9	387.3	118.4	1.00	0.43	1.53	0.27	0.88	0.26
FS-I-1	164.4	193.2	152.4	243.3	165.7	1.05	0.89	1.13	0.71	1.04	1.91
FS-I-1.25	186.8	240.1	168.4	289.8	191.1	1.11	0.87	1.24	0.72	1.09	1.56
FS-I-1.5	203.0	287.0	176.9	337.4	210.7	1.06	0.75	1.21	0.64	1.02	0.61
FS-I-2	216.5	380.7	170.9	436.1	232.7	1.19	0.68	1.51	0.59	1.11	0.68
S-NI-0.5	42.5	49.9	39.1	124.1	42.3	0.66	0.56	0.72	0.23	0.66	0.55
S-NI-0.75	51.5	73.7	44.4	171.0	53.3	1.32	0.92	1.53	0.40	1.28	0.70
S-NI-1	54.0	97.5	41.9	220.0	58.4	0.99	0.55	1.27	0.24	0.91	0.70
S-NI-1.25	50.2	121.2	31.5	272.5	57.5	1.46	0.61	2.33	0.27	1.28	0.65
S-I-1	78.8	97.5	72	175.6	80.2	1.13	0.92	1.24	0.51	1.11	1.90
S-I-1.25	88.2	121.2	77.7	210.7	91.2	1.16	0.85	1.32	0.49	1.13	1.40
S-I-1.5	93.9	145.0	79.0	246.8	98.9	1.09	0.71	1.30	0.42	1.04	0.89
S-I-2	94.5	192.5	68.4	322.4	104.2	1.24	0.61	1.71	0.36	1.13	0.62
H1	21.6	19.85	21.4	61.1	21.6	3.90	4.24	3.92	1.38	3.90	2.35
H2	59.8	57.7	58.9	111.7	60.2	2.27	2.36	2.31	1.22	2.26	2.03
H3	28.3	27.3	27.9	76.9	28.5	3.66	3.79	3.72	1.35	3.64	1.38
H4	78.3	75.9	77.5	128.1	79.2	1.77	1.82	1.79	1.08	1.75	2.74
H5	11.8	11.4	11.6	33.1	11.9	3.04	3.15	3.08	1.08	3.02	1.60
H6	26.6	25.7	26.2	60.8	26.8	2.39	2.47	2.42	1.04	2.37	1.65
H7	106.4	102.6	104.8	171.9	107.0	1.84	1.91	1.87	1.14	1.83	2.51
P3	150.0	171.3	141.1	222.3	153.1	0.81	0.71	0.86	0.54	0.79	0.51
P4	192.6	252.2	173.8	303.4	199.5	0.75	0.58	0.83	0.48	0.73	0.26
10-A	52.9	57.9	50.4	108.0	53.8	1.12	1.02	1.17	0.55	1.10	1.51
10-B	82.1	113.6	72.7	185.1	85.6	1.30	0.94	1.47	0.58	1.25	0.66
10-C	77.5	104.5	69.2	170.9	80.5	1.41	1.04	1.58	0.64	1.35	0.67
11-A	284.3	304.9	269.1	359.4	285.9	1.02	0.95	1.08	0.81	1.01	2.51
CL6	88.6	84.9	87.31	131.8	89.0	0.95	0.99	0.97	0.64	0.95	2.34
CS5	91.7	103.0	86.9	179.2	93.5	1.05	0.93	1.11	0.54	1.03	2.16
CS6	45.9	51.5	43.4	89.6	46.8	0.90	0.80	0.95	0.46	0.88	1.11
CS7	366.9	412.0	347.4	506.8	374.1	0.60	0.53	0.63	0.43	0.58	3.01
CS8	183.4	206.0	173.7	253.4	187.0	0.84	0.75	0.89	0.61	0.83	1.05

Regarding the **FS-NI** full scale non-injected specimens, Eq. (3.7) gives good simulations for low vertical stress levels at 0.5MPa and 0.75MPa. For higher vertical stress levels at 1.0MPa and 1.25MPa Eqs. (3.5) and (3.9) provide suited ratios with less than 5% divergence from the experimental results. Equation (3.6) provides results with around 50% divergent, while this percentage increase as the vertical stress levels increase. Eq. (3.8) is not able to simulate the experimental results. Full scale injected specimens **FS-I** had better ratios in general compared to non-injected ones. It is noted that Eq. (3.9) is suitable at all vertical stress levels with a divergence factor ranging between 2%-11%. Then, Eq. (3.5) provides a good match for vertical stress levels 1.0MPa, 1.25MPa and 1.5MPa, while Eqs. (3.6) and (3.7) show fair ratios for vertical stress level 1.0MPa and divergence factor increases as the vertical stress levels increase. Herein, Eq. (3.8) shows better match than previous samples.

Moving to the scaled non-injected specimens **S-NI**, hardly any formulation is able to capture the shear capacity at 0.5MPa vertical stress level with Eq. (3.8) having the closest result with a divergence of 28%. At 0.75MPa vertical stress level, Eq. (3.6) gives the best ratio of 0.92. Then, Eqs. (3.5) and (3.9) show good simulation of the experimental results at 1.0MPa vertical stress level with ratios 0.99 and 0.91 respectively, while Eq. (3.8) is not able to provide good simulation. For the scaled injected specimens **S-I**, Eq. (3.9) provides good match at all vertical stress levels and Eq. (3.5) shows good simulation at all vertical stress levels except for 2.0MPa, where the divergence reaches 24%. Further, Eqs. (3.6) and (3.7) gave fair results for 1.0MPa and 1.25MPa, while the divergence increases as the pre-stress levels increase. However, Eq. (3.8) shows high divergence in comparison to the experimental values.

It is important to note that the experimental campaign from which the **H** samples are selected is the one used for the calibration of Eq. (3.8); thus, it is expected to give good results in regard to

this portion. As deemed evident from the ratios in Table 3.7, all the formulations provide high divergence ratios except for Eq. (3.8) that gives fair results for samples **H1**, **H2** and **H3** and very good simulations for samples **H4**, **H5**, **H6** and **H7**. The experimental values selected for this work are based on the positive displacements of the piers during the in-plane cyclic tests which are clearly higher than the shear capacities in the negative displacements. Regarding the **P3** and **P4** samples, most of the formulations provided fair simulations with divergence around 25% except for Eq. (3.6) at 619kN gravity load and Eq. (3.8) at both loading levels.

Moreover, Eq. (3.6) provides very good simulation of the experimental results in all the samples from the ZAG Laboratory: **10-A**, **10-B**, **10-C** and **11-A**. Then, Eqs. (3.5), (3.7) and (3.9) gave good shear ratio indices for the samples **10-A** and **11-A**, while Eq. (3.8) gives fair results only for the **11-A** sample and high divergence for the other piers. On the other hand, the slender samples from the EUCENTRE Laboratory show good simulation of the experimental results. For samples **CL6**, **CS5** and **CS6**, Eqs. (3.5), (3.6), (3.7) and (3.9) show very good results, while for the squat samples **CS7** and **CS8** the divergence increase reaching up to 45%. Nonetheless, Eq. (3.8) was not able to provide good simulation for any sample.

Figure 3.2a is used to assess the influence of the vertical stress variation on the shear capacity simulation regarding full scale non-injected piers. It shows that Eqs. (3.5), (3.7) and (3.9) were able to simulate the experimental results well. On the other hand, Eq. (3.6) only gives fair results for low vertical stress levels and Eq. (3.8) gives much higher values than the experimental ones. The same pattern seems to repeat itself in Figs 3.2b, 3.2c and 3.2d with slight variation in the accuracy of the formulations. The scaling factor of the tested walls and the presence or the absence of the strengthening mortar through injection has no major effect on the functionality of the five equations under examination.

Figure 3.2e shows the influence of the vertical stress variation between sample H1 and H2 that has similar geometry on the accuracy of the formulations. Only Eq. (3.8) provides close results to the experimental ones, while the other four equations gave very low values. No evident improvement was noticed with the increase in the vertical stress level. In the same manner, Figs. 3.2f and 3.2g show the influence of the wall thicknesses and aspect ratios on the accuracy of the formulations. Thus, Eq. (3.8) provides the most accurate results in comparison to the experimental ones. As the thickness of the walls increases and the aspect ratios increases indicating more slenderness, the results became more precise.

Figure 3.3a shows the influence of vertical stress levels on the formulations using the samples **P3** and **P4**, characterized by a squat geometry and an effective height $H_o = 1.5h$. Using Eq. (3.7), reasonable results were obtained in comparison to the experimental ones. Then, Eqs. (3.5) and (3.9) show also reasonable results. There is a general tendency to have better simulations at lower pre-stress levels mostly evident when using Eq. (3.6).

The variation of vertical stress between samples **10-A** and **10-B** is also examined in Fig. 3.3b. Herein, Eq. (3.6) gave the best simulation of the experimental values with very high precision, while Eqs. (3.5), (3.7) and (3.9) give fair results with divergence at the high vertical stress level. The variation of the typology between samples **10-B** that is fully mortared and **10-C** where the mortar is only applied to the bed joints is presented in Fig. 3.3c. As depicted, Eq. (3.6) keeps its good record of simulation in those samples followed by Eqs. (3.5), (3.7) and (3.9). No apparent improvement in the results is realized due to the change in typology. The last set of tested piers is utilized in several setups to account for different parameters that are analyzed for their influence on the accuracy of the formulations. Figure 3.3d presents the pre-stress variation in samples **CL6** and **CS5**.

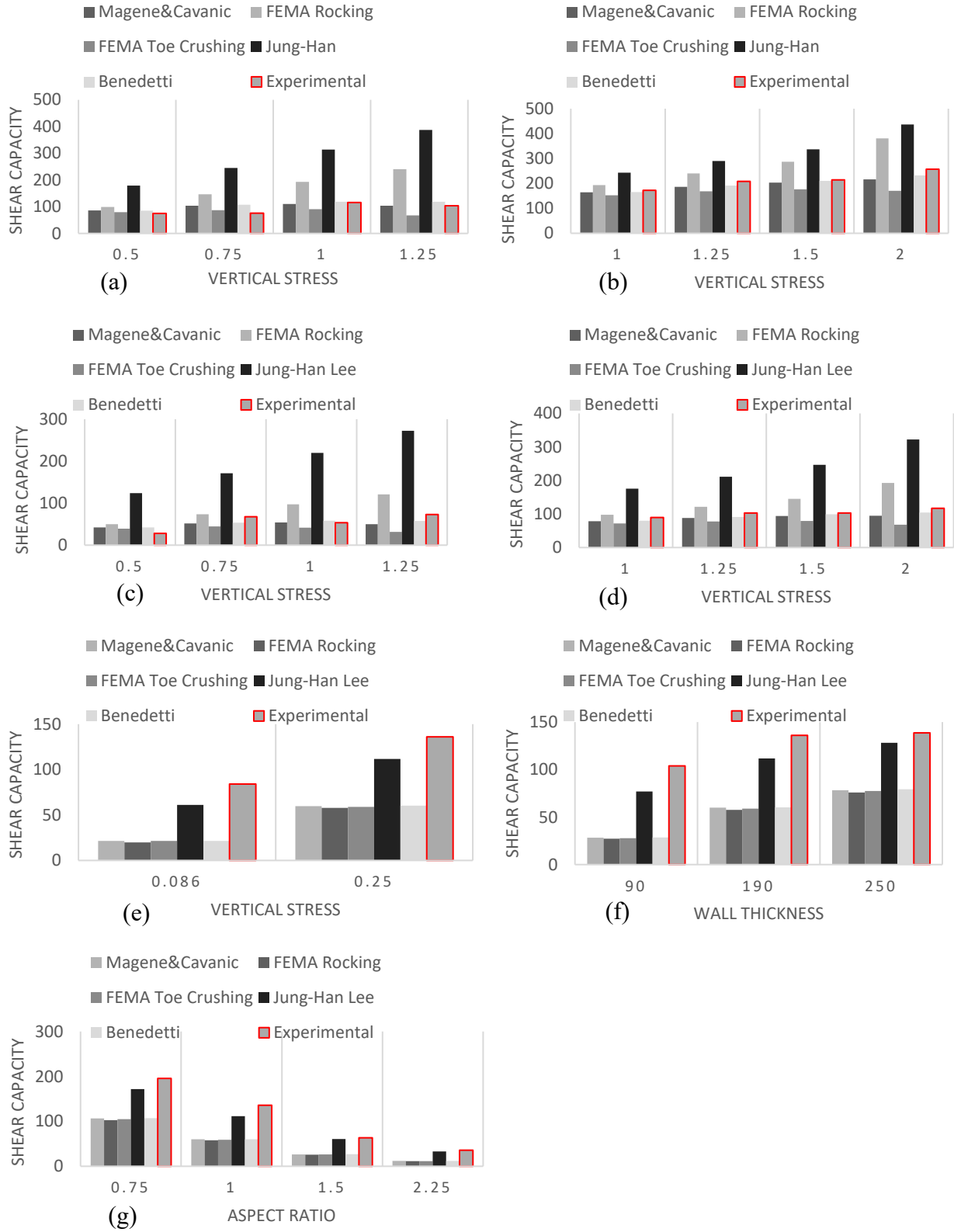


Figure 3.2: a) The variation of shear capacities with the vertical stress levels for samples FS-NI b) FS-I c) S-NI d) S-I e) H1 and H2 f) H2, H3 and H4 g) H2, H5, H6 and H7.

From this figure, it is shown that Eq. (3.6) can capture the slope of the graph where it starts with fair simulation at low vertical stress level and diverges at the higher vertical stress level, while Eqs. (3.5) and (3.9) give better results at higher vertical stress level. It is noted that Eq. (3.8) is not included in the graphical representation due to its high divergence. Figure 3.3e shows the effect of the boundary conditions on the slender specimens **CS5** and **CS6**. All the formulations present good correlation with the experimental results with no evident improvement with the variation in the boundary conditions from doubly fixed to cantilever except for Eq. (3.7). Again, Eq. (3.8) was excluded from the graph due to its high divergence. On the other hand, the squat samples **CS7** and **CS8** in Fig. 3.3f shows great improvement in the results of the formulations for cantilever boundary condition when compared to the doubly fixed condition. The divergence is reduced immensely with best performance for Eq. (3.7). Then, in Fig. 3.3g, samples **CS5** and **CS7** with doubly fixed boundary conditions and different aspect ratios are analyzed. Apart from Eq. (3.8), all formulations show good correlation at the higher aspect ratio of 2 indicating a slender geometry and more divergence with lower aspect ratio of 1 referring to squat geometry. A very similar pattern is realized in Fig. 3.3h for samples **CS6** and **CS8** except for less divergence happening at the low aspect ratio of 1.

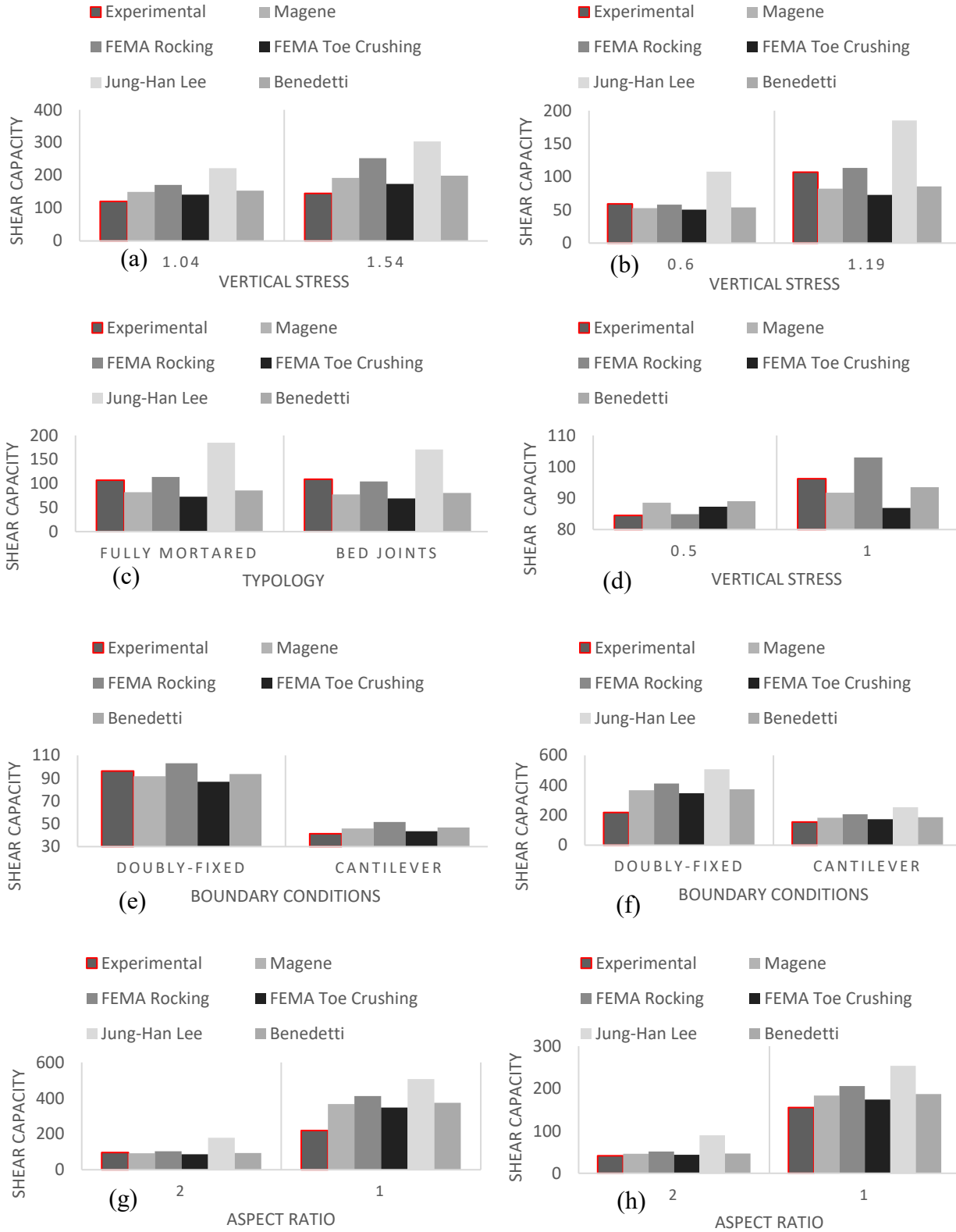


Figure 3.3: a) Shear capacities versus the vertical stresses in samples P3 and P4 b) 10-A and 10-B c) 10-B & 10-C d) CL6 and CS5 e) CS5 and CS6 f) CS7 and CS8 g) CS5 and CS7 h) CS6 & CS8.

Table 3.8: Variation of capacity shear indices and divergence factors in terms of the different parameters of the piers

ID	h/L _w ¹	BC ⁵	VS ³	TP ²⁵	WT ¹⁵	SC ⁴	CS ⁶	UST ⁷	MT ⁸	TR ²	V _u /V _{u5}	V _u /V _{u6}	V _u /V _{u7}	V _u /V _{u8}	V _u /V _{u9}
	(1)	(2)	(3)	(4)	(5)	(6)	(7)	(8)	(9)	(10)	(11.1)	(11.2)	(11.3)	(11.4)	(11.5)
	Primary					Secondary					Indices				
FS-NI	1.2	C ¹⁶	0.50	FM ²⁶	500	FS ¹³	TL ²⁷	CS ²¹	W ²³	IR ¹⁰	0.87	0.75	0.94	0.42	0.88
FS-NI	1.2	C	0.75	FM	500	FS	TL	CS	W	IR	0.73	0.52	0.88	0.31	0.71
FS-NI	1.2	C	1.00	FM	500	FS	TL	CS	W	IR	1.05	0.60	1.28	0.37	0.98
FS-NI	1.2	C	1.25	FM	500	FS	TL	CS	W	IR	1.00	0.43	1.53	0.27	0.88
DF ⁹											0.11	0.43	0.25	0.66	0.14
FS-I	1.2	C	1.00	FM	500	FS	TL	CS	M ²⁴	IR	1.05	0.89	1.13	0.71	1.04
FS-I	1.2	C	1.25	FM	500	FS	TL	CS	M	IR	1.11	0.87	1.24	0.72	1.09
FS-I	1.2	C	1.50	FM	500	FS	TL	CS	M	IR	1.06	0.75	1.21	0.64	1.02
FS-I	1.2	C	2.00	FM	500	FS	TL	CS	M	IR	1.19	0.68	1.51	0.59	1.11
DF											0.10	0.20	0.27	0.34	0.07
S-NI	1.25	C	0.50	FM	330	S ¹⁴	TL	CS	W	IR	0.66	0.56	0.72	0.23	0.66
S-NI	1.25	C	0.75	FM	330	S	TL	CS	W	IR	1.32	0.92	1.53	0.40	1.28
S-NI	1.25	C	1.00	FM	330	S	TL	CS	W	IR	0.99	0.55	1.27	0.24	0.91
S-NI	1.25	C	1.25	FM	330	S	TL	CS	W	IR	1.46	0.61	2.33	0.27	1.28
DF											0.28	0.34	0.60	0.72	0.25
S-I	1.25	C	1.00	FM	330	S	TL	CS	M	IR	1.13	0.92	1.24	0.51	1.11
S-I	1.25	C	1.25	FM	330	S	TL	CS	M	IR	1.16	0.85	1.32	0.49	1.13
S-I	1.25	C	1.50	FM	330	S	TL	CS	M	IR	1.09	0.71	1.30	0.42	1.04
S-I	1.25	C	2.00	FM	330	S	TL	CS	M	IR	1.24	0.61	1.71	0.36	1.13
DF											0.16	0.23	0.39	0.56	0.10
H1	1	C	0.086*	FM	190	FS	SL ¹⁹	CB ²⁰	M	SW	3.90	4.24	3.92	1.38	3.90
H2	1	C	0.250*	FM	190	FS	SL	CB	M	SW	2.27	2.36	2.31	1.22	2.26
H3	1	C	0.250*	FM	90	FS	HL ²⁸	CB	M	SW	3.66	3.79	3.72	1.35	3.64
H4	1	C	0.250*	FM	250	FS	DL	CB	M	SW	1.77	1.82	1.79	1.08	1.75
H5	2.5	C	0.250*	FM	190	FS	SL	CB	M	SW	3.04	3.15	3.08	1.08	3.02
H6	1.5	C	0.250*	FM	190	FS	SL	CB	M	SW	2.39	2.47	2.42	1.04	2.37
H7	0.75	C	0.250*	FM	190	FS	SL	CB	M	SW	1.84	1.91	1.87	1.14	1.83
DF											1.70	1.82	1.73	0.18	1.68
P3	1.12	C	1.04	FM	200	FS	SL	CB	M	SW	0.81	0.71	0.86	0.54	0.79
P4	1.12	C	1.54	FM	200	FS	SL	CB	M	SW	0.75	0.58	0.83	0.48	0.73
DF											0.22	0.36	0.16	0.49	0.24
10-A	1.47	C	0.60	FM	300	FS	SL	CB	M	SW	1.12	1.02	1.17	0.55	1.10
10-B	1.47	C	1.19	FM	300	FS	SL	CB	M	SW	1.30	0.94	1.47	0.58	1.25
10-C	1.53	C	1.19	BM ²²	300	FS	SL	CB	M	SW	1.41	1.04	1.58	0.64	1.35
DF											0.28	0.04	0.41	0.41	0.23
11-A	0.68	C	0.59	FM	297	FS	SL	CB	M	SW	1.02	0.95	1.08	0.81	1.01
CL6	2.08	FF	0.50	FM	300	FS	SL	CB	M	SW	0.95	0.99	0.97	0.64	0.95
CS5	2	FF	1.00	FM	175	FS	SL	CM ¹²	M	SW	1.05	0.93	1.11	0.54	1.03
CS6	2	C	1.00	BM	175	FS	SL	CM	M	SW	0.90	0.80	0.95	0.46	0.88
CS7	1	FF	1.00	BM	175	FS	SL	CM	M	SW	0.60	0.53	0.63	0.43	0.58
CS8	1	C	1.00	BM	175	FS	SL	CM	M	SW	0.84	0.75	0.89	0.61	0.83
DF											0.18	0.25	0.16	0.49	0.19

1 Aspect ratios define as height divided by the width
2 Texture of the unit stones used in the piers
3 Vertical Stress excluding the own weight
4 Scale of the pier specimen
5 Boundary conditions
6 Cross section of the wall
7 Unit stone material type depending on the origin
8 Mortar type depending on its strength
9 Divergence factor = $\sum_{i=1}^n |V_i/V_{u,i} - 1|/n$
10 Irregular texture referring to unit stones partially worked
11 Sawn texture referring to unit stones fully worked
12 Calcium silicate masonry
13 Full scale specimen based on a typical stone masonry construction
14 Scaled specimen based on a typical stone masonry construction

15 Wall thickness regardless of the number of wythes
16 Cantilever or fixed-free boundary conditions
17 Fixed-fixed boundary conditions
18 Double-leaf cross section wall
19 Single-leaf cross section wall
20 Clay brick masonry
21 Calcareous stone: red, regular white, irregular white
22 Only bed joints mortared
23 Weak mortar with $f_m < 5\text{MPa}$
24 Medium strength mortar with $5\text{MPa} < f_m < 15\text{MPa}$
25 Typology regarding the placement of mortar
26 Fully mortared including bed and head joints
27 Three-leaf cross section wall
28 Half-leaf cross section wall

To understand the effect of different parameters on the formulations, major and minor sets are defined based on data available in Table 3.8 in the same way done for shear analysis in the previous section.

Starting with Eqs. (3.5) and (3.9), the major sample set **FS-NI** shows that the formulations perform better for higher vertical stress levels at 1.0MPa and 1.25 MPa. Considering the major set **FS-I**, Eqs. (3.5) and (3.9) give good results for vertical stress levels 1.0MPa, 1.25MPa and 1.5MPa, while their accuracy declines for 2.0MPa. The major sample set **S-NI** indicates a good performance at 1.0MPa while the major set **S-I** shows good ratios at 1.0MPa, 1.25MPa and 1.5MPa. Despite the scaling and the injection factors, Eqs. (3.5) and (3.9) perform well for a range of 1.0 MPa and 1.25MPa. The major sample sets **FS-NI-1 & FS-I-1**; **FS-NI-1.25 & FS-I-1.25**; **S-NI-1 & S-I-1**; **S-NI-1.25 & S-I-1.25** can hardly indicate any improvement in the results due to injection. Regarding the minor sets **FS-NI & S-NI** and **FS-I & S-I** with close aspect ratios, they show a better performance for the full-scale specimens at all the vertical stress levels. This result is clarified by the smaller divergence factors $DF = 0.11$ and $DF = 0.10$ for the full-scale piers. The major set **H1- H2** shows better performance for Eqs. (3.5) and (3.9) at higher vertical stress level 0.25MPa, while the major set **H2, H3, H4** indicates better results as increasing thickness of the wall. Moreover, the major set **H2, H5, H6** and **H7** shows that the ratios are enhanced as the aspect ratio decreases thus moving into a squatter shaped pier. The divergence factor for the **H** series is very high indicating weak performance with this series which could be justified by the general low vertical stress levels. Considering the major set **P3** and **P4**, the formulation acts better with vertical stress level around 1.0 MPa as proven earlier. Then, the major set 10-A and 10-B shows that the ratios are closer to 1 for lower vertical stress level 0.6MPa than that of 1.19MPa, while the major set **10-B** and **10-C** indicates better performance for fully mortared specimen with only 10% and

11%, respectively, difference in the results. The last set piers indicates that Eqs. (3.5) and (3.9) perform better with a cantilever boundary condition as inferred from major set **CS7** and **CS8** despite the similar results that are illustrated by the minor set **CS5** and **CS6**. Taking into consideration the major set **CS6** and **CS8** and the minor set **CS5** and **CS7**, it clearly indicates an advantage for the higher aspect ratio of 2. The divergence factor for this set $DF = 0.18$ and 0.19 , respectively, indicates a fair representation of the equations for the experimental values.

Analyzing Eq. (3.6) it is evident from the first three major sets **FS-NI**; **FS-I**; **S-I** that the performance of the formulation declines with the increase in pre-stress levels. Major sets **FS-NI-1** and **FS-I-1**, as well as **FS-NI-1.25** and **FS-I-1.25** indicates clearly that the injected specimens outperform the non-injected ones. The same conclusion can be made from the scaled major sets **S-NI-1** and **S-I-1**, as well as, **S-NI-1.25** and **S-I-1.25**. Those results are illustrated in the lower divergence factors for both injected samples. Regarding the major sets **FS-NI** and **S-NI**, as well as **FS-I** and **S-I** there is no clear indication for the influence of scaling on the performance of the formulation. The major set **H1**, **H2** indicates better performance for higher pre-stress level at 0.25MPa , while the major set **H2**, **H3**, **H4** shows improvement in the results with the increase in the thicknesses of the walls. The major set **H2**, **H5**, **H6**, **H7** indicates an increase in the divergence as the aspect ratio of the piers increases or become slenderer. The divergence factor of the **H** series is $DF = 1.82$ which is very high; thus making Eq. (3.6) less representative of such samples. The major set **P3** and **P4** shows that the formulation had a better ratio with lower pre-stress level. Hence, the major set **10-A** and **10-B** shows good results for both vertical stress levels of 0.6MPa and 1.19MPa , respectively, while the major set **10-B** and **10-C** also provides good values for both typologies of mortar application. No clear advantage can be withdrawn from those mentioned sets; however, it is obvious that Eq. (3.6) works well with this kind of samples that are characterized by

an average aspect ratio of 1.5 and cantilever boundary conditions represented in the very low divergence factor $DF = 0.04$. In the last set of piers, the minor set **CS5** and **CS6** shows that the simulation acts better for doubly fixed boundary conditions regarding the slender piers while the major set **CS7** and **CS8** shows that the cantilever boundary condition has better advantage for squat piers. Regarding the major sets **CS5**, **CS7**, as well as **CS6**, **CS8**, the slender piers with aspect ratio of 2 has better results.

Evaluating Eq. (3.7) using the major sets **FS-NI**; **FS-I**; **S-I**, is shown that the simulation becomes more divergent with the increase of vertical stress level going through a plateau at the mid-levels of pre-stresses at 1.25MPa and 1.5MPa for the injected specimens. The major sets **FS-NI-1** and **FS-I-1**; **FS-NI-1.25** and **FS-I-1.25**; **S-NI-1** and **S-I-1**; **S-NI-1.25** and **S-I-1.25** indicate better performance of the injected piers for both full scaled and scaled samples. As for the major sets **FS-NI** & **S-NI** and **FS-I** & **S-I** it is noticed that the full-scale specimens have better simulation to the experimental results which is illustrated by the higher divergence factors for the scaled piers. The sets from the **H** series behaves similarly to the previous formulations with $DF = 1.73$ making the representation not very reliable. The major set **P3**, **P4** and the sets from samples **10-A**, **10-B** and **10-C** has similar simulation as Eq. (3.5). However, the $DF = 0.41$ is more divergent than the previous results. The major sets **CS7**, **CS8** and **CS5**, **CS6** shows that the formulations act better with cantilever boundary conditions for both slender and squat piers. Slender piers with aspect ratio of 2 has clear advantage as demonstrated in the previous formulations.

Equation (3.8) only performs well with the experimental campaign **H** series that is used for its calibration the first place. This can indicate that this formulation provides good results for low pre-stress levels that are used in those tests. The major set **H1**, **H2** shows better performance for Eq. (3.8) at higher pre-stress level 0.25MPa, while the major set **H2**, **H3**, **H4** indicates better results as

increasing thickness of the wall. Meanwhile, the major set **H2, H5, H6, H7** gives very good correlations with aspect ratios of 1.5 and 2.5 and fair results for the aspect ratio 0.75. The divergence factor for this set $DF = 0.18$ is a clear indication for the advantage of this formulation. Comparing the equation to the rest of the major sets it performs in a very similar manner to the previous formulations about **FS-NI; FS-I; S-NI; S-I; P3; P4**. Regarding the samples **10-A, 10-B** and **10-C** the values are very close thus showing no clear advantage for any pre-stress level or typology. The major set **CS5, CS6** shows a better performance for doubly fixed boundary condition in slender piers, while the major set **CS7, CS8** indicates an advantage for the cantilever boundary condition in squat piers.

3.3 Shear and Flexural dominant behavior in Spandrels Elements

Spandrels are considered as secondary elements in URM walls; however, they significantly contribute to the overall seismic response. Through the connective joints, spandrels form a coupling effect on the adjacent piers determining their boundary conditions and the stress distribution along their spans (Foraboschi, 2009). In many codes, simplified equivalent frame models are allowed to utilize the “weak spandrel - strong piers” approach which ignores the spandrels; thus considering the piers as cantilevers and “strong spandrels - weak piers” approach which models the spandrel as a rigid element; thus considering the piers as fixed-fixed elements (Cattari & Lagomarsino, 2008). The two approaches do not fully represent the actual behavior of spandrels that can experience a variation of strength and ductility throughout the ground motion application. Therefore, modeling the strength capacities and the displacements of masonry spandrels is essential for the overall results of the wall, as the stiffness degradation in the spandrels is reflected on the coupling of the piers.

The typical mechanisms in spandrels observed in post-earthquake surveys are the flexural and shear failures. Shear failure shown in Fig. 3.4b is more common in squat geometries and laterally strengthened spandrels. It is characterized with more strength that continue to build up until failure within the range of the ultimate displacement. This means that more energy dissipation is associated with the hysteretic cyclic loop representing the motion during lateral shaking. Cracks propagation has the cross-X shape, passing through bed and head joints at the interface between masonry units and mortar (Beyer, 2012). Flexure on the other hand shown in Fig. 3.4a is common in slender geometries and spandrels with less or no lateral support. The strength endures a sudden drop at a very small displacement before it settles to the residual strength that can withstand most of the displacement in the spandrel until failure. Less energy dissipation is allied with this behavior due to the small hysteretic cyclic loops in the force-displacement graphs. Cracks form perpendicular to the span of the spandrel right at the corners of the opening passing through the head joints (Beyer, 2012). Hybrid cracking failure can also take place in spandrels as the formation of weak points can alter the behavior of the element.

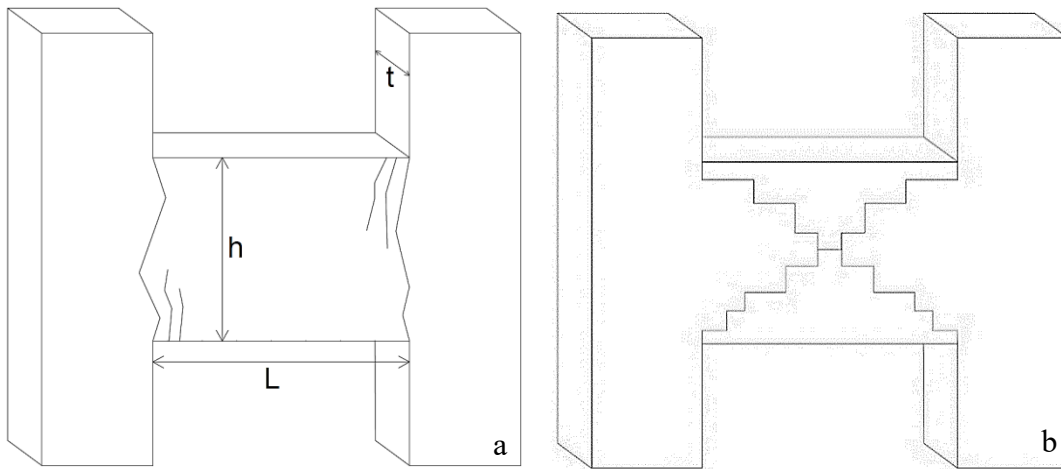


Figure 3.4: a) Flexural cracks in a spandrel and b) Shear cracks in a spandrel

Equivalent frame modeling represented in Fig. 3.5b has proven to be a useful modeling technique that can simplify the complexity of masonry structures through reducing the number of degrees of freedom and allowing for more sophisticated analysis such as the time-history to take place (Tomazevic, 1978) and (Magenes & Della Fontana, 1998). With proper calibration of the strength formulations in the hinges, sophisticated results can be delivered. Proper positioning of the flexural and shear hinges is also required as part of the model. Shear hinges are placed in the middle of the spandrel as to account for the formation of cracks at the center of element, as for the flexural hinges they are placed next to the support at the end of the rigid node following the formation of cracks at that particular zone (Pasticier et al., 2008). The moment and shear distributions along the spandrels are illustrated in Fig. 3.5a. Zero moment is assigned in the middle of the element following the assumption that the spandrel is subjected to double bending.

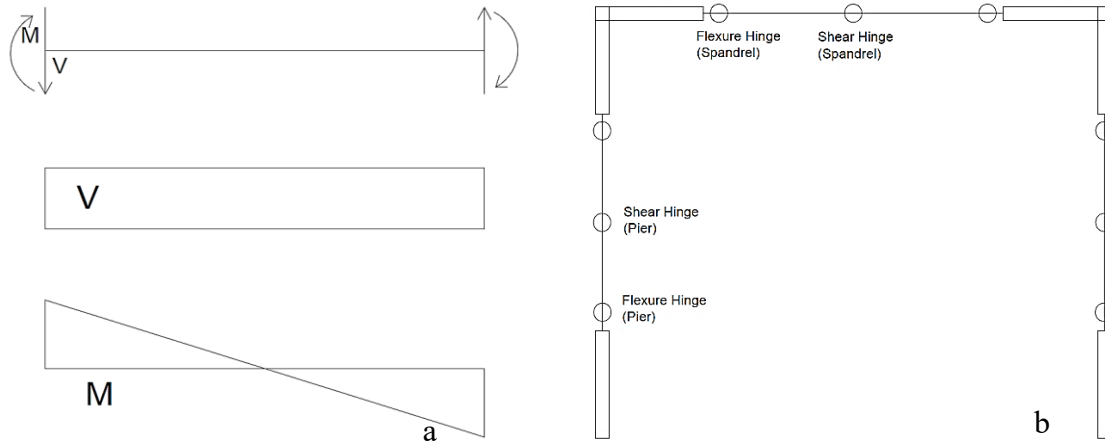


Figure 3.5: a) Shear and moment diagrams following the force distribution in spandrels b) Distribution of plastic hinges in an equivalent frame model.

3.3.1 Parameters for Masonry Spandrels

The behavior of spandrels is influenced by the various parameters that characterize the spandrels. Mentioned in the previous sections are some parameters that determine the type of failure. However, within each category, several strength formulations are proposed throughout the literature that determine the capacity of those structural elements. The accuracy of those criterion is dependent on major parameters used in designing spandrels (Beyer & Mangalathu, 2013). The construction type of spandrels for typical practices such as using wooden lintels or masonry arches can influence the lateral behavior. Also using thick versus thin timber lintels can alter the stiffness of the element and thus the simulation results. The presence of tie rods or other lateral restricting elements can determine the magnitude of horizontal compression forces on the spandrel. Those forces have significant implications on the type of response and developed strength within the element itself.

We can also identify minor parameters that has indirect effect on the behavior of the spandrels. They are used to justify the variations in the results that might arise between the numerical and experimental calculations. Such parameters can include the texture of the unit masonry stones,

their arrangement and material type, the thickness of the wall and the number of layers, and the type of mortar used in the construction. Also, the aspect ratio of the spandrel and the scaling factors should be considered in the assessment.

An important thing to consider in the analysis is the boundary conditions that is linked to the stress distributions for shear and flexural behaviors. Since spandrels act as the connection between piers this can also affect their response as well in which reflects on the interaction between those two members and the coupling effect induced. This will be considered in the full-scale model of an entire masonry wall. Instead of simplifying the model to the ones proposed by the codes mentioned earlier, it would be more satisfactory to include three cases that covers the proper connection at the peak strength of the spandrel, the weak connection at the residual strength of the spandrel and the finally the lost connection at the failure of the spandrel. Thus, the piers will have fixed-fixed, intermediate and cantilever boundaries, respectively.

3.3.2 Capacity Equations for Shear Dominant Failure

The Italian codes (OPCM 3431, 2005) suggests the following shear criterion for the peak strength of the spandrel.

$$V_{u,1} = h \cdot t \cdot f_{vo} \quad (3.11)$$

Herein, t is the spandrel thickness, h is the height of the spandrel and f_{vo} is the shear strength of wall assemblages without considering any compression thus relying mainly on the cohesive strength of the mortar c .

Turnsek and Cacovic (Turnšek & Čačovič, 1971) suggested another formulation that accounts for the maximum tensile strength at the middle of the spandrel. The equation is borrowed from the shear strength of piers with some modifications in the parameters.

$$V_{u,2} = f_v \cdot h \cdot t \cdot \beta \sqrt{1 + \frac{\sigma_s}{f_v}} \quad (3.12)$$

Herein, f_v is the diagonal tensile strength; σ_s is the axial compressive stress; β is the aspect ratio (height/length= h/l) where $0.67 \leq \beta \leq 1.0$.

Magenes and Della Fontana (Magenes & Della Fontana, 1998) suggested the follow criterion which influenced the one provided by the Italian codes OPCM 3431. A modification of the cohesion parameter, as suggested by (Mann & Müller, 1982) is used in the calculations.

$$V_{u,3} = h \cdot t \cdot c_r \quad (3.13)$$

where $c_r = c \cdot \frac{1}{1+2(h_b+h_j)/(l_b+l_j)}$ is the reduced cohesion stress; h_b and h_j is are the height of the brick and the joint respectively; l_b and l_j are the length of the brick and the joint, respectively.

3.3.3 Capacity Equations for Flexure Dominant Failure

Adopted by the Italian codes OPCM 3431, the maximum shear force in a flexural governed behavior is captured by the following formulation.

$$V_{u,4} = P \cdot \frac{h}{l} \cdot \left[1 - \frac{P}{0.85 f_m h t} \right] \quad (3.14)$$

where f_m is the compressive strength of the masonry; P is the axial force applied on the spandrel from external load. If P was unknown it can be replaced by the minimum of $[f_{ie} ; 0.4 h t f_m]$, where f_{ie} is the tensile strength of the horizontal tension elements such as steel ties and ring beams.

FEMA 306 (FEMA 306, 1998) adopts the following equation for the flexural behavior of masonry spandrels that ignores the axial force.

$$V_{u,5} = \frac{2}{l} \cdot \frac{2}{3} h \cdot f_{p,tot} \cdot \frac{h}{4(h_j+h_b)} \quad (3.15)$$

where the total tensile force $f_{p,tot} = f_{t,b}x t_b x \frac{l_b}{2} + f_{t,s}x h_b x \frac{l_b}{2} x (NB - 1)$. The tensile strength due to friction in the bed-joints is $f_{t,b} = 0.5(0.75c + \gamma_{sp}\sigma_p)$ and the tensile strength due to cohesion on the side faces of the bricks is $f_{t,s} = 0.5(0.75c)$. Herein, γ_{sp} is a ratio to determine the effective vertical stress on adjacent piers suggested as 0.5, σ_p is the vertical stress on the adjacent pier, NB is the number of wythes and t_b is the thickness of the brick.

Cattari and Lagomarsino (Cattari & Lagomarsino, 2008) used the following equation that includes the tensile criterion at the level of the brick units.

$$V_{u,6} = \frac{2}{l} \cdot t \left[0.85 \cdot f_m \cdot h_c \left(\frac{h}{2} - \frac{h_c}{2} \right) + f_{tu} (h - h_c) \frac{h_c}{2} \right] \quad (3.16)$$

where $f_{tu} = \min \left(\mu \cdot \gamma_{sp} \sigma_p \cdot \frac{l_b}{2(h_j + h_b)}; \frac{f_{bt}}{2} \right)$ is the equivalent tensile strength in the mortar joints and the brick; f_{bt} is the limited tensile strength of the brick; γ_{sp} is suggested as 0.65; μ is the friction coefficient; $h_c = \frac{\sigma_s + f_{tu}}{0.85f_m + f_{tu}} \cdot h$ is the depth of compressive zone.

Betti et al. (Betti et al., 2008) also provides an equation for ultimate flexural strength in spandrels. It varies the parameters between large axial forces and small axial forces on the element shown below.

$$V_{u,7} = \frac{2}{l} \cdot \frac{h^2 t}{6} \cdot (k f_{tm} + \sigma_s) \quad (3.17)$$

where $f_{tm} = c/2\mu$ is the tensile strength of mortar joints.

3.3.4 Parametric Analysis of the Shear Failure Mode

In the aim of verifying the accuracy of each formulation about certain parameters, different experimental campaigns conducted on spandrels are selected to compare the numerical results to the experimental ones. A study held in Pavia, Italy, focuses on two different aspects in the

construction of the spandrel using full scale specimens. The samples have boundary conditions resembling the real case scenario of a spandrel in a wall built using a double-leaf Credaro stones. The preliminary characterization of the elements are represented in Table 3.9 (Magenes, Penna, Galasco, & Rota, 2010). Lime mortar with weak strength is used to fill the head and bed joints.

Table 3.9: Preliminary characterizations of the spandrels used in the full-scale experiment.

Parameters	f_m	f_v	f_t	E	G	Density
Mean Values [MPa]	3.28	0.197	0.137	2550	840	2680 kg/m ³

In the first experiment (Graziotti et al., 2012), the parameter tested is the presence and absence of lateral support. Two samples are built with dimensions $l \times h \times t$ (length; height; thickness) = 1200x1080x320mm with a thick lintel with height of 120mm using two wythes. The first sample named **W1** has no lateral support while the other sample **W2** has a lateral support exerting an axial force $F=38\text{KN}$. The second experiment (Graziotti et al., 2014), aiming to test the variation in the size of the lintels used to support the masonry units at the bottom of the structural element, while considering an initial axial force of 28kN. The spandrels have dimensions $l \times h \times t = 1200 \times 780 \times 320\text{mm}$. The first sample of 2nd experiment considered, **W3**, has a thick wooden lintel with 120mm depth, while the second sample **W4** has a thin wooden lintel with depth of 25mm. The type of failure associated with each parameter the maximum and residual strength obtained are summarized in Table 3.10. It must be noted that there was a problem with the actuator while testing **W4** that might alter the results. Herein, V_u represent the maximum shear force reached by the spandrel. Specimen **W1** exhibit a flexural failure mode and thus would be excluded from this analysis.

Table 3.10: Experimental results from the in-plane cyclic tests on the piers

Specimens	V_u [kN]	Failure Mode
W2	60	Diagonal Shear
W3	38	Diagonal Shear
W4	23	Hybrid

The values of the cohesion strength c and the friction coefficient μ_s are chosen to be 0.35 MPa and 0.65 respectively, based on (Elmenschawi & Shrive, 2015). The irregular stones have a length of 200-350mm and height of 100-150mm with mortar joints thickness ranging between 20-30mm. Average values are used. The height of the wooden lintel is not considered in the calculation of the spandrel's height. The results of maximum shear forces estimated by the simplified equations are provided in Table 3.11.

Table 3.11: Results of maximum shear from the simplified formulations

Specimens	V _{u,1} from Eq. (3.11)	V _{u,2} from Eq. (3.12)	V _{u,3} from Eq. (3.13)
	[kN]	[kN]	[kN]
W2	120.9	61.3	60.5
W3	87.4	32.0	43.7
W4	87.4	32.0	43.7

In another study, (Knox et al., 2017) tested six URM brick masonry frames for in-plane cyclic behavior. Full scale specimens are constructed using 80 years old bricks with typical dimensions of 225x108x75mm for length, width, and height respectively and weak lime mortar of 2.9MPa compressive strength and 10mm thickness of mortar joints. The mechanical properties of the panel are mentioned in Table 3.12.

Table 3.12: Mechanical properties of the masonry panels

Parameters	f _v	f _t	μ	c
Mean Values [MPa]	0.262	0.185	0.7	0.3

Different dimensions $l \times h \times t$ of the spandrels summarized in Table 3.13 are varied between the samples with some variations in the axial stresses on the piers holding the spandrels along with the experimental shear forces and the failure modes. Sample **S3** and **S5** has same dimensions but the axial stresses on the adjacent piers are higher in **S3**. The mechanical properties of the materials are listed in Table 3.12. Zero axial forces are applied on the spandrels. It should be noted that the height of the piers in specimen **S6** is less than the rest of the samples.

Table 3.13: Experimental results from the in-plane cyclic tests on the piers

Specimens	Dimensions [mm]	V_u [kN]	Failure Mode
S1	1240x590x230	83.6	Diagonal Shear
S2	1740x590x230	49.3	Diagonal Shear
S3	1240x940x230	83.2	Diagonal Shear
S4	1240x1260x230	89.7	Diagonal Shear
S5	1240x940x230	48.6	Diagonal Shear
S6	1240x1450x230	24.9	Diagonal Shear

Applying the parameters to the simplified equations, different estimations of the maximum shear forces are extracted and summarized in Table 3.14.

Table 3.14: Results of maximum shear from the simplified formulations

Specimens	$V_{u,1}$ from Eq. (3.11)	$V_{u,2}$ from Eq. (3.12)	$V_{u,3}$ from Eq. (3.13)
	[kN]	[kN]	[kN]
S1	40.7	16.8	23.6
S2	40.7	12.0	23.6
S3	64.9	42.6	37.6
S4	86.9	76.6	50.4
S5	64.9	42.6	37.6
S6	100.1	101.4	58.1

To compare the experimental and numerical results of maximum shear forces attained by the spandrels, the ratios of experimental to numerical forces are displayed in Table 3.15 for all the previous samples considered in this study. The values of experimental to computed shear ratios closer to 1 shows good correlations.

Table 3.15: Ratio of experimental to the numerical shear capacity values

Specimens	$V_u/V_{u,1}$	$V_u/V_{u,2}$	$V_u/V_{u,3}$
W2	0.50	0.98	0.99
W3	0.43	1.19	0.87
W4	0.26	0.72	0.53
S1	2.05	4.98	3.54
S2	1.21	4.11	2.09
S3	1.28	1.95	2.21
S4	1.03	1.17	1.78
S5	0.75	1.14	1.29
S6	0.25	0.25	0.43

It is evident from the shear ratios that Eqs. (3.12) and (3.13) can simulate the experimental results to a very good extent while Eq. (3.11) overestimates the forces by almost double the values. Figure 3.6a shows that the equations better represent the values at lower axial forces. The shear forces in Fig. 3.6b are similar in both thick and thin lintels which indicates the deficiency of the formulations in considering such a variable in the calculations.

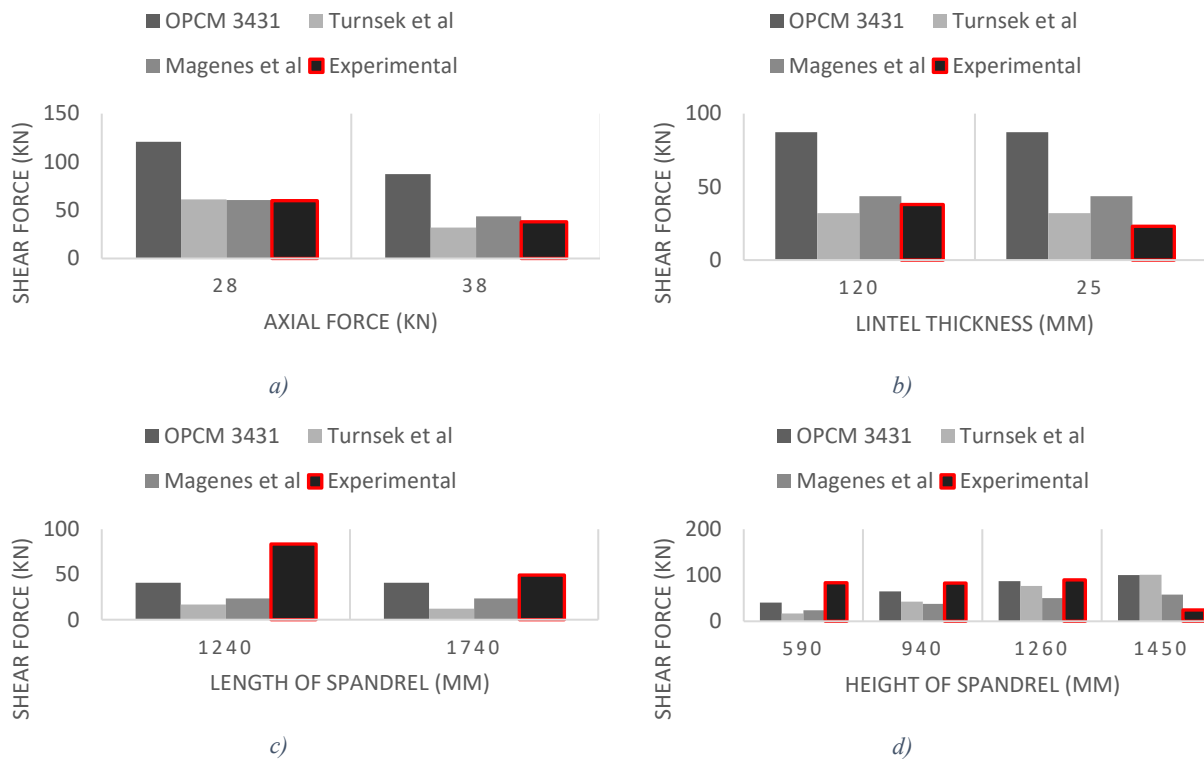


Figure 3.6: a) Variation of shear force w.r.t. axial force in spandrels W2 & W3 b) thickness of lintels in spandrels W3 & W4 c) length of spandrels S1 & S2 d) height of spandrels S1, S3, S4 & S6.

Observing the shear ratios for the second campaign, a significant divergence in the results is recognized for most of the samples. Equation (3.11) gives good correlation for specimen S4 while Eq. (3.12) gives fair correlation to specimen S5 with 14% divergence. In Fig. 3.6c, Eqs. (3.11) and (3.13) provide the same shear force values at both lengths of the spandrels indicating a deficiency in including this variable. In general, the results are better simulated for higher length of the spandrels. Observing Fig. 3.6d, the equations are yielding better results with the increase in the

height of the spandrels apart from the last value at 1450mm which experiences a sudden drop in the experimental shear forces that can be justified by the variations in the pier length used in that sample. In general Eq. (3.11) had better results than the other equations. It should be noted that the variation in the vertical stresses on the adjacent piers represented in samples **S3** and **S5** cannot be captured by the suggested equations in the literature.

3.3.5 Parametric Analysis of the Flexural Failure Mode

Three specimens from three different experimental campaigns with flexural failure are selected to conduct the comparisons. Due to the scarcity of data related to flexural behavior in spandrels the parameters are chosen roughly for the most convenient representation. Sample **W1** from the previous section will be used (Graziotti et al., 2012). Another sample, **M1** is utilized constructed using a thick lintel of 120mm height and no axial forces. It is constructed using brick masonry with dimensions 250x120x55mm. Finally, a third sample **T1** is selected (Beyer & Dazio, 2012); the sample was constructed using a thick lintel of 140mm height and brick masonry with typical dimensions of 250x120x60mm. A variable axial force is applied on the spandrel depending on the horizontal elongation starting with 5 kN as initial force and reaching 67 kN at the final failure with maximum crack. All the dimensions of the specimens and the experimental shear capacities are listed in Table 3.16.

Table 3.16: Data from the in-plane cyclic tests on the piers

Specimens	Dimensions [mm]	V_u [kN]	Failure Mode
W1	1200x1080x320	32	Flexural Failure
M1	1000x1080x380	70	Flexural Failure
T1	1180x1120x380	82	Flexural Failure

The mechanical properties of all three samples are summarized in Table 3.17. The data needed to apply the formulations are inferred from the same experimental campaigns, where the specimens

are tested or from similar samples from other sources when the data is missing (Brignola et al., 2008).

Table 3.17: Mechanical parameters for the selected samples

Samples	f_m [MPa]	μ	c [MPa]	NB	f_{bt} [MPa]	h_j [mm]	σ_p [MPa]	σ_s [MPa]
W1	3.28	0.65	0.35	2	19	25	0.17	0
M1	4	0.85	0.35	3	7	10	0.5	0
T1	4	0.85	0.35	2	7	10	0.33	0.16

The parameters are defined previously along with the formulations. In the same manner, for shear capacity analysis, the numerical capacity values associated with flexural failure are viewed in Table 3.18.

Table 3.18: Numerical capacity values for spandrels associated with flexural failure.

Samples	$V_{u,4}$; Eq. (3.14) [kN]	$V_{u,5}$; Eq. (3.15) [kN]	$V_{u,6}$; Eq. (3.16) [kN]	$V_{u,7}$; Eq. (3.17) [kN]
W1	-	12.6	20.0	27.9
M1	-	30.6	203.7	30.4
T1	63.6	21.2	170.6	49.3

To compare the numerical to the experimental values the ratios shown in Table 3.19 are derived.

Table 3.19: Ratio of experimental to the numerical shear capacity values

Samples	$V_u/V_{u,4}$	$V_u/V_{u,5}$	$V_u/V_{u,6}$	$V_u/V_{u,7}$
W1	-	2.54	1.6	1.15
M1	-	2.29	0.34	2.30
T1	1.29	4.01	0.48	1.66

Based on the limited data, it is not possible to determine whether the formulations can represent the experimental tests. While Eq. (3.17) provides fair simulation for sample **W1** with 15% divergence, in all other cases there is a significant difference in the capacity results obtained from the equations. The parameters involved in this study are: i) the variations in the height of the spandrel between **W1** and **M1**, ii) the variation in the material type of the stone units between **W1** and **T1**, and iii) the application of axial force in case of **T1**. Given the limitations in the information due to the small number of samples it can be derived that the performance of the equations must

be revised. The divergence reaching more than 100% in certain cases raises red flags on the competency of those formulation and their ability to compute the capacity of spandrels.

3.4 Results

3.4.1 Pier Analysis

Four major parameters are identified for the shear capacity comparisons such as: the aspect ratio, the texture of the walls, the vertical stresses, and the scale of the specimens, respectively. The summary of findings are as follows (Figures 3.7a, 3.7b, 3.7c, and 3.7d):

- The shear capacity provided by Equation (3.1) works well with: i) full scale specimens, ii) irregular texture and iii) vertical stress levels between 0.25MPa and 0.5MPa.
- The shear capacity provided by Equation (3.2) works well for: i) scaled samples (1.2 aspect ratio), ii) rubble texture and iii) pre-stress level between 0.5MPa and 1.0MPa.
- The shear capacity provided by Equation (3.3) provides good simulations for: i) scaled samples (aspect ratio of 1 and 1.2), ii) sawn dry joint texture and iii) pre-stress levels less than 0.25MPa.
- The shear capacity provided by Equation (3.4) can simulate: i) scaled samples with aspect ratio of 1 and 1.2, ii) sawn dry joint texture and iii) pre-stress levels between 1.0MPa and 1.2MPa.

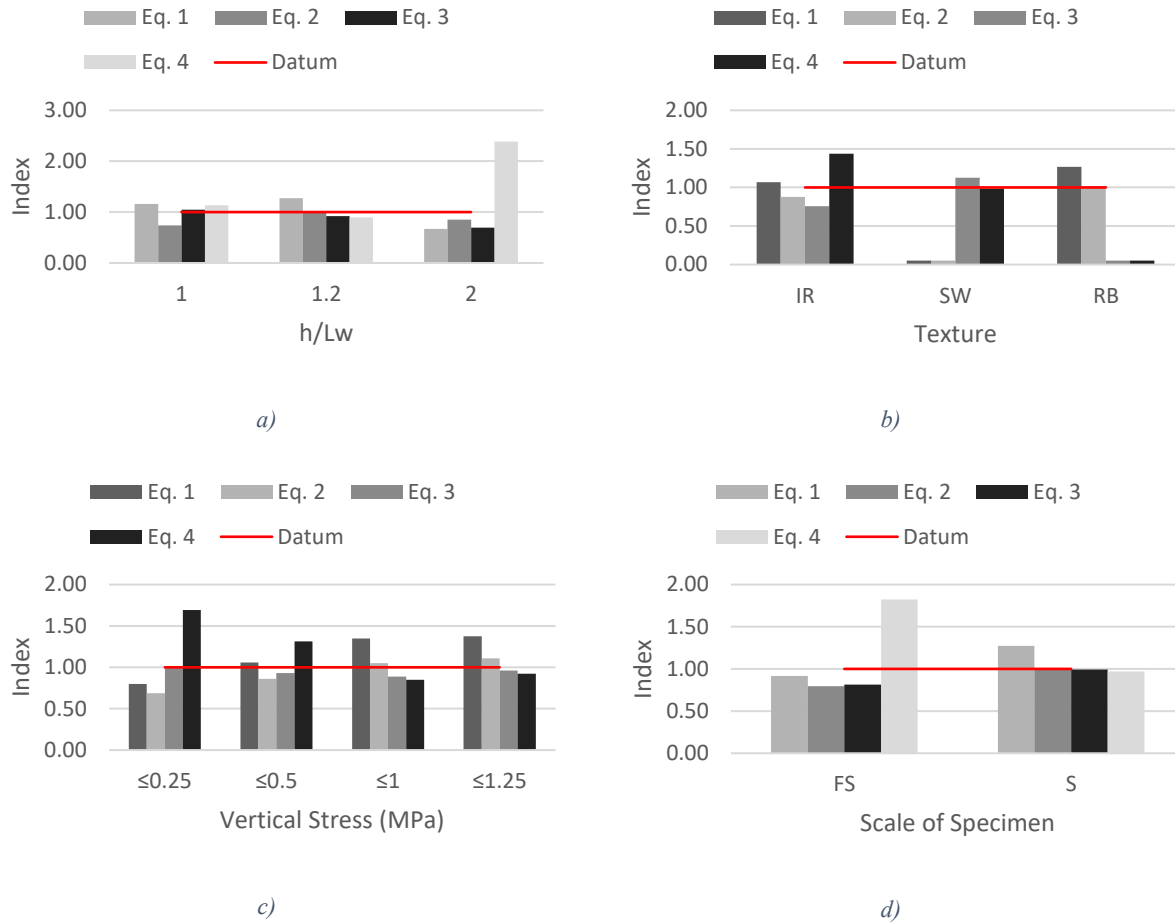


Figure 3.7: a) Indices for the four capacity formulations regarding aspect ratios b) stone textures c) vertical stresses d) scale factors

Seven major parameters were selected for the capacity formulations for flexure dominant behavior such as: the aspect ratio, the boundary conditions, the vertical stresses, the typology, the wall thickness, the scale, and the strengthening through injection. The findings are (Figures 3.8a, 3.8b, 3.9a, 3.9b, 3.9c, 3.9d, and 3.9e):

- Equation (3.5) shows good simulation for: i) scaled specimens and piers with aspect ratios between 1 and 1.5, ii) fixed boundary condition, iii) pre-stress levels between 0.5MPa and 1.0MPa, iv) bed joint mortared typologies, v) 330mm to 500mm wall thickness and vi) non-injected samples.

- Equation (3.9) shows similar results as that given by Equation (3.5) with more advantage for strengthened injected specimens.
- Equation (3.6) works well for: i) piers with 1 to 1.5 aspect ratios, ii) cantilever boundary conditions, iii) pre-stresses levels between 0.5MPa and 1.0MPa, iv) 200-330mm wall thicknesses and v) injected specimens.
- Equation (3.7) has good simulation for: i) piers with 1 to 1.5 aspect ratios, ii) fixed boundary conditions, iii) vertical stresses between 0.5MPa and 1.0MPa, iv) 330 to 500mm wall thicknesses and v) bed joints mortared specimens.
- Equation (3.8) works well for: i) full scale samples and pier aspect ratios ≤ 1.0 , ii) pre-stresses level $\leq 0.5\text{MPa}$ and iii) wall thicknesses $\leq 200\text{mm}$.

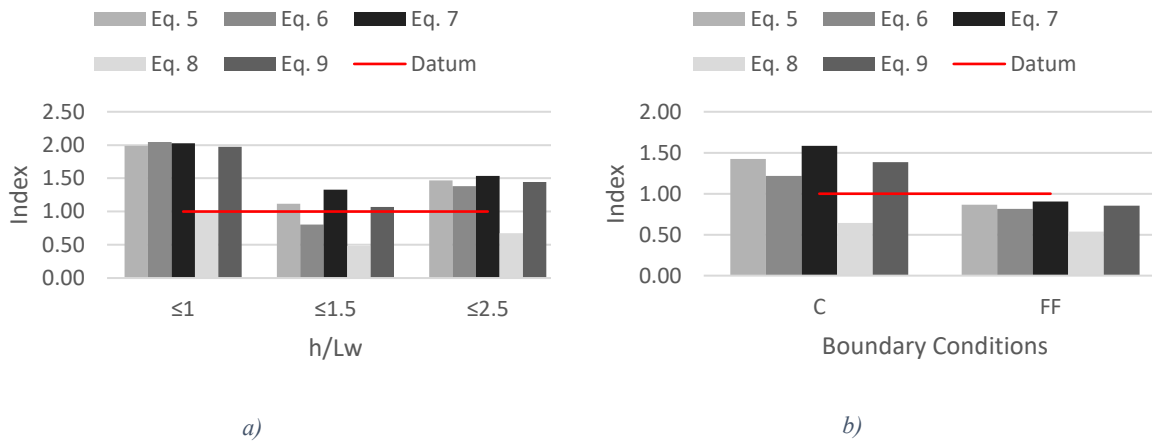


Figure 3.8: a) Indices for the five capacity formulations regarding the aspect ratios b) boundary conditions

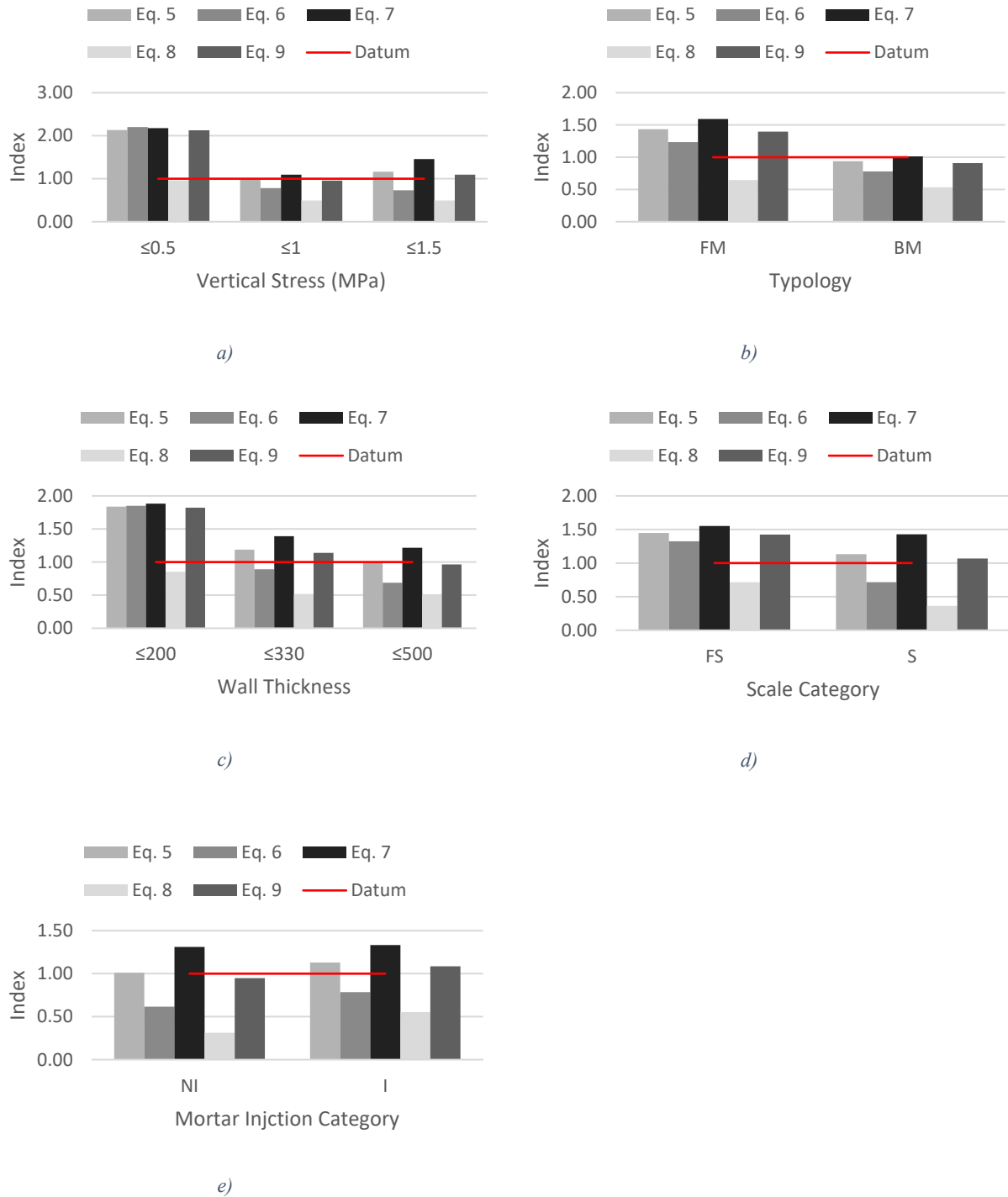


Figure 3.9: a) Indices for the five capacity formulations regarding the vertical stresses b) typology c) wall thicknesses d) scale factors e) mortar injection

3.4.2 Spandrel Analysis

The variation in the parameters between unreinforced masonry constructions indicates the necessity to verify their influence on the behavior of the elements in seismic action. It is realized from the literature of performed experimental data collection that the failures in spandrels associated with shear cracks are more common than those associated with flexural cracks. This explains the fact that the parametric study in this work has more data to evaluate the shear formulations. Each equation from different codes or suggested by researchers is yielding different results showing that the calibration process to which the equations are proposed has a significant impact on its performance.

Regarding the shear failure mode of spandrels, the parameters to consider are: the axial force, lintel thickness, length and height of the spandrel. It is shown that the simulations are better at lower axial forces, lower lintel thicknesses and higher heights of spandrels, while it remains indifferent for the length of the spandrels. It is also derived that Equations (3.11) and (3.12) perform better for stone unit samples in comparison to the brick unit samples, while the relations swaps for Equation (3.10).

Regarding the flexural failure mode of spandrels, the number of samples found in the literature was not enough to yield any deduction which shows the need for more experimental tests on spandrels. In general, there is a high divergence in the results for all the parameters involved. Also, Equation (3.13) is not reliable for samples without axial forces. As more data are acquired it would reveal a better connection between the different parameters of spandrels and the suggested equations which will help in refining the modeling approach utilized by decreasing the size of the error generated and encompassing a bigger number of parameters.

In summary, the parametric study on URM elements is used to develop correlation factors between their characteristics and a group of seismic capacity equations. Indices are generated for both shear and flexural dominant behavior modes that show the accuracy of such correlations. Four shear formulations and five flexural formulations for masonry piers, and seven shear formulations for spandrels are utilized to generate the in-plane cyclic experimental data and compare the results in terms of divergence ratios. It was found that each proposed equation can specialize in determining the lateral shear capacity of URM piers based on a variation of a set of major parameters that can highly influence its performance. More data is required to give better results for the spandrels.

Chapter 4:URM Capacity Estimation Using Distributed Plasticity Models for Linear Data Correlations

The behavior of masonry piers is well understood using more detailed models that are built with the objective of analyzing the data and predicting the future performance of those structural elements during the horizontal shaking. For this reason, a deterministic model is created using the open-source software OpenSees (McKenna et al., 2000) using the distributed plasticity applied through an equivalent frame macro modeling technique. The model had to be calibrated against experimental tests on piers representing the behavior dominated by shear and flexure. Once the calibration is accomplished, it is then possible to generate data based on multiple variations in the parameters which are assessed for their influence on the performance and the strengthening criteria of the piers. Thus, making a useful tool for predicting strengthening interventions that can have the optimal impact on the walls. It is realized that some parameters as the length of the piers has the highest influence on the piers making the openings in the walls a critical issue to be discussed in any future strengthening interventions.

4.1 Distributed Plasticity Model

4.1.1 Numerical Model Using OpenSees

The application of the modeling is performed in the open source computational platform (McKenna et al., 2000) due to its flexibility in incorporating constitutive laws that are able to simulate the in-plane behavior of URM walls using macro-element approach. One force-based element is used to represent the piers and thus ensuring the equilibrium at the force level between flexure and shear that is essential for determining the dominant type of failure. The cross section is discretized in fibers elements that accounts for the interaction between the moment and axial forces automatically represented in Fig. 4.1. A phenomenological (based on experimental work)

law is used to represent the cyclic response of shear which is coupled with the fiber section in the framework of Timoshenko beam theory (considering both the shear deformation and the axial force-moment interaction) as demonstrated in Fig. 4.2.

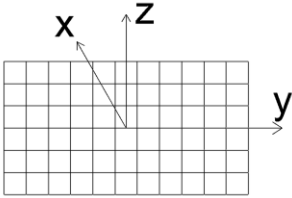


Figure 4.1: Fiber section discretization

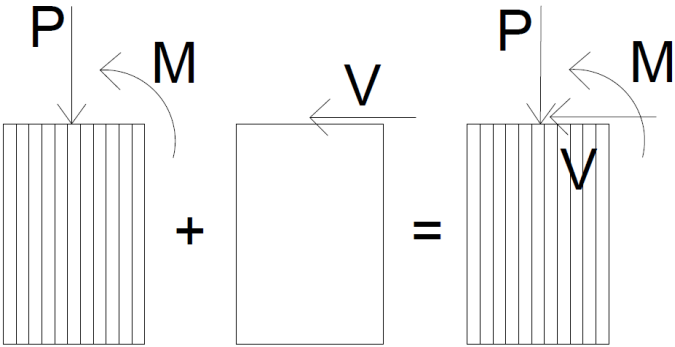


Figure 4.2: Coupling of shear law into the fiber section

Borrowed from the OpenSees uniaxial material library, the concrete material *Concrete02* is used to represent the flexural behavior in the piers (Mohd Yassin, 1994). This material is characterized with linear tension softening, which is important in the stabilization of the material during the lateral shaking due to the absence of reinforcement in the section. Shown in Fig. 4.3, the material captures the unconfined behavior (Kent & Park, 1971) in compression expressed in the negative side of the graph and considering the unloading path for the cyclic response. The positive quadrant represents the tension behavior with the maximum tensile strength and the tension softening stiffness (not to scale).

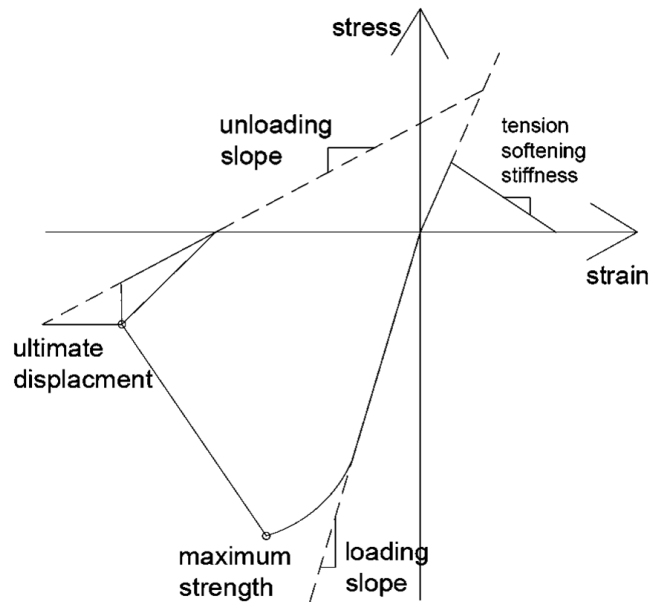


Figure 4.3: Concrete02 material as defined in OpenSees (McKenna et al., 2000)

Additional elastic fibers at the corners of the pier section are added with very small cross-section and high stiffness to help with the convergence of the analysis without having any effect on the response. A 20 mm² area and 1000 MPa modulus of elasticity are used as suggested by (Peruch et al., 2019).

For the representation of the shear behavior of unreinforced masonry, a hysteretic uniaxial material in OpenSees known as Hysteretic is used. The constitutive law is representative of the whole element through shear force and shear strain points, unlike the previous one which is a characteristic of the material itself. Shown in Fig. 4.4, it is a trilinear curve in both the positive and negative direction of force application. The material also covers the force and deformation pinching, the damage due to ductility and energy and degraded unloaded stiffness.

The failure of the pier is determined by the dominant type of the materials established by the minimum force capacity that varies depending in the characteristics of the wall. Throughout the

analysis, the shear strength is not affected by the vertical force. Also the vertical force resulting from the self weight of the pier and the carried weight from the upper floors is set to be constant.

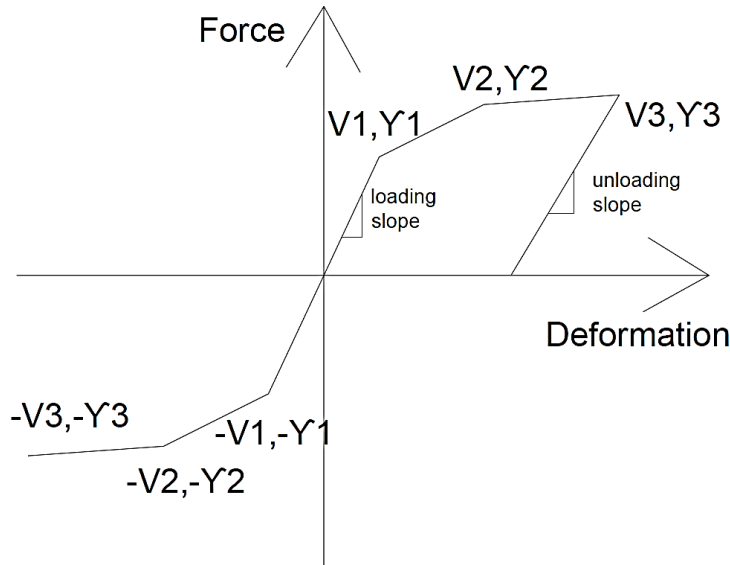


Figure 4.4: Hysteretic material as defined in OpenSees (McKenna et al., 2000)

4.1.2 Model Calibration & Validation

In order to validate the model, a simulation for quasi-cyclic experimental tests on two masonry piers, led by (Anthoine et al., 1994), was utilized for the demonstration. The piers **A** and **B** has different aspect ratios of 1.35 m and 2 m respectively which are typical for existing masonry construction in Italy. Both piers have similar length and thickness of 1.0 m and 0.25 m as demonstrated in Fig. 4.5. Throughout the experiment, a constant vertical force $N = 150 \text{ kN}$ is applied through a hydraulic jack with double bending boundary conditions replicated in the models by fixing the rotation at the top of the panel. Quasi-static loading with predetermined displacement increments is performed.

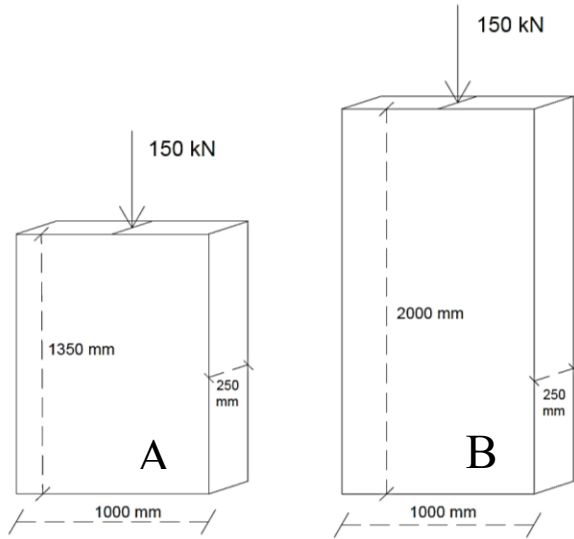


Figure 4.5: A) squat pier; B) slender pier as tested after Anthoine et al.(1994)

The parameters for *Concrete02* material are calibrated based on experimental tests made of masonry prisms with maximum compressive strength $f_m = 2.7 \text{ MPa}$ and maximum tensile strength $f_t = 0.18 \text{ MPa}$. The maximum and ultimate strain are calibrated to fit the experimental response.

The resulting constitutive law is represented in Fig. 4.6.

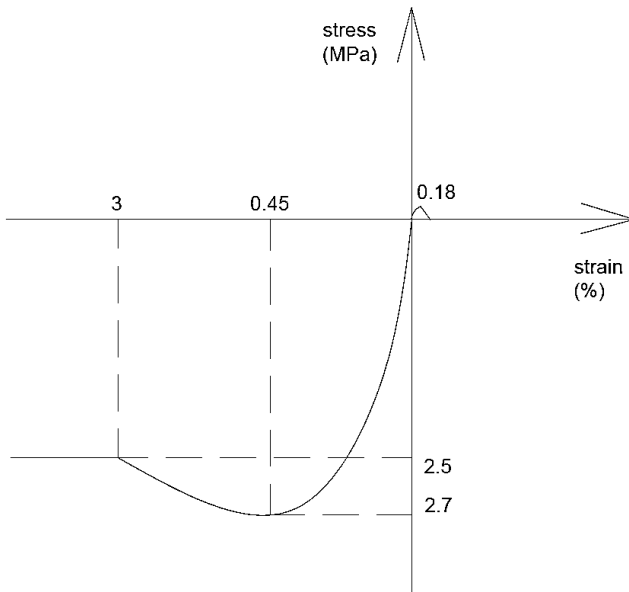


Figure 4.6: Constitutive law for *Concrete02* for piers A and B

The force parameters for the Hysteretic material are calculated based on the simplified capacity formulations associated with diagonal shear failure presented in Table 4.1. The formulation with the most accurate predictability of the maximum strength of the pier is used to calculate the maximum shear force V_m . For the squat sample, the maximum experimental strength associated with shear behavior is $V_m = 82$ kN (That associated with flexural behavior cannot be known experimentally but it should be larger than 82 kN). As for the slender sample, the maximum experimental strength associated with flexural behavior is 71 kN (That associated with shear behavior cannot be known experimentally but it should larger than 71 kN). Shown in Table 4.1 are four capacity formulations for unreinforced masonry walls associated with shear behavior that are used to calibrate the hysteretic material. The most accurate is Equation (3.1) (Turnšek & Čačovič, 1971) to a factor of 1.18. This will represent the floating point V2 in Fig. 4.4.

Table 4.1: Unreinforced masonry capacity formulations associated with shear behavior used to calibrate the numerical model.

Formulation	Source	V_m (kN) Squat	V_m (kN) Slender
$V_{m,1} = (f_v b_w L_w + 0.25N) \gamma_g$	Clause 7.10.1.1. (CSA 5304.1-04, R2010)	101.1	101.1
$V_{m,2} = \frac{f_t L_w b_w}{\xi} \sqrt{1 + \frac{\sigma_o}{f_t}}$	(Turnšek & Čačovič, 1971)	69.4	62.5
$V_{m,3} = \frac{c + \mu_s \sigma_o}{1 + \alpha_v} (L_w b_w)$	Coulomb criterion corrected by (Magenes & Calvi, 1997b)	51.3	43
$V_{m,4} = P \tan \phi \left[1 - \frac{h}{2L_w} \tan \phi \left(\frac{1}{1-\nu} \right) \right]$	(Lourenço et al., 2005)	12.6	12.1

The remaining floating points are determined as a percentage of the maximum strength. Point V1 that designates the end of the elastic behavior of the material is taken as 90% of V2 (Magenes & Calvi, 1997b) and (Tomazevic, 1996). Other literature based on experimental work suggest a value of 60% of V2 (Peruch et al., 2019) and (Peruch Matteo et al., 2019). Point V3 designates the end of the plastic behavior of the material and is specified as 50% of V2. The deformation parameters

can be determined through subtracting the flexural displacement due to the *Concrete02* material alone from the total displacement response found in the experiment and then dividing by the height of the panel. This method is justified using the force-based element that ensures the equilibrium of forces between shear and flexural at the fiber section level. Therefore, as the lower force will dominate the response of the element, the displacement from both behaviors will add up. Shown in Fig. 4.7 the difference in displacement between the total response envelope of the experiment on the squat pier and the flexural response envelope after applying a cyclic load on the element with *Concrete02* material only. The deformations are then obtained by dividing the difference in displacement by the height of the squat pier.

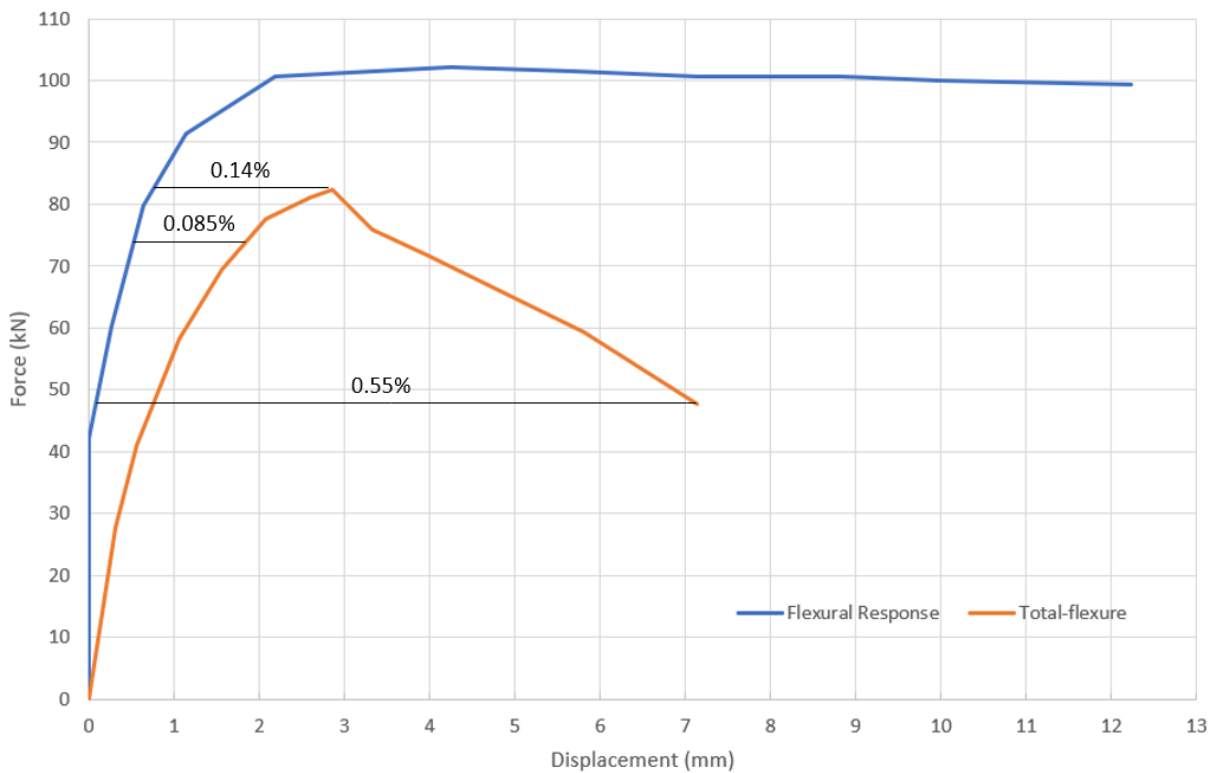


Figure 4.7: The difference between the total response and the flexural response in the squat pier

The Hysteretic parameters for shear forces and shear deformations are thus presented in Table 4.2.

It is important to note that at the ultimate displacement, the deformation of the pier is governed by

shear deformation only because the force associated with flexural response is higher than the total response. The constitutive law for shear behavior is then represented in Fig. 4.8.

Table 4.2: Hysteretic parameters after calibration to represent the shear behavior of the pier.

V1 (kN)	V2 (kN)	V3 (kN)	Y1	Y2	Y3
76	82	45	0.00085	0.0014	0.0055

Using the Aggregator command in OpenSees, the two constitutive laws are coupled within the fiber section. The cyclic load is applied based on displacement increments reaching up to 7.5mm for failures associated with shear and 12.5mm with failures associated with flexure to match the experiment. The loading is shown in Table 4.3.

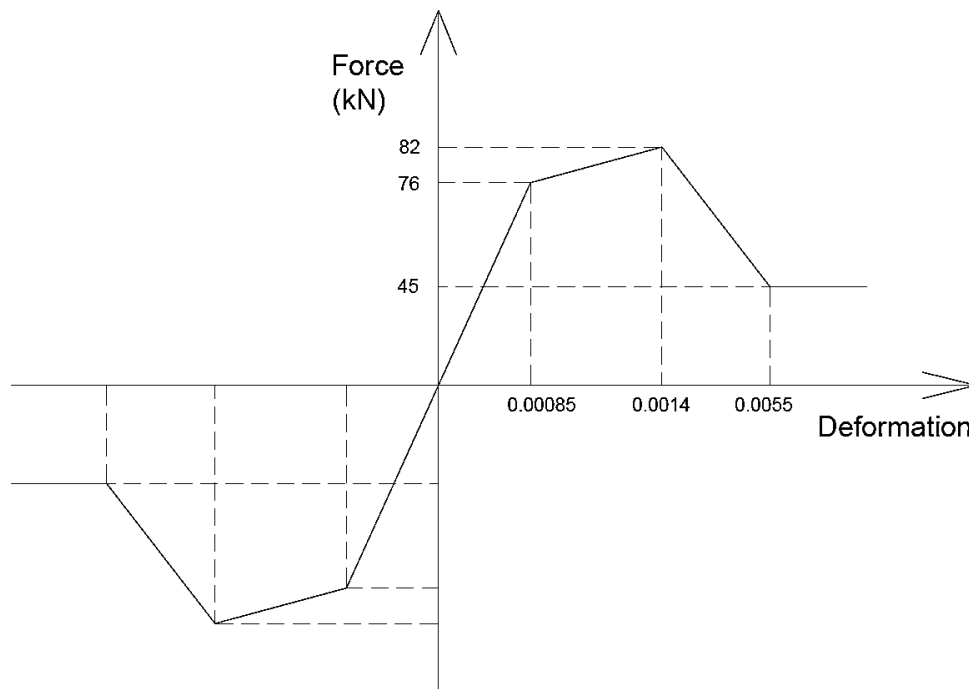


Figure 4.8: Constitutive law for Hysteretic material after calibration

Table 4.3: Incremental displacements for the quasi-cyclic loading on the top of the pier

Disp (m)	0	0	3	-3	4.5	-4.5	6	-6	7.5	-7.5	10	-10	12.5	-12.5	0
Steps	0	20	30	30	30	30	30	30	30	30	40	40	40	40	30

The squat pier response is presented in Fig. 4.9. The behavior is dominated by shear mode as the *Hysteretic* material is activated to capture the lateral response.

The model captures the positive and negative envelope to a very good precision. The initial stiffness is underestimated. However, the elastic displacement, the maximum strength and the strength degradation is well simulated. It also shows that the energy dissipation and the pinching behavior is well captured as well.

In Fig. 4.10, the slender pier response is presented. The behavior is dominated by flexural mode where the *Concrete02* material is activated. It is worth noting that in both cases the total response of the pier is influenced by the non-dominant material at the displacement level as to preserve the equilibrium in the force-based element as explained in previous sections. Thus the total response will accumulate additional displacements up to the level of the maximum force of the non-dominant material. In Fig. 4.10 the stiffness of the model is captured to a good extent along with the envelope on the positive and negative sides. The maximum strength and the strength degradation is well simulated. The energy dissipation and the pinching of the material is fairly representative of the experimental response.

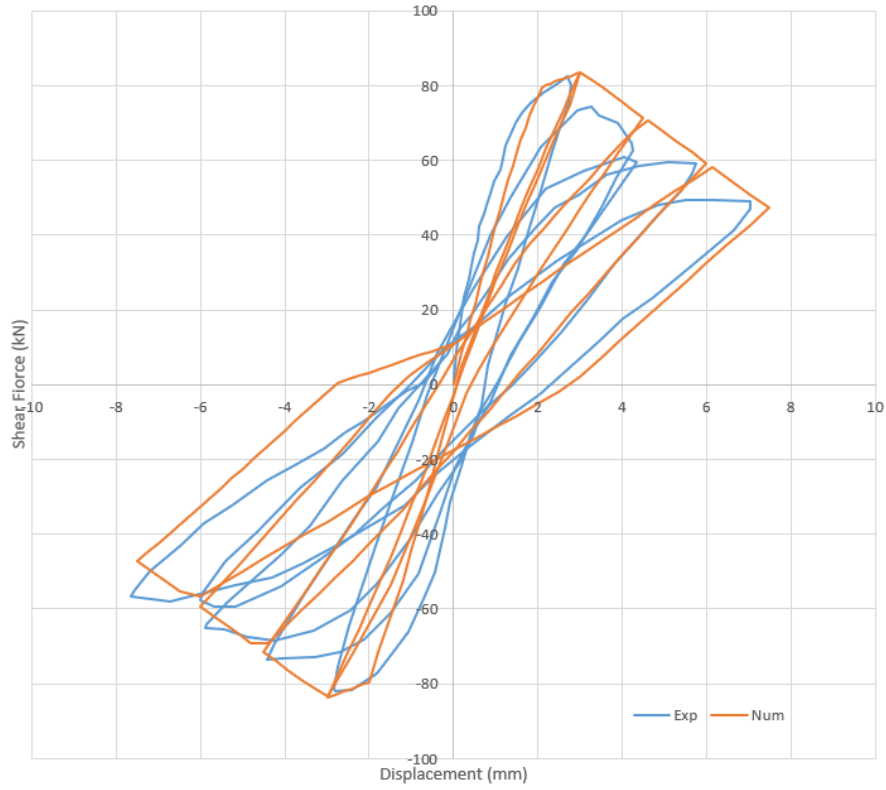


Figure 4.9: Response of the squat pier to the cyclic loading dominated by shear behavior.

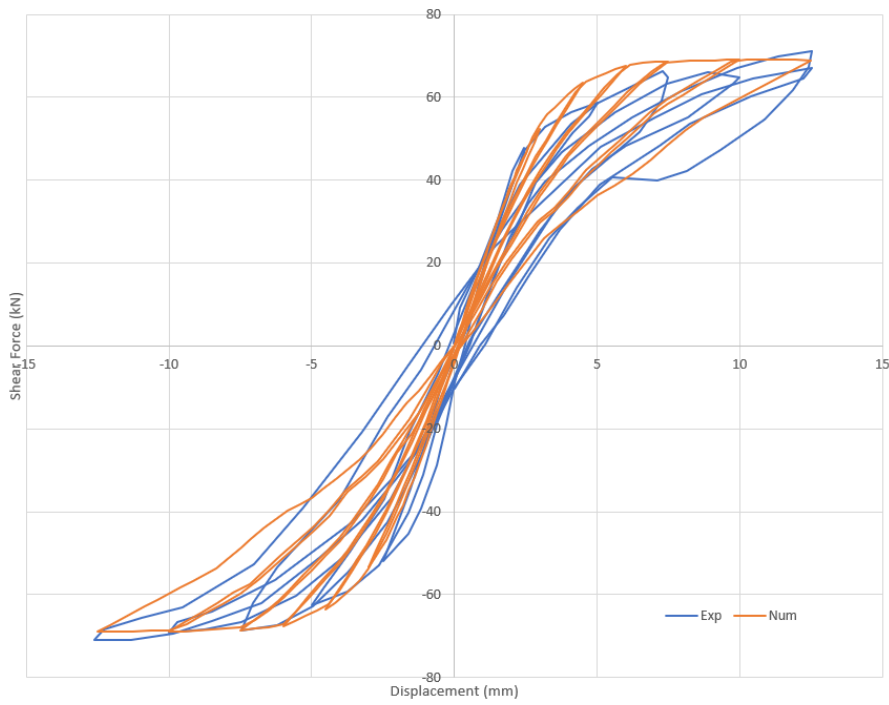


Figure 4.10: Response of the slender pier to cyclic loading dominated by flexural behavior.

4.2 Data Generation and Linear Correlation of Parameters for Strengthening Interventions

In the attempt to understand the influence of different parameters on the behavior of the piers, a linear parametric analysis is conducted for both the shear and flexure dominant type of failures. The information about the pier is defined through its base shear capacity and its displacement. For the shear dominant behavior, the height, length, thickness, and the vertical forces on the pier are evaluated. While for the flexural dominant behavior, the same parameters are considered in addition to the tensile modulus of elasticity. The method followed for such evaluation is to fix all the parameters except for the variable being tested, then determining the strength of the pier along with the variation. The method will apply separately for each dominant type of failure through limiting the variable into a range that will induce the needed mode. Enough data is generated to be able to construct a correlation between the variables. More information on the shape of the hysteretic loops showing the response of the piers due to the cyclic loadings applied is presented in the Appendix A.

4.2.1 Correlations for Shear Dominant Failure Mode

The parameters that are found to directly influence the strength criteria of the piers dominated with shear behavior are the height h , the vertical forces N , the length L and the thickness t presented as independent variables in Table 4.4. The ranges for the independent parameters are limited to the values that induce a shear failure. The strength criteria are the maximum displacement D_{max} (displacement at maximum base shear strength), the ultimate displacement D_{ult} (displacement at the failure of the pier), and the maximum base shear strength V_{max} . Those are listed as the dependent variables in the table below.

Table 4.4: The correlation values between the major parameters and the strength criteria of the piers with shear dominant behavior

Independent Variable	Range	Dependent Var.	R ²	Linear Equation
Height H	0.5 – 1.5 (m)	D _{max}	0.9245	y = 3.63x – 1.56
Height H	0.5 – 1.5 (m)	D _{ult}	0.9779	y = 6.27x – 0.66
Vertical Force N	60 – 300 (kN)	V _{max}	0.9898	y = 0.20x – 53.9
Length L	0.9 – 2 (m)	D _{max}	0.8459	y = -x + 3.83
Length L	0.9 – 2 (m)	V _{max}	0.9995	y = 48.5x + 36.0
Thickness t	200 – 600 (mm)	D _{max}	0.6577	y = 0.003x – 2.3
Thickness t	200 – 600 (mm)	V _{max}	0.9976	y = 0.2x + 38.8

The statistical variable R² representing the degree to which the data points for a particular distribution have the tendency of forming a linear relationship. The equation of the linear line is then calculated and stated in the table representing the potential linear relationship between the independent and dependent variables. Thus, those equations constitute preliminary correlation between the parameters of the piers under analysis and the strength criteria to be predicted by the model. This linear relationship is generated using the graphs shown in Figs. 4.11a to 4.11f. Those graphs are constructed using the random data generated by the calibrated model and limited to the ranges assigned above. Those will serve a critical role in understanding the influence of altering those parameters on the strength of the piers. Figure 4.11a shows that increasing the height of the specimen will increase both the maximum and ultimate displacements indicating the additional flexibility associated with taller piers. The slope of D_{ult} is double the slope of D_{max} which indicates that the rate of gaining flexibility towards the failure of the piers is higher than the gain towards the maximum shear strength. Figure 4.11b shows that the increase in the vertical forces on the piers will increase the maximum shear strength due to the stability induced by the vertical stresses thus reducing the tensile vulnerability at the weak bond between the stones and the mortar.

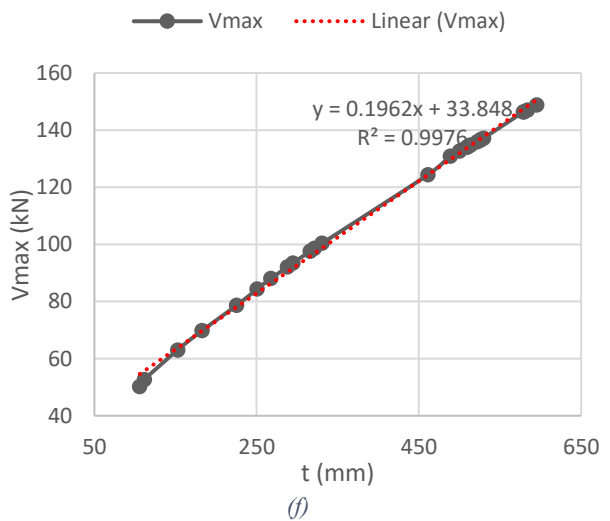
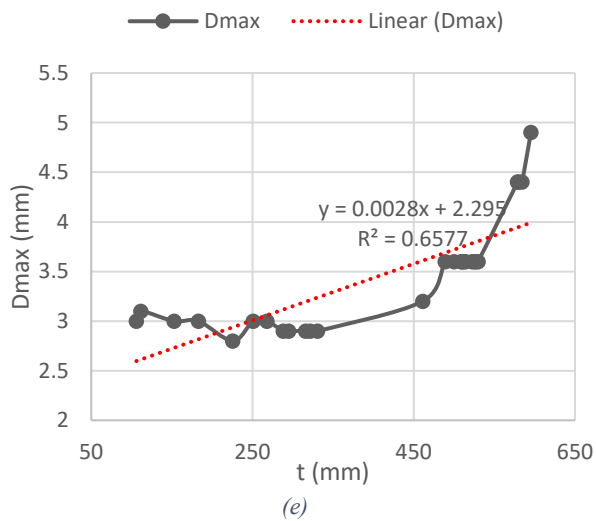
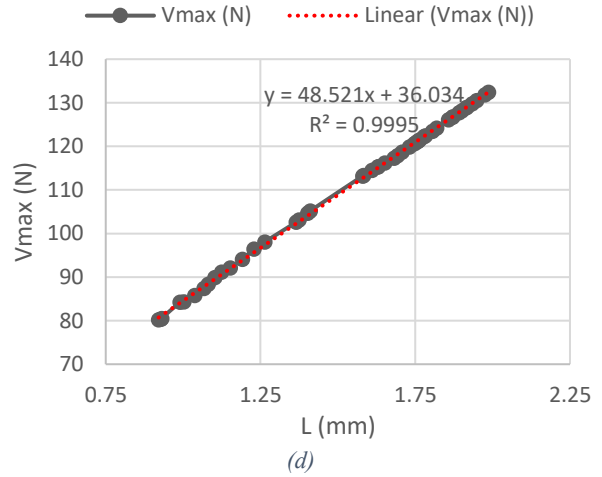
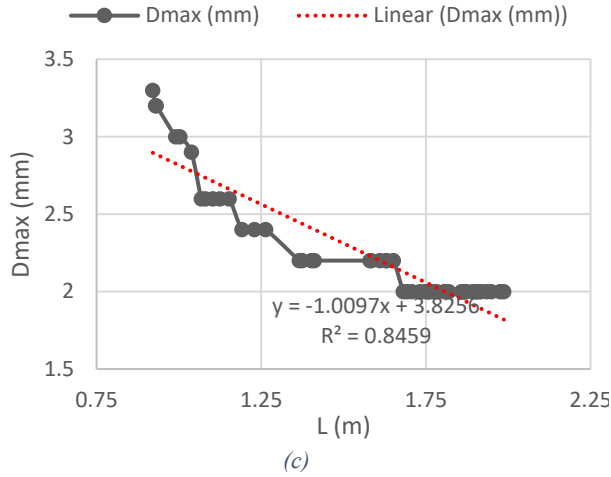
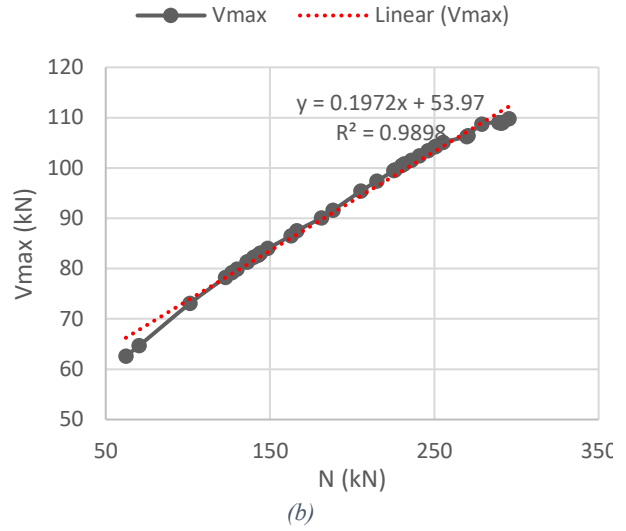
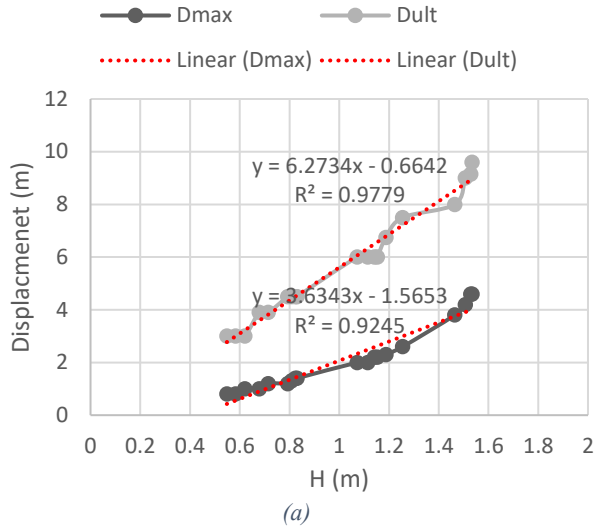


Figure 4.11: a) Variation of Dmax and Dult w.r.t the height b) Vmax w.r.t. vertical forces c) Dmax w.r.t. length d) Vmax w.r.t. length e) Dmax w.r.t. thickness f) Vmax w.r.t. thickness

Figures 4.11c and 4.11d shows the correlation between the displacement, strength, and the length of the piers. Increasing the length of the pier is adding stiffness which reduces the displacement and increases the strength. It is good to note that the R^2 value for the linear relationship between the length and displacement is 0.8459 due to the plateauing in the data observed in the graph. The slope of linear relationship between the length and the shear strength is 48.5 indicating a high gain in the strength. This shows the strong influence of such intervention on the behavior of the pier and thus could be considered as potential parameter to work on for rehabilitation projects. Figures 4.11e and 4.11f shows the relationship between the thickness of the piers, displacement, and strength. The R^2 value for the linear relationship between the displacement and the thickness is 0.6577 indicating a discrepancy in the data reflected in the spikes and plateauing of the data observed in the graph. In general, increasing the thickness increases the maximum displacements. However, the actual influence appears after a thickness of 450 mm and the slope of the linear line is low at 0.0028. The increase in the thickness increases the strength of the piers with a slope of 0.1962 and good data correlation. The thickness parameter could be good starting point, despite the inconsistency of the data in Figure 66, to increase the strength of the element without sacrificing the stiffness to a great extent. A strengthening intervention that serves in this direction is of great benefit to the URM structures.

4.2.2 Correlations for Flexural Dominant Failure Mode

In the same manner, data is generated for the piers with flexural dominant behavior using the major parameters using the specified ranges shown in Table 4.5. The strength criterion is limited to the maximum and ultimate based shear extracted from the cyclic loops due to the limited variations in the displacements. This is due to the flexibility associated with flexural behavior. Figure 4.12a

shows the correlation between the V_{\max} and the height H of the pier with the lowest R^2 value in the list equal to 0.88. The negative slope of the linear relationship between the data is -10.3 indicating the increase in the height of the pier will lower its base shear strength. A good practice in such case is to ensure the rigidity of the connection at the top of the pier which limits the height of the pier to the first adjacent opening without extending to upper floors.

Table 4.5: The correlation values between the major parameters and the strength criteria of the piers with flexural dominant behavior

Independent Variable	Range	Dependent Variable	R^2	Linear Line Equation
Height H	1.9 – 7 (m)	V_{\max}	0.8793	$y = -10.3x + 75$
Compressive Strength f_m	1.4 – 4.7 (MPa)	V_{\max}	0.9648	$y = 6.1x + 50.95$
Tensile Strength f_t	0.07 – 0.3 (MPa)	V_{\max}	1	$y = 62.3x + 56.9$
Tensile Modulus E_t	1 – 10 (MPa)	V_{\max}	0.9872	$y = -0.4x + 67.9$
Tensile Modulus E_t	1 – 10 (MPa)	V_{ult}	0.9890	$y = -0.9x + 68.6$
Vertical Force N	10 – 175 (kN)	V_{\max}	0.9896	$y = 0.33x + 20.8$
Length L	0.5 – 1 (m)	V_{\max}	0.9996	$y = 94.8x + 27$
Thickness t	200 – 800 (mm)	V_{\max}	0.9888	$y = 0.09x + 46$

Figure 4.12b shows the correlation between the maximum shear strength and compressive strength of the pier. Increasing the compressive strength has increased the strength of the pier with a slope of 6.1 for linear data and good R^2 value of 0.96. Increasing the compressive strength is dependent on the strength of mortar being the weakest material in the wall which can crush under the vertical pressure from gravity loads. A good practice for rehabilitation intervention is the injection of hydraulic mortar into the wall. Figure 4.13a shows a perfect correlation between the maximum shear strength and tensile strength of the pier. The slope for the linear relationship is 62.3 which indicates high influence of the parameter on the strengthening of the pier. The tensile strength of the pier is increased through improving the bond between the mortar and the stone units to enhance the cohesion and friction parameters. A careful replacement of the existing lime mortar in such wall with newer hydraulic or cement-based mortar can improve the performance considerably.

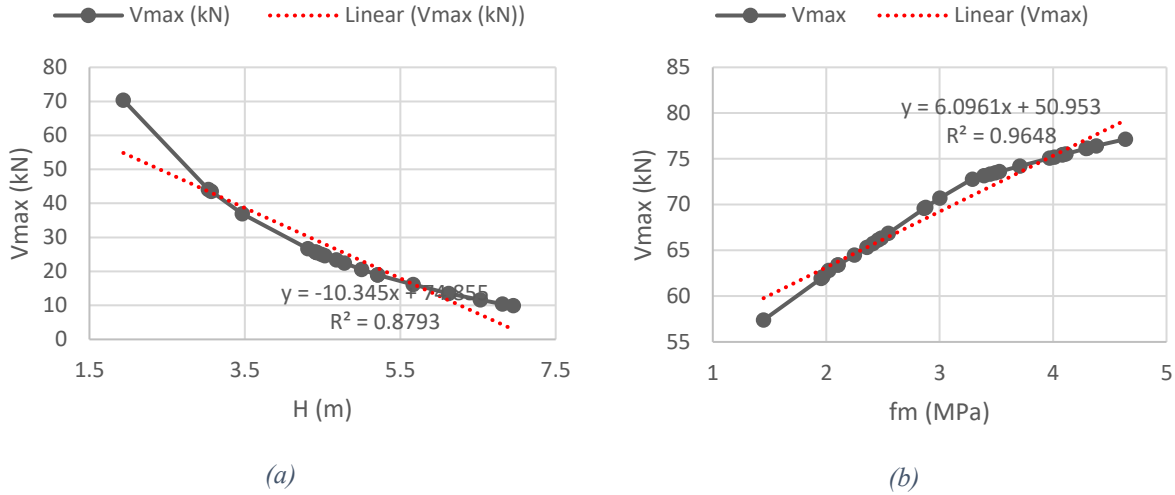


Figure 4.12: a) Variation of V_{max} w.r.t. height b) V_{max} w.r.t. compressive strength.

Figure 4.13b shows the correlation between the maximum and ultimate shear strength and the elastic tensile modulus of the pier. In general, the influence of this parameter is low on the strength criteria which is almost three time larger towards the ultimate strength at failure compared to the maximum shear strength. Figure 4.13c shows the correlation between the maximum shear strength and the vertical forces exerted on the top of the piers. There is a good correlation of the data but a low slope for the linear relationship indicating low influence in the strengthening criteria. The vertical forces are usually controlled by the number of stories above the intended pier and increasing such parameter for the intent of improving the strength could be on the detriment of the vertical capacity of the bearing walls. However, the improvement in the strength is due to tensile cracks closing phenomena that occurs through the vertical forces.

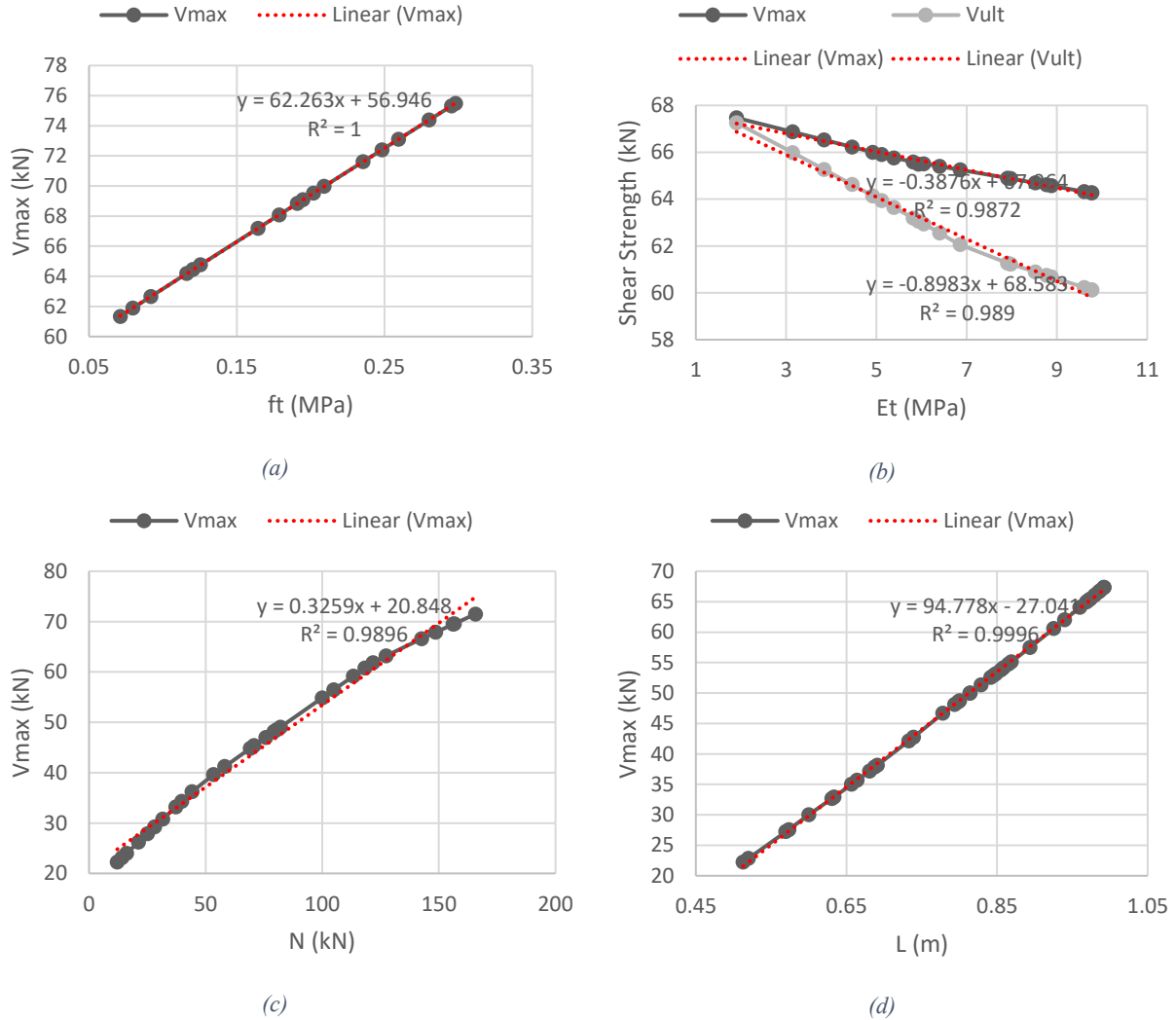


Figure 4.13: a) Variation of V_{max} w.r.t. tensile strength b) V_{max} and V_{ult} w.r.t. elastic tension modulus c) V_{max} w.r.t. vertical forces d) V_{max} w.r.t. length

Figure 4.13d is the correlation between the maximum shear strength and the length of the pier. With almost perfect correlated data and high slope for the linear relationship, it proves to be as a great influence on the strengthening criteria. For this reason, the size of the openings in the URM walls has a major effect on the performance of the walls. One practical intervention could be reducing the size of the openings or completely closing it depending on the practicality of the situation. Figure 4.14 shows the correlation between the maximum shear strength and the thickness

of the pier. The slope of the linear relationship is very low indicating a low influence on the strengthening criteria.

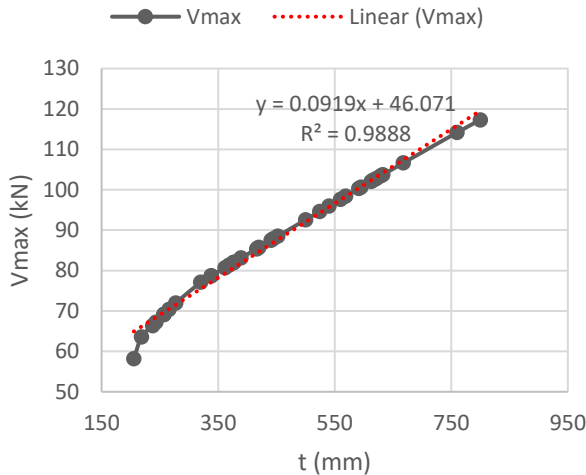


Figure 4.14: Variation of maximum base shear strength V_{max} with the thickness of the pier

4.3 Case Study - Piers Extracted from the Facade Wall of Villa Maria School Building

A case study in the city of Montreal is considered to study the behaviour of the URM piers in response to lateral forces simulated from earthquakes. The building selected in the Villa Maria School located on a Site Class C in the Westmount area in Montreal. The purpose of this study is to understand the results of the models generated in the previous chapters on a local structure of significant historical value. To build the model in OpenSees, several parameters need to be determined to define the characteristics of the pier. To identify the compressive strength of the walls covering the flexural behavior, experimental tests are conducted on mortar cubes made in the lab that resemble the lime mortar used in such existing URM structures. The results from the tests are then used to deduce the compressive strength of the piers using formulations from the literature generated based on previous experimental campaigns. On the other hand, the shear behavior of the piers is defined using the capacity formulations mentioned in Chapter 2. From the

analysis on those formulations, the best fit is selected to calculate the strength of the pier while the deformation is determined using the calibrated ratios for shear displacements in Chapter 3. Using the available maps of the building, the dimensions of the facade wall is extracted and two piers from the first and second floors are selected for the analysis. One pier showed a dominant shear behavior, and another pier showed a flexural dominant behavior. Referring to those two modes of responses, it was possible to use the probabilistic model presented in Chapter 4 to evaluate the most influencing predictive parameters that can be used to strengthen the wall to improve the building response.

4.3.1 Villa Maria School - Extraction of Parameters Using Available Resources



Figure 4.15: The central building of Villa Maria high school (main facade)

The case study is conducted on the central building of Villa Marie high school shown in Fig. 4.15. This stone masonry building was originally a convent and was built in 1804 (Parks Canada Agency, 1998). Recognized by its Neo-Palladian style, this building was the official residence for

the General Governor of Canada in the year 1844. To accommodate the change of building occupancy type, the building was renovated in the same year by the architect George Browne.

Hence, the case study is a two-story stone masonry building with basement. The stone masonry is classified as limestone originated from sedimentary rocks.

All plans of the building were obtained from the owner and the Congregation de Notre-Dame and are shown in Figs. 4.16, 4.17, and 4.18. From the building plans it results the following wall thicknesses: 519mm for the basement, 500mm for the first floor, and 432mm for the second floor.



Figure 4.16: Villa-Maria school elevation

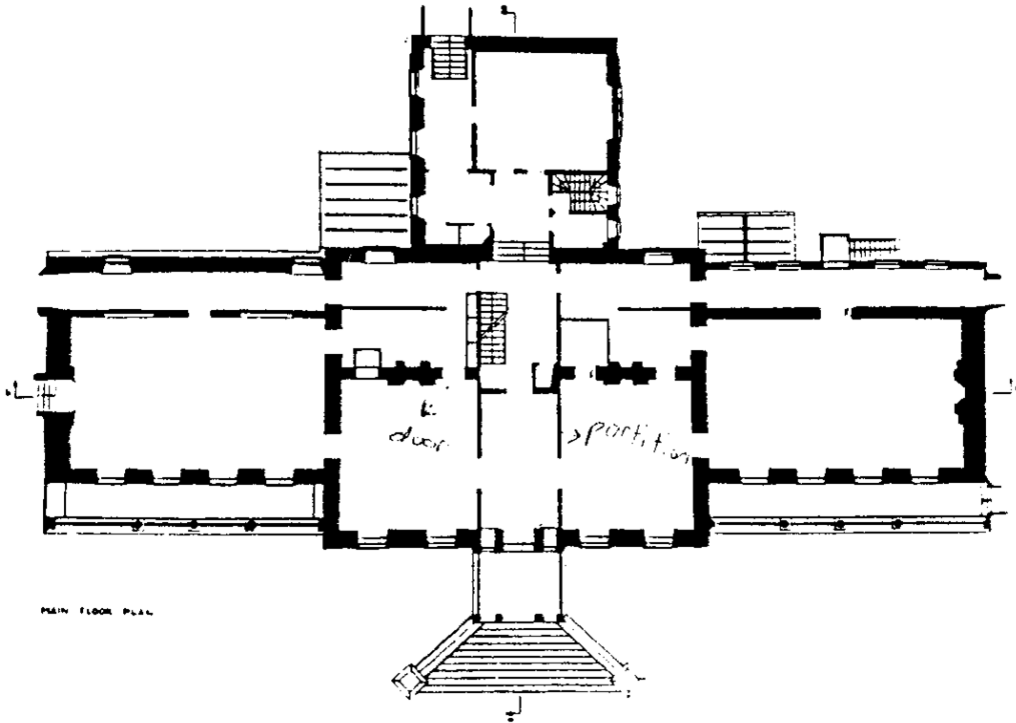


Figure 4.17: Main floor plan for Villa Maria school

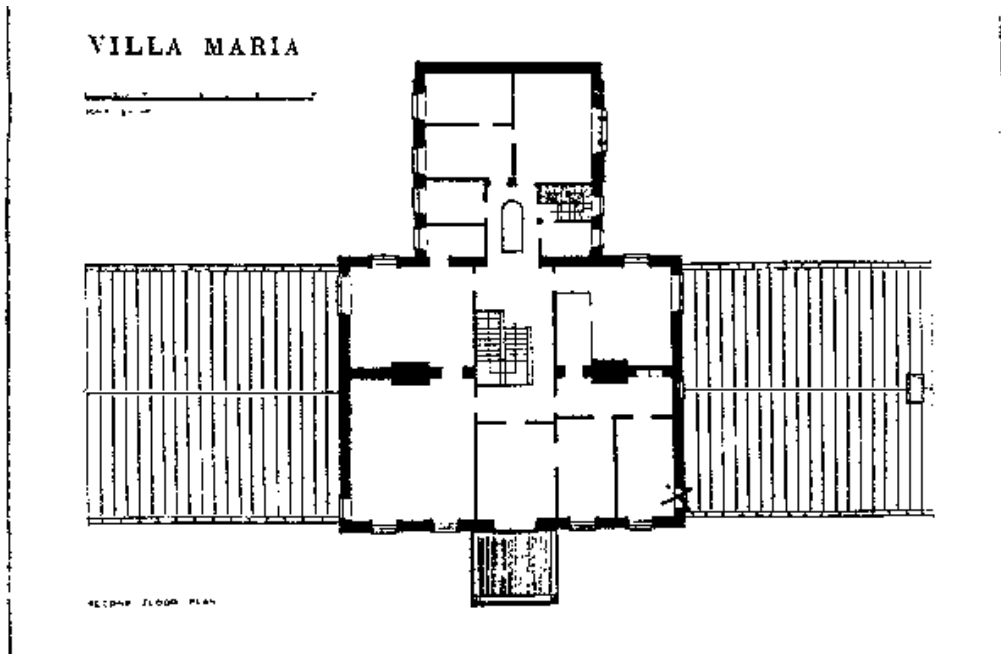


Figure 4.18: Second floor plan for the Villa Maria school

Using extrapolation method from the maps and actual measuring taken on site, the dimensions of the facade wall are extracted as shown in Fig. 4.19. **Pier 1** at the second floor and **Pier 2** at the first floor are selected to be analysed using the deterministic model in Chapter 3.

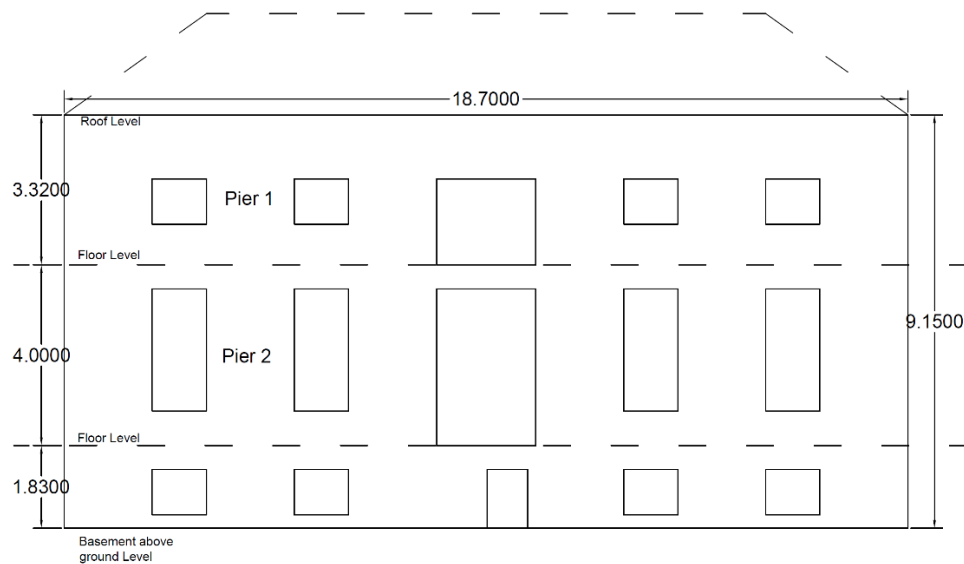


Figure 4.19: Facade wall of the Villa Maria school with extracted dimensions in meters

4.3.2 Preliminary Experimental Tests on Lime Mortar

In the aim of extracting the compressive strength of the masonry wallets used as parameters in defining the properties of the piers under examination, a set of compression tests are performed on mortar cubes selected based on different lime to sand ratios extracted from the literature shown in Figs. 4.20a and 4.20b. The sand specific density is 2702 Kg/m^3 while the lime specific density is 2370 kg/m^3 . For existing URM buildings, lime mortar was commonly used in the bed joints and head joints between the unit stones.



Figure 4.20: a) NHL hydraulic lime used in the mix of mortar b) Sand used in the mortar

Three different ratios are selected and presented in Table 4.6 based on mass proportions. Tests are done according to ASTM C109 (ASTM International, 2020) using 50 mm cubic molds and EN 1015-11 (EN 1015-11, 2019) for curing. Nine samples are taken from each batch to be tested at 7 and 50 days. Water is added in each batch until obtaining the same consistence. The resulting water to lime ratios is presented in Table 4.6 as well. The average of compressive strength obtained from all batches at 50 days are considered for further analysis as the ones obtained at 7 days are only used as a control.

Table 4.6: Different mortar to sand ratios used in the mix with their associated water to mortar ratios.

Batch	Proportions (L:S)	W/L ratios
A (1-2)	1 : 1.25	0.663
B (1-2)	1 : 1.75	0.573
C (1-2)	3.5 : 1	0.439

The whole preparation process for mixing the material, molding, and curing is presented in Fig.4.21. ASTM requirements are satisfied at every step of the tests (ASTM C 109), while also some conditions from the European norms are used guidance (EN 1015-11). After the cubes are ready, the molds are placed in plastic bags and stored for 2 days at room temperature after which



Figure 4.21: a) Mixing the mortar using a mechanical turbine b) ASTM certified molds c) Tapping the mortar at half the portion d) Finishing the surface of the mortar e) Curing f) Weight measuring.

they are removed from the molds and placed in plastic bags to finish the 7 days period at which the first set is tested. The remaining cubes are left without any bags at room temperature up to 50 days when the second set has been tested. Once the curing part is over, the mortar cubes are prepared for testing starting by measure the weight using a sensitive scale.

Typical testing procedure is presented in Fig. 4.22. The dimensions are taken using a calibrated caliper, then the cubes are placed under the crushing disks in the compression machine while the

load is applied gradually using a manual handle. A typical failure of the cubes is a split towards the edge due to weak tensile strength.

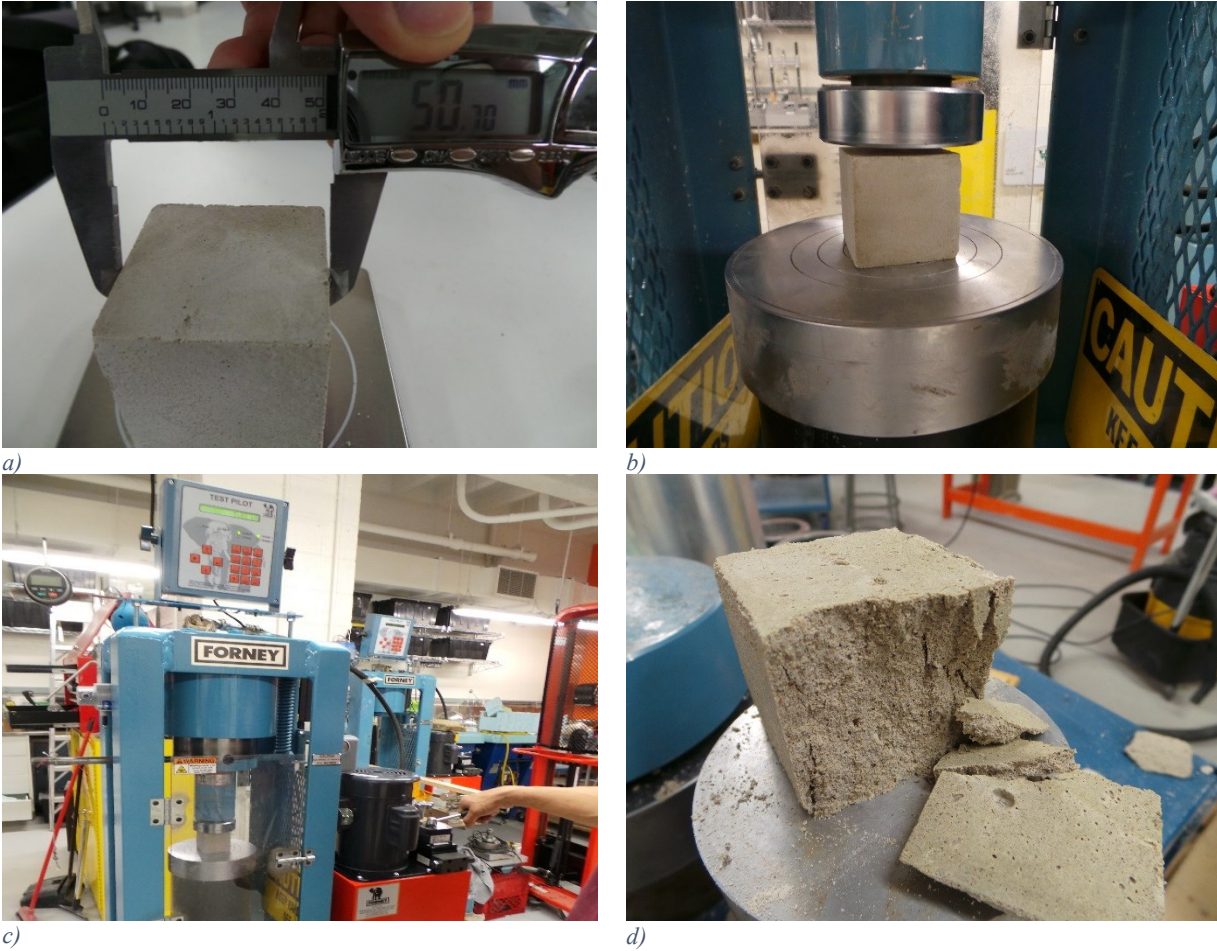


Figure 4.22: a) Measuring the dimensions b), c) Compressive strength test d) Typical failure in the mortar cubes.

The results of each batch with their equivalent average are presented in Table 4.7 at 7 days and in Table 4.8 at 50 days. The averages at day 7 are 1.1, 2, and 3.1 for batches A1, B1, and C1, respectively resulting in a total average of 2.1 MPa. The averages at 50 days are 2.6, 5.9, and 8.6 for batches A2, B2, and C2, respectively with a total average of 5.7 MPa. In a study on the ageing of lime mortar due to various conditions of exposure (Izaguirre et al., 2010), it is shown that the mortar suffers a 13.5% decrease in compressive strength due to climate exposure which includes changes in temperatures and humidity, and a 25% decrease in compressive strength due to freeze-

and-thawing phenomenon that is very common in Montreal. This will result in a total of 38.5% decay in the compressive strength in the compressive strength of the lime mortar existing in the Villa Maria building. Thus, the compressive strength is 3.5 MPa. This number will be used for further numerical investigations on the compressive strength of URM prisms and wallets.

Table 4.7: Compressive strength for the three batches at 7 days

A1	1	2	3	Average
Cross-sectional area (mm)	50.25x50.46	50.21x50.17	49.48x50.12	
Weight (g)	246.12	247.05	245.06	
Force P (KN)	2.65	2.61	3.14	
Strength Fm (Mpa)	1.1	1.0	1.3	1.1
B1	1	2	3	Average
Cross-sectional area (mm)	50.94x50.11	50.47x51.09	50.68x50.14	
Weight (g)	263.69	269.23	261.72	
Force P (KN)	5.14	5.08	5.40	
Strength Fm (Mpa)	2.0	2.0	2.1	2.0
C1	1	2	3	Average
Cross-sectional area (mm)	51.55x50.49	50.87x50.43	51.50x50.60	
Weight (g)	240.57	237.82	239.44	
Force P (KN)	7.78	8.14	7.70	
Strength Fm (Mpa)	3.0	3.2	3.0	3.1

Table 4.8: Compressive strength results for three batches at 50 days

A2	1	2	3	Average
Cross-sectional area (mm)	51.19x50.75	51.01x51.06	50.67x51.34	
Weight (g)	211.91	211.86	212.37	
Force P (KN)	6.55	6.62	7.26	
Strength Fm (Mpa)	2.5	2.5	2.8	2.6
B2	1	2	3	Average
Cross-sectional area (mm)	50.53x51.44	51.43x50.42	51.22x50.41	
Weight (g)	239.84	240.84	237.65	
Force P (KN)	14.74	16.75	14.03	
Strength Fm (Mpa)	5.7	6.5	5.4	5.9
C2	1	2	3	Average
Cross-sectional area (mm)	50.90x51.80	50.94x51.38	50.89x51.50	
Weight (g)	199.90	198.77	199.93	
Force P (KN)	23.14	22.34	22.45	
Strength Fm (Mpa)	8.8	8.5	8.6	8.6

In a study on the correlation between the compressive strength, thickness of mortar bed joints, and the compressive strength of URM prisms (Lima et al., 2012), an equation is extracted from the experimental tests:

$$f_p = 4.7 + 2.3 \ln(f_a) + 0.23e_a \pm 0.42 \quad (4.1)$$

Herein, f_p is the compressive strength of the prism, $f_a = 3.5 \text{ MPa}$ is the compressive strength of the mortar, and $e_a = 8 \text{ mm}$ is the thickness of the bed joint. This equation is used to deduce the prism compressive strength from a sample of the Villa Maria building walls. Using the equation, the compressive strength of an equivalent prism is $f_p = 9 \text{ MPa}$. In another experimental study on the correlation between the prism and walette compressive strength (Thamboo & Dhanasekar, 2019), an equation is developed in the following form with correlation coefficient $R^2 = 0.94$:

$$f_{m,wallette} = 0.75 \times f_{m,prism} \quad (4.2)$$

Using the equation, $f_{m,wallette} = 6.75 \text{ MPa}$. This value will be used as a parameter in the pier model.

4.3.3 Villa Maria School - Extraction of Parameters Using Available Resources

The stone masonry is classified as limestone originated from sedimentary rocks. A density test was performed in Concordia lab to identify its category. Weight measurements in the field conditions of two stone samples with different sizes that were made in water (w_{water}) and in air (w_{air}) and are illustrated in Figs. 4.23a and 4.23b. The density was calculated based on the following formula:

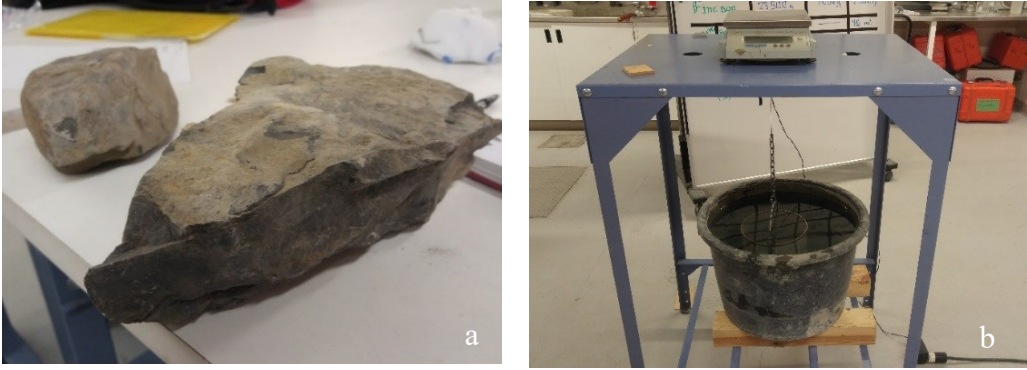


Figure 4.23: a) Limestone masonry samples collected from the field near the building prepared for density test b) Measurement of the weight in water using a chain hooked to the weight balance.

$$\rho_{stone} = w_{air} / (w_{air} - w_{water}) \quad (3)$$

The measurement yielded a density of 26.9 kN/m³ which is classified into compact limestone with unit compressive strength ranges between 78 – 186 MPa and unit elastic modulus ranges between 39000 – 68000 MPa (Mario Como, 2013). Another study on the physical properties of the Lindsay-Cobourg Limestone conducted at McGill University (Hekimi, 2012) shows similar values (saturated density of 26.9 kN/m³ and a dry density of 26.8 kN/m³) to those obtained in Concordia lab. The stone material is classified as argillaceous limestone with visible heterogeneity ranging between light to dark grey color that are formed as a sub-division of the Middle Ordovician Limestone in Southern Ontario bedrock. The uniaxial compressive strength of the unit stone ranges between 22MPa and 140 MPa. Scanning the literature to find experimental tests conducted on stone masonry assemblages to extract the initial shear and compressive strength of small wallets, it was found that a diagonal shear test was performed using Credaro sandstone originating from sedimentary rocks with density of 25.79 kN/m³ and a unit compressive strength ranging between 165MPa and 172 MPa.

Thus, the values extracted from these experimental tests were used to develop the shear strength formulations in this paper. The preliminary mechanical properties considered for the stone

masonry assemblage are: $E_m = 2550$ MPa; $f_t = 0.137$ MPa tensile strength; and $G = 840$ MPa (Magenes, Penna, Galasco, & Rota, 2010).

4.3.4 Distributed Plasticity Model in OpenSees

Pier 1 at the second floor and Pier 2 at the first floor marked in Fig. 4.24 are selected to be analysed using the deterministic model presented in Chapter 3. The piers vertical loads are calculated based on the density of the stone masonry and the volume of the tributary area carried by each pier. A sketch of each one is shown in Fig. 4.40. The height of the piers is determined using the 30 degrees angles method (Dolce, 1991).

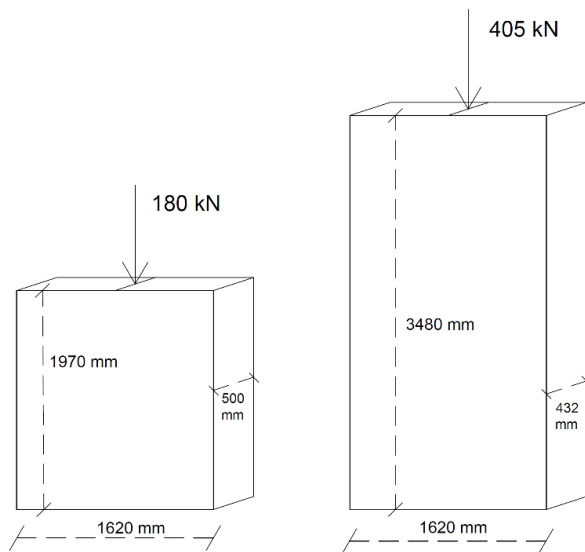


Figure 4.24: Illustration of pier1 (left) and pier2 (right) selected from the facade wall.

To calculate the capacity of the wall for the shear dominant behavior, the Eqs. (3.1), (3.2), (3.3) and (3.4) are used presented in Table 4.9. The calculations for the capacities of the piers are presented in the table. Based on the analysis from the parametric study presented in Chapter 3, Eq. (3.2) of (Turnšek & Čačovič, 1971) has the best fit for representing the capacity with better indices for the aspect ratio and vertical stress, in addition to fair values for the vertical stress and full scale.

Table 4.9: Capacity formulations for shear dominant behavior

Formulation	Source	Pier1 V_{\max} (kN)	Pier 2 V_{\max} (kN)
$V_{m,1} = (f_v b_w L_w + 0.25N)\gamma_g$	Clause 7.10.1.1. (CSA S304.1-04, R2010)	204.6	239.1
$V_{m,2} = \frac{f_t L_w b_w}{\xi} \sqrt{1 + \frac{\sigma_o}{f_t}}$	(Turnšek & Čačovič, 1971)	163.3	182.6
$V_{m,3} = \frac{c + \mu_s \sigma_o}{1 + \alpha_p} (L_w b_w)$	Coulomb Criterion corrected by (Magenes & Calvi, 1997b)	180.7	161.4
$V_{m,4} = P \tan \phi \left[1 - \frac{h}{2L_w} \tan \phi \left(\frac{1}{1-v} \right) \right]$	(Lourenço et al., 2005)	69.2	62.2

Therefore, $V_{\max} = 119.8\text{kN}$ and $V_{\max} = 146.1\text{kN}$ will be used in the model for Pier1 and Pier2, respectively. To build the model in OpenSees, we present the summary of all the calculated parameters to be used for both the shear and flexural dominant behaviors in Table 4.10. The value of $V' = 0.9V_{\max}$ and $V_{\text{ult}} = 0.5V_{\max}$ based on the calibration in Chapter 3.

Table 4.10: Parameters needed to build the distributed plastic model in OpenSees

Sample	fm	ft	L (m)	H (m)	t (m)	V' (kN)	V_{\max} (kN)	V_{ult} (kN)	N (kN)
Pier1	6.75	0.137	1.62	1.97	0.5	107.8	163.3	59.9	180
Pier2	6.75	0.137	1.62	3.48	0.43	131.5	182.6	73.1	405

The aspect ratio of Pier1 is $H/L = 1.22$ which predicts a shear dominant behavior. This was evident from the cyclic behavior in Fig. 4.25 showing a wide area under the curve due to energy dissipation. The shear capacity of the pier in the $V_{\max}=161\text{kN}$ at 3.25mm and an ultimate capacity of 84.5kN at 10.25mm. Thus, the displacement ductility factor is $\mu = 3.15$. The elastic shear capacity is reached at 1.5 mm with 149 kN.

On the other hand, the aspect ratio of **Pier 2** is $H/L = 2.15$ which predicts a flexural dominant behavior. Evident in Fig. 4.26 is the narrow shape of the curve indicating low energy dissipation due to more flexibility in the slender pier. The maximum shear capacity is $V_{\max}=183$ kN with a plateau in the curve showing at about 7.5mm. The reason the capacity of the pier with flexural dominant behavior is higher than the one with shear dominant behavior is due to the high vertical

forces on Pier 2 associated with its location on the first floor thus carrying more loads. Also, it was noticed a decrease in the stiffness as the lateral deformation reached 3.25mm and the shear is 139kN.

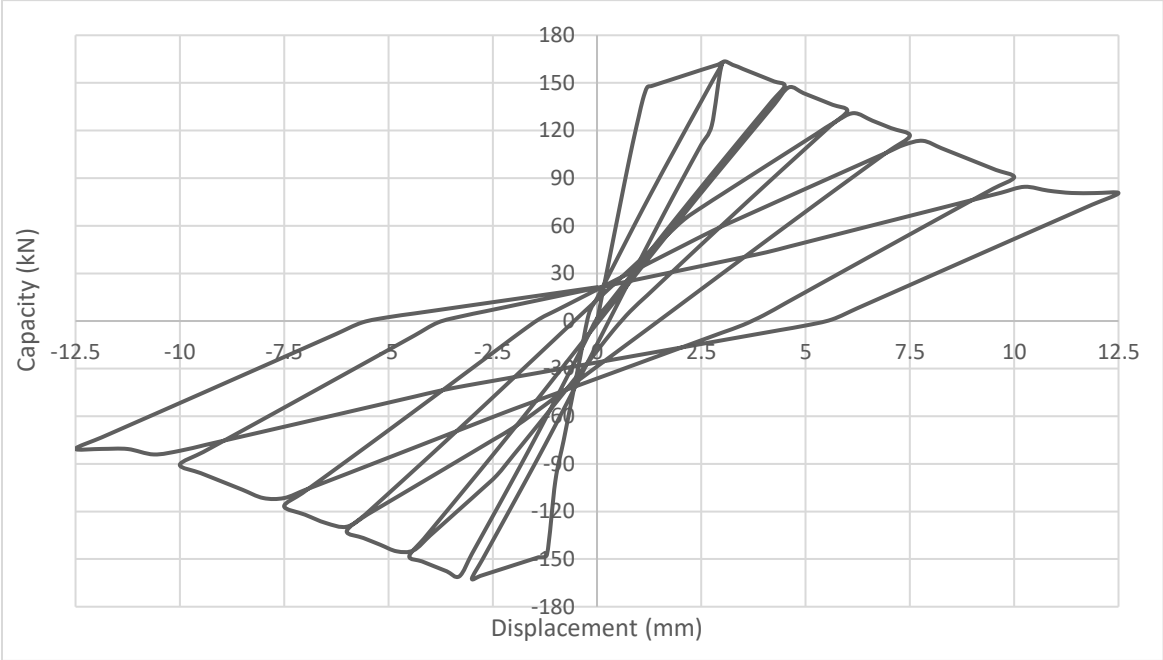


Figure 4.25: The cyclic behavior of Pier 1

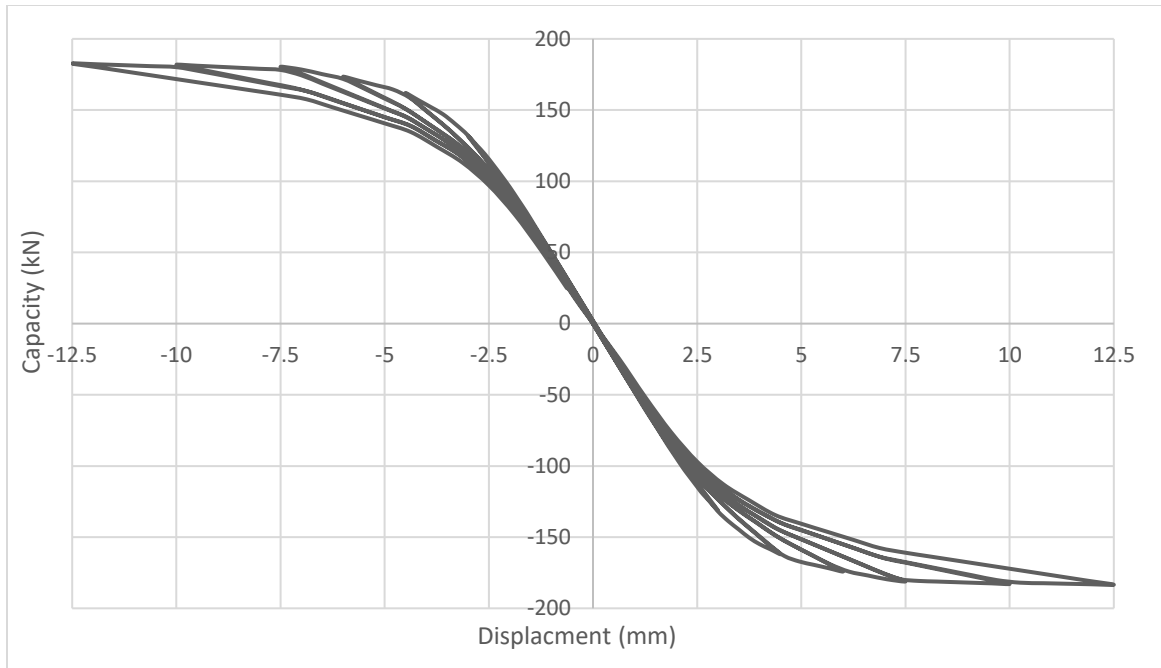


Figure 4.26: The cyclic behavior of Pier2

In Summary, the deterministic equivalent frame model calibrated using experimental data is used to generate data between curtailed ranges. The ranges are based on the common practice and limited dimensions of the structural elements. Using linear data analysis tools such as statistical correlation values and slopes, a preliminary relationship between the characteristics of the walls and their influence on the behavior is built. Those factors are the first step for more comprehensive nonlinear data analysis presented in the next chapter.

Chapter 5: Nonlinear Probabilistic Model and Machine Learning Approach to Parameter Identification for URM Piers Strengthening

The performance of URM piers is reliable on many parameters that can influence its strength and deformation. In the previous chapter, a linear correlation method was used to assess the effect of those parameters. However, in this chapter, a more advance technique is used which can measure the nonlinear relationship between the parameters. The work includes both dominant modes of failure: the shear and flexure. Using the deterministic model developed before to generate data of all the parameters includes the target variables, it was possible to develop a probability-based model using Bayesian networks (A. Goulet, 2020) which can assess the flow of information. Utilizing a software named BayesiaLab (Conrady & Jouffe, 2015), it is possible to import the data files and discretize the variables using several available methods, then learn the connections using supervised machine learning algorithms. Those models are validated using a cross validation method that provides the precision and the reliability of the connections. Finally, several indices are produced that shows the influence of predictive variables on the strength and ductility of the piers which will play a major role in any strengthening intervention applied on URM walls.

5.1 Data generation and curation

Using the calibrated deterministic model in Chapter 3, a random data was generated for the both the shear and flexure dominated behaviors of the piers. However, the difference in this time is the randomization of the all the variables available in the model that can influence response within limited ranges that will yield the sought modes of failure. Herein, 513 observations for 10 variables are used for the shear dominant mode of failure with the shear strength, maximum displacement, and the ultimate displacement, as the three target variables in the model. In addition, data on ductility is generated using the ratios between displacement values relevant to each data point

which could be helpful to understand the response of the piers from different perspective. The 896 observations for 8 variables are generated for the flexure dominant mode of failure with the shear strength representing the target variable of the model. Figures 5.1a, 5.1b, and 5.1c show the data distribution of the target variable V_{\max} for the shear dominant behavior. This normal distribution will help in the discretization process to determine the intervals required for better analyzing the information in the model. Figures 5.1d, 5.1e, and 5.1f show the data distribution for the target variable V_{\max} for the flexural dominant behavior with normal distribution. It is noted that the data has been generated and edited to fit the normal distribution curve as it serves a mark for random selection of data and thus eliminates any bias in the analysis. A manual discretization of the target variable is made to set the place of other predictive variables to be discretized using the automated functions explained in the previous sections.

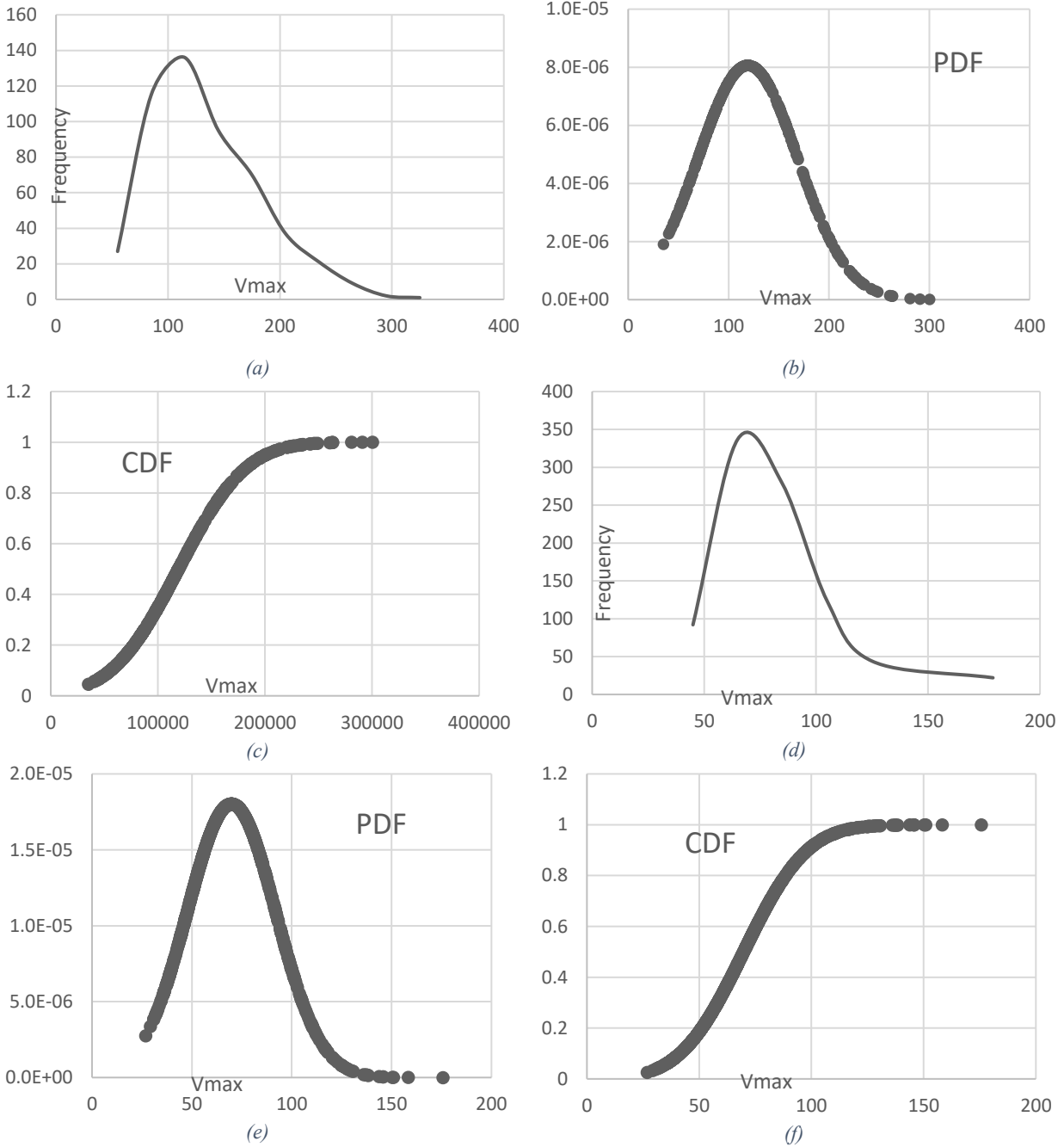


Figure 5.1: a) Frequency of V_{max} in terms of specified intervals b) PDF of V_{max} c) CDF of V_{max} d) Frequency of V_{max} for the specified intervals e) PDF of V_{max} f) CDF of V_{max} .

The list of the predictive and the target variables generated are listed in Tables 5.1 and 5.2 for the shear and the flexural dominant mode of behavior, respectively. The aspect ratio H/L and the ductility factor μ (D_{ult}/D_{max}) are only ratios extracted from the data and was not generated by the model originally. After the data has been curated, it is imported to the BayesiaLab Software for

the analysis. It is to be noted that μ (D_{ult}/D_{max}) is a ratio that expresses ductility particularly for the purpose of this work. The aim is to combine the maximum and the ultimate displacement information to form a relationship showing the behavior of the piers. Therefore, ductility can be defined differently in other work where more factors such as the stress can be included.

Table 5.1: Generated variables for the shear dominant behavior

Predictive Variables								Target Variables			
N	fm	ft	Et	L	t	H	H/L	Vmax	Dmax	Dult	μ (D_{ult}/D_{max})

Table 5.2: Generated variables for the flexural dominant behavior

Predictive Variables								Target Variable
N	fm	ft	Et	L	t	H	H/L	Vmax

Figures 5.2a, 5.2b, and 5.2c shows the scatter data points for the most relevant predictive variables N, t, and ft versus the target variable V_{max} for the shear dominant behavior. Figures 5.2d and 5.2e are the scatter data points for the N and H/L predictive variables versus the target variable V_{max} for the flexural dominant behavior. The reason the data points are presented is to understand their relationship to the mutual information that will be generated later using the probabilistic model. For the typical correlation in regression, the shape of the data can predict the level of correlation. As the scattering leans towards a circular shape it will predict low levels of correlation. It will be observed that nonlinear correlations can capture a different level of relationship between the data without having to depend on the linearity of the distribution.

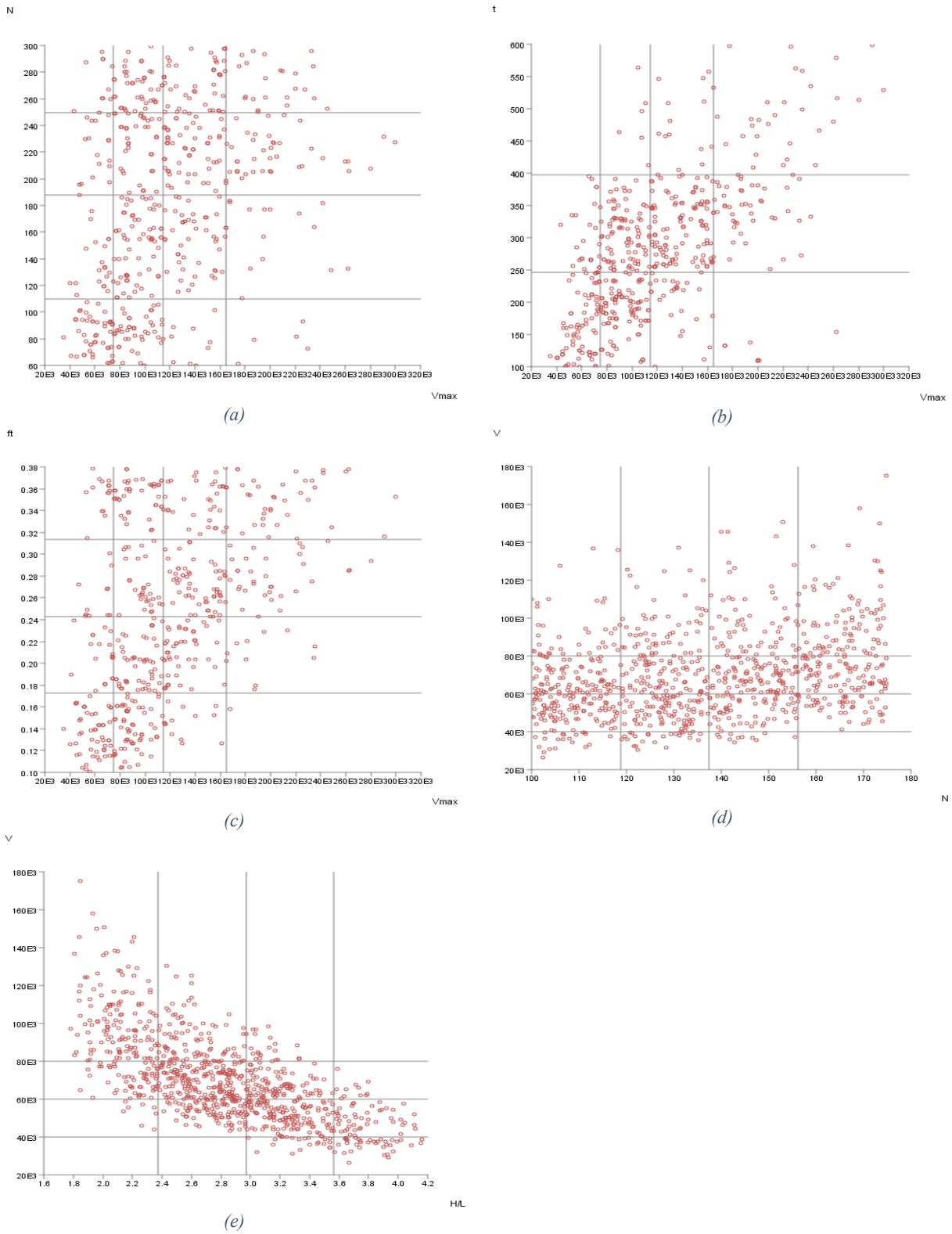


Figure 5.2: a) Data scatter for V_{max} versus N for the shear dominant behavior b) vs t for the shear dominant behavior c) vs ft for the shear dominant behavior d) vs N for the flexural dominant behavior e) vs H/L for the flexural dominant behavior

5.2 Nonlinear Probability Model and Acyclic Graphs

An application of the probabilistic model is done in the BayesiaLab Software to perform a nonlinear analysis of the data generated by the calibrated deterministic model. After the curation of the data and distinguishing the input variables from the output variables, it is then possible to import the files into the software and start the discretization process. The work will be divided between the shear and the flexural dominant behaviors witnessed in the piers.

5.2.1 Model of the Shear dominant Behavior in Piers

After applying several trials of discretization methods on the data set, the most optimized intervals were selected for the analysis based on the modal validation and tuning of the numbers to enhance the performance. A summary of the intervals selected for each of the variables are presented in the report in Fig. 5.3.

Nodes 10					
		States	Intervals		Discretization
Vmax	Continuous	<=75000	35230.0	75000.0	Asked: Manual Obtained: Manual
		<=115000	75000.0	115000.0	
		<=165000	115000.0	165000.0	
		>165000	165000.0	300300.0	
N	Continuous	<=110	60.317	110.0	Asked: Manual Obtained: Manual
		<=188	110.0	188.0	
		<=250	188.0	250.0	
		>250	250.0	299.875	
fm	Continuous	<=3	2.5	3.0	Asked: Manual Obtained: Manual
		<=3.7	3.0	3.7	
		<=4.2	3.7	4.2	
		>4.2	4.2	4.7	
ft	Continuous	<=0.173	0.101153	0.173	Asked: Manual Obtained: Manual
		<=0.243	0.173	0.243	
		<=0.314	0.243	0.314	
		>0.314	0.314	0.379537	
Et	Continuous	<=2	1.00069	2.0002533333333333	Asked: Normalized Equal Distance - 3 Obtained: Normalized Equal Distance - 3
		<=3	2.0002533333333333	2.9998166666666667	
		>3	2.9998166666666667	3.99938	
L	Continuous	<=1097.828	900.407	1097.828	Asked: Normalized Equal Distance - 3 Obtained: Normalized Equal Distance - 3
		<=1295.249	1097.828	1295.249	
		>1295.249	1295.249	1492.67	
t	Continuous	<=266.539	100.243	266.539	Asked: Normalized Equal Distance - 3 Obtained: Normalized Equal Distance - 3
		<=432.835	266.539	432.835	
		>432.835	432.835	599.131	
H	Continuous	<=0.85	0.500359	0.85	Asked: Manual Obtained: Manual
		<=1.2	0.85	1.2	
		>1.2	1.2	1.54976	
H/L	Continuous	<=0.7	0.392664211	0.7	Asked: Manual Obtained: Manual
		<=1.2	0.7	1.2	
		>1.2	1.2	1.613742201	
μ (Dult/Dmax)	Continuous	<=2.782	1.672566372	2.7817109146666663	Asked: Normalized Equal Distance - 3 Obtained: Normalized Equal Distance - 3
		<=3.891	2.7817109146666663	3.8908554573333333	
		>3.891	3.8908554573333333	5.0	

Figure 5.3: Discretization of the variables and the different functions used.

In the first trail, the Naïve Bayes network is used to have a general idea on the influence of all the predictive variables on the target variable V_{\max} . Figure 5.4 shows the connections and the mutual information for all the variables. The values in blue represent the percentages of reduction of entropy of the target variable on the predictive variables while the red values are the opposite. This

value is simply obtained by dividing the mutual information by the marginal entropy of the variable. In other words, those values determine how much information we can know about target variable by revealing the predictive variables. Thus, we are interested in the red values that are aligned in increasing order reflected in the increased thickness of the arrows. The least influence seems to be the compressive strength of the pier fm with mutual information $I = 0.0073$ and 0.3789% entropy reduction on V_{max} . On the other end, the thickness t has the highest influence on V_{max} with $I = 0.2184$ and entropy reduction of 11.2376%. In Fig. 5.5a is shown the application of the Markov Blanket algorithm, which selects only the most influential variables t , ft , N , and L with slight increase in the mutual information compared to the Naïve Bayes Network. Figure 5.5b is the model constructed using the Augmented Markov Blanket Algorithm. This resulted in considering one less variable limiting the predictive variables to t , ft , and N with slight improvement in the mutual information for the variable t and slight reduction in the mutual information for ft and N .

Additional computational effort is applied to enhance the performance of the models using the Structural Coefficient SC (Richardson, 1968). This parameter is a tool that permits to change the internal number of observations made from the model in a way that affects the complexity associated with the connection drawn between the variables. The internal number of observations is defined as $N' = N / SC$ where N is the original number of observations from the imported data file, thus changing the value of SC between the range (0;1), leads to increase in the number of internal observations and thus the complexity of the structure. However, this increase in complexity may come at the expense of the precision due to overfitting of the model to the data. Figures 5.5c and 5.5d show the graph for SC versus the normalized values of the

structure/target precision ratios for both Markov Blanket and Augmented Markov Blanket models. The structure refers to the complexity of the model which increases as the SC increases. The target precision however keeps increasing up to a certain limit where we observe a spike in the graph. At this point, the increase in the structure exceeds the increase in the precision indicating the inadequacy of the data past this SC. Relying on this information, for the Markov Blanket model an $SC = 0.22$ is selected and for the Augmented Markov Blanket an $SC = 0.175$ is selected. Figures 5.5e and 5.5f shows the models after the alteration of the SC to the new values extracted from the graphs.

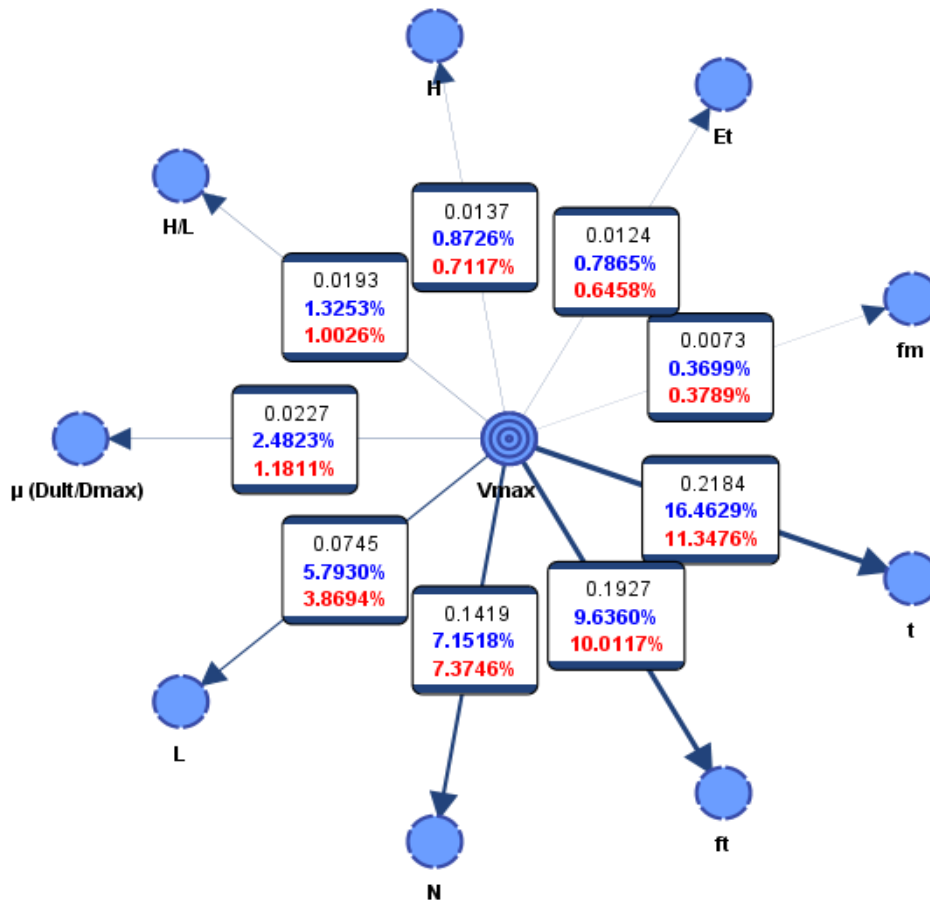


Figure 5.4: Model using Naive Bayes Network with the mutual information.

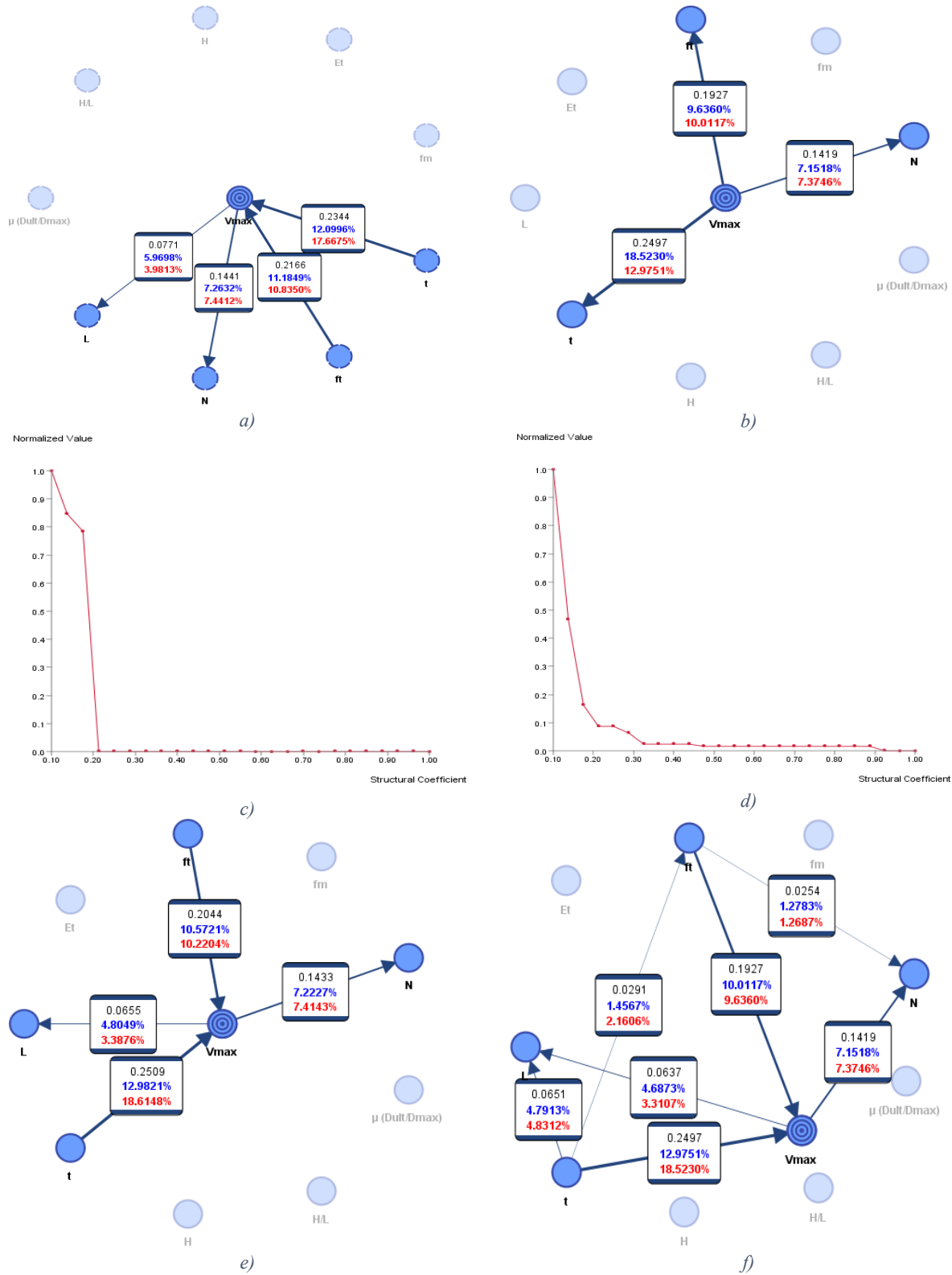


Figure 5.5: a) Markov Blanket b) Aug. Markov Blanket c) SC vs structure/target precision ratio for the Markov Blanket d) SC vs structure/target precision ratio for the Aug. Markov Blanket model e) Markov Blanket with SC=0.22 f) Aug. Markov Blanket with SC=0.175

Only a slight change in the values of the mutual information is observed in the Markov Blanket model. For the Augmented Markov Blanket model additional connections between the predictive variables appeared between t and L , t and ft , and finally between ft and N . Those additional arrows can justify the connectivity between those variables and the influence on each other as extracted from the data set. This in fact reflects the realistic approach in determining the values of the predictive variables against the fixity applied on the all the variables while changing only one in the linear analysis of the data performed in the previous chapter. It is an expected reduction in connective arrows in the Markov and Augmented Markov Blanket compared to the Naïve Bayes Network due to their tendencies to limit the nodes to direct connections. However, the validity of the model is yet to be tested to understand which model is more reliable and assess the degree of precision in each.

The model validation is done through the K-Folds Cross Validation method (Rodriguez et al., 2010) that incorporates a K number of test samples from the original data and utilize it in the purpose of learning the networks. The results from all the learned networks are then combined to give the final validation of the model in terms of reliability and precision percentages. The advantage of K-Fold is the shuffling of the selected test samples which eliminates any bias and randomize the data. For this model, K = 10 samples are chosen with a test sample with size of 51 observations leaving the 462 observations for the learning sample. Figures 5.6a, 5.6b, and 5.6c show the performance of the generated models from the Naïve Bayes Network, Markov Blanket, and Augmented Markov Blanket, respectively. The first row represents the actual values extracted from the data file imported to the software while the first column represents the predicted values by the model after the aggregation of the results from the 10 folds test samples. The occurrences are then represented in the middle of the table. Dividing the occurrences by the actual values yields

the precision percentages, while dividing the occurrences by the prediction values yields the reliability percentages.

Occurrences				
Value	<=75000 (96)	<=115000 (182)	<=165000 (154)	>165000 (81)
<=75000 (64)	42	19	2	1
<=115000 (218)	41	126	45	6
<=165000 (184)	13	37	99	35
>165000 (47)	0	0	8	39

Reliability				
Value	<=75000 (96)	<=115000 (182)	<=165000 (154)	>165000 (81)
<=75000 (64)	65.6250%	29.6875%	3.1250%	1.5625%
<=115000 (218)	18.8073%	57.7982%	20.6422%	2.7523%
<=165000 (184)	7.0652%	20.1087%	53.8043%	19.0217%
>165000 (47)	0.0000%	0.0000%	17.0213%	82.9787%

Precision				
Value	<=75000 (96)	<=115000 (182)	<=165000 (154)	>165000 (81)
<=75000 (64)	43.7500%	10.4396%	1.2987%	1.2346%
<=115000 (218)	42.7083%	69.2308%	29.2208%	7.4074%
<=165000 (184)	13.5417%	20.3297%	64.2857%	43.2099%
>165000 (47)	0.0000%	0.0000%	5.1948%	48.1481%

a)

Occurrences				
Value	<=75000 (96)	<=115000 (182)	<=165000 (154)	>165000 (81)
<=75000 (74)	50	22	2	0
<=115000 (206)	36	128	37	5
<=165000 (187)	10	32	108	37
>165000 (46)	0	0	7	39

Reliability				
Value	<=75000 (96)	<=115000 (182)	<=165000 (154)	>165000 (81)
<=75000 (74)	67.5676%	29.7297%	2.7027%	0.0000%
<=115000 (206)	17.4757%	62.1359%	17.9612%	2.4272%
<=165000 (187)	5.3476%	17.1123%	57.7540%	19.7861%
>165000 (46)	0.0000%	0.0000%	15.2174%	84.7826%

Precision				
Value	<=75000 (96)	<=115000 (182)	<=165000 (154)	>165000 (81)
<=75000 (74)	52.0833%	12.0879%	1.2987%	0.0000%
<=115000 (206)	37.5000%	70.3297%	24.0260%	6.1728%
<=165000 (187)	10.4167%	17.5824%	70.1299%	45.6790%
>165000 (46)	0.0000%	0.0000%	4.5455%	48.1481%

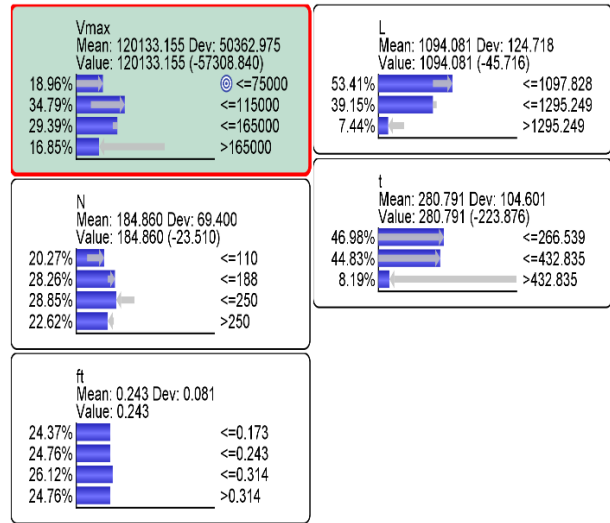
b)

Occurrences				
Value	<=75000 (96)	<=115000 (182)	<=165000 (154)	>165000 (81)
<=75000 (67)	45	20	2	0
<=115000 (217)	41	133	36	7
<=165000 (185)	9	29	104	43
>165000 (44)	1	0	12	31

Reliability				
Value	<=75000 (96)	<=115000 (182)	<=165000 (154)	>165000 (81)
<=75000 (67)	67.1642%	29.8507%	2.9851%	0.0000%
<=115000 (217)	18.8940%	61.2903%	16.5899%	3.2258%
<=165000 (185)	4.8649%	15.6757%	56.2162%	23.2432%
>165000 (44)	2.2727%	0.0000%	27.2727%	70.4545%

Precision				
Value	<=75000 (96)	<=115000 (182)	<=165000 (154)	>165000 (81)
<=75000 (67)	46.8750%	10.9890%	1.2987%	0.0000%
<=115000 (217)	42.7083%	73.0769%	23.3766%	8.6420%
<=165000 (185)	9.3750%	15.9341%	67.5325%	53.0864%
>165000 (44)	1.0417%	0.0000%	7.7922%	38.2716%

c)



d)

Figure 5.6: a) Performance of Naive Bayes model b) Markov Blanket c) Aug. Markov Blanket d) Marginal probabilities for the variables in the Markov Blanket

Observing the values for the three models, the Markov Blanket in Figure 5.5e provides the best precision values. Also, it performs better across all the intervals regarding the reliability meter.

Since the complexity of the Augmented Markov Blanket model did not improve the performance

of the model, it will be discarded. Figure 5.6d shows the marginal probabilities of all the variables in the Markov Blanket in addition to the target variable V_{\max} . This reflects the distribution of the intervals amongst the variables at any moment given the data provided. This can be used to predict the performance of the piers from a general perspective, which can then be narrowed down to more specific values as we our information about the parameters increases. As the values from the Markov Blanket model are considered in the analysis, the variables with the most influence on the strength of the pier are the thickness t and the tensile strength f_t with mutual information values $I = 0.25$ and $I = 0.2$, respectively.

Now we shift the target variable to the ductility factor $\mu = D_{ult}/D_{max}$ to study the response of the piers in the perspective of lateral displacements. D_{ult} is the ultimate displacement at failure, while D_{max} is the displacement at the maximum base shear strength achieved extracted form the response curves of the cyclic behavior of the piers. The data scatter points between ductility factor and the height H and the length L of the piers is shown in Figs 5.7a and 5.7b, respectively.

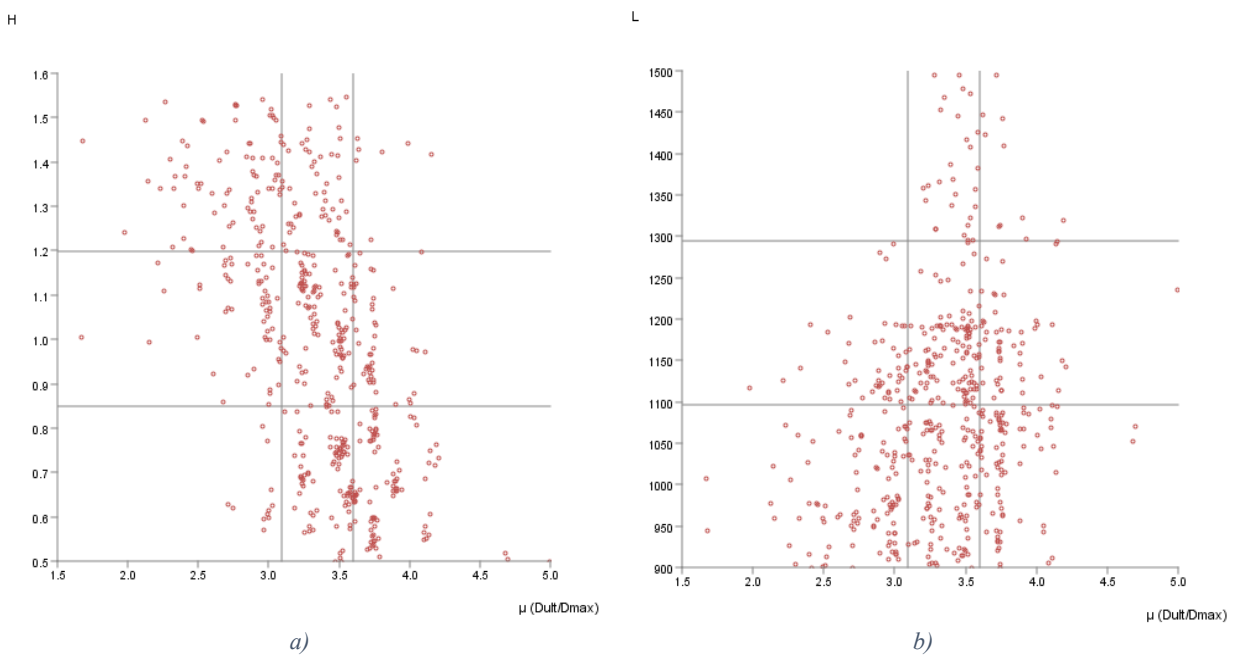


Figure 5.7: a) Scatter points for ductility factor and H b) ductility factor and L

Similarly, the discretization criteria are selected, and the acyclic graph is generated. The model is then learned through the Naïve Bayes Network, the Markov Blanket, and the Augmented Markov Blanket algorithms using a structural coefficient $SC = 0.27667$ extracted from the structure/target precision ratio graphs. The manual discretization of the target variable and the SC for the Markov Blanket are shown in Figs. 5.8a and 5.8b, respectively.

The best performance is attributed to the Markov Blanket model based on a 10 Folds Cross Validation method using 10 testing samples aggregating into precision and reliability percentages. The model presented a connection between the ductility factor and the predictive variables, the height H , the length L , and the tensile strength f_t with mutual information values $I = 0.187$, $I = 0.0602$, and $I = 0.0306$, respectively. The results are shown in Fig. 5.9a representing the acyclic graph. In Fig. 5.9b, the performance analysis criteria are presented. In comparison to the model for the shear strength capacity, the values for reliability and precision are generally lower indicating a weak connection between the predictive variables and the target variable.

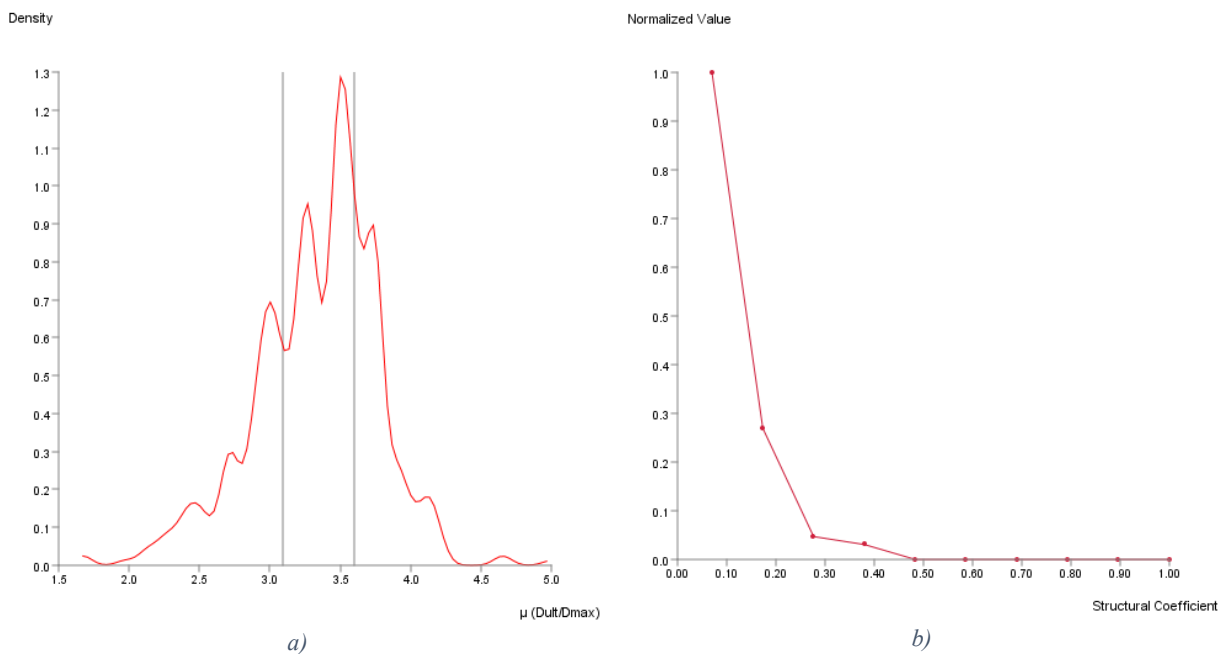


Figure 5.8: Manual discretization of the ductility factor using the PDF a) SC for Markov Blanket vs structure/target precision.

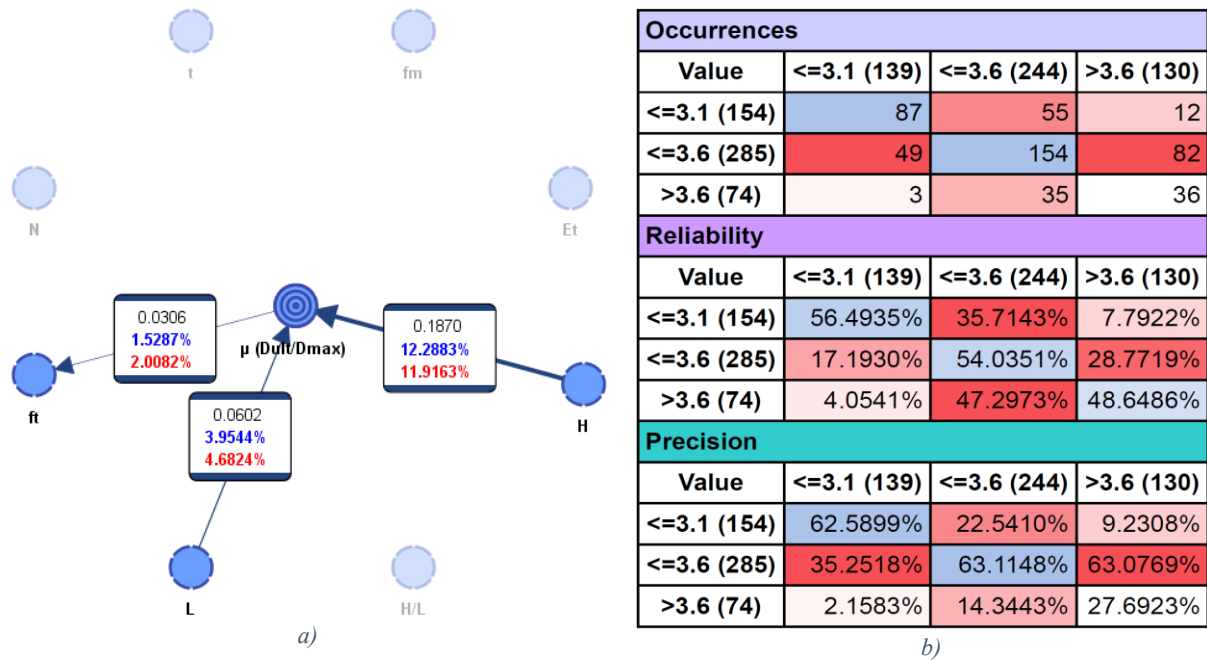


Figure 5.9: Acyclic graph for the Markov Blanket model b) Performance of the Markov Blanket model

5.2.2 Model of the Flexural dominant Behavior in Piers

Like the first analysis, the flexural dominant behavior of the piers is also analyzed with the target variable as the maximum shear strength V_{max} . The optimum discretization is shown in Fig. 5.10 including nine nodes. Then, V_{max} is discretized manually while the rest of the variables are discretized using the normalized equal distance function.

Nodes 9					
		States	Intervals	Discretization	
N	Continuous	<=118.802	100.099	118.80225	Asked: Normalized Equal Distance - 4 Obtained: Normalized Equal Distance - 4
		<=137.506	118.80225	137.5055	
		<=156.209	137.5055	156.20875	
		>156.209	156.20875	174.912	
fm	Continuous	<=3.054	2.50592	3.0542625	Asked: Normalized Equal Distance - 4 Obtained: Normalized Equal Distance - 4
		<=3.603	3.0542625	3.602605	
		<=4.151	3.602605	4.1509475	
		>4.151	4.1509475	4.69929	
ft	Continuous	<=0.17	0.100111	0.17006075	Asked: Normalized Equal Distance - 4 Obtained: Normalized Equal Distance - 4
		<=0.24	0.17006075	0.24001050000000002	
		<=0.31	0.24001050000000002	0.30996025000000005	
		>0.31	0.30996025000000005	0.37991	
Et	Continuous	<=1.749	1.00069	1.7493375000000002	Asked: Normalized Equal Distance - 4 Obtained: Normalized Equal Distance - 4
		<=2.498	1.7493375000000002	2.4979850000000003	
		<=3.247	2.4979850000000003	3.2466325000000005	
		>3.247	3.2466325000000005	3.99528	
L	Continuous	<=775.068	700.098	775.06825	Asked: Normalized Equal Distance - 4 Obtained: Normalized Equal Distance - 4
		<=850.038	775.06825	850.0385	
		<=925.009	850.0385	925.00875	
		>925.009	925.00875	999.979	
t	Continuous	<=425.025	300.076	425.025	Asked: Normalized Equal Distance - 4 Obtained: Normalized Equal Distance - 4
		<=549.974	425.025	549.9739999999999	
		<=674.923	549.9739999999999	674.923	
		>674.923	674.923	799.872	
H	Continuous	<=2.063	1.75136	2.0633850000000002	Asked: Normalized Equal Distance - 4 Obtained: Normalized Equal Distance - 4
		<=2.375	2.0633850000000002	2.37541	
		<=2.687	2.37541	2.687435	
		>2.687	2.687435	2.99946	
V	Continuous	<=40000	26882.3	40000.0	Asked: Manual Obtained: Manual
		<=60000	40000.0	60000.0	
		<=80000	60000.0	80000.0	
		>80000	80000.0	175700.0	
H/L	Continuous	<=2.376	1.780465602	2.37622751875	Asked: Normalized Equal Distance - 4 Obtained: Normalized Equal Distance - 4
		<=2.972	2.37622751875	2.9719894355	
		<=3.568	2.9719894355	3.56775135225	
		>3.568	3.56775135225	4.163513269	

Figure 5.10: Discretization of the variables for the flexural dominant behavior of the piers

The Naïve Bayes network in Fig. 5.11 is generated to have an overlook on the connections and their strength with the target variable V_{max} . The height of the pier has the highest influence with mutual information $I = 0.3779$ giving a 20.87% reduction of entropy to the target variable. The

elastic tensile modulus has the least influence with $I = 0.0049$ and only 0.27% reduction of entropy on the target variable. Figures 5.12a and 5.12b shows the Markov Blanket models with $SC = 1$ and $SC = 0.2125$, respectively. The aspect ratio H/L , the tensile strength ft , the thickness t , and the vertical forces N , are selected by the model. However, with the increase in the internal number of observations, the length L is added to the model. There is not a major change in the mutual information compared to the Naïve Bayes network.

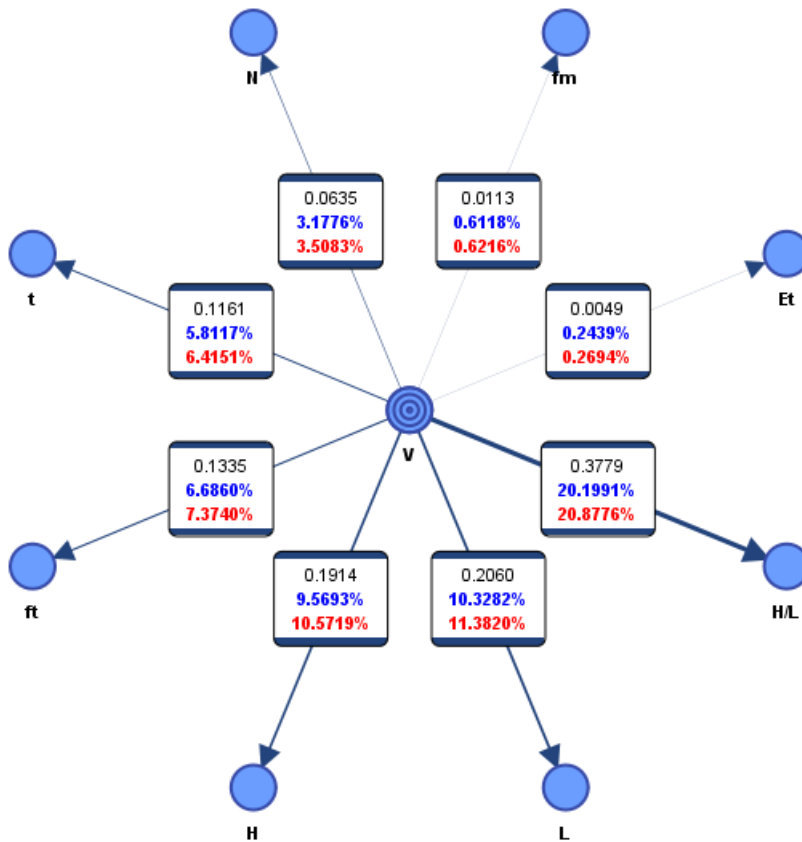


Figure 5.11: Naive Bayes Network

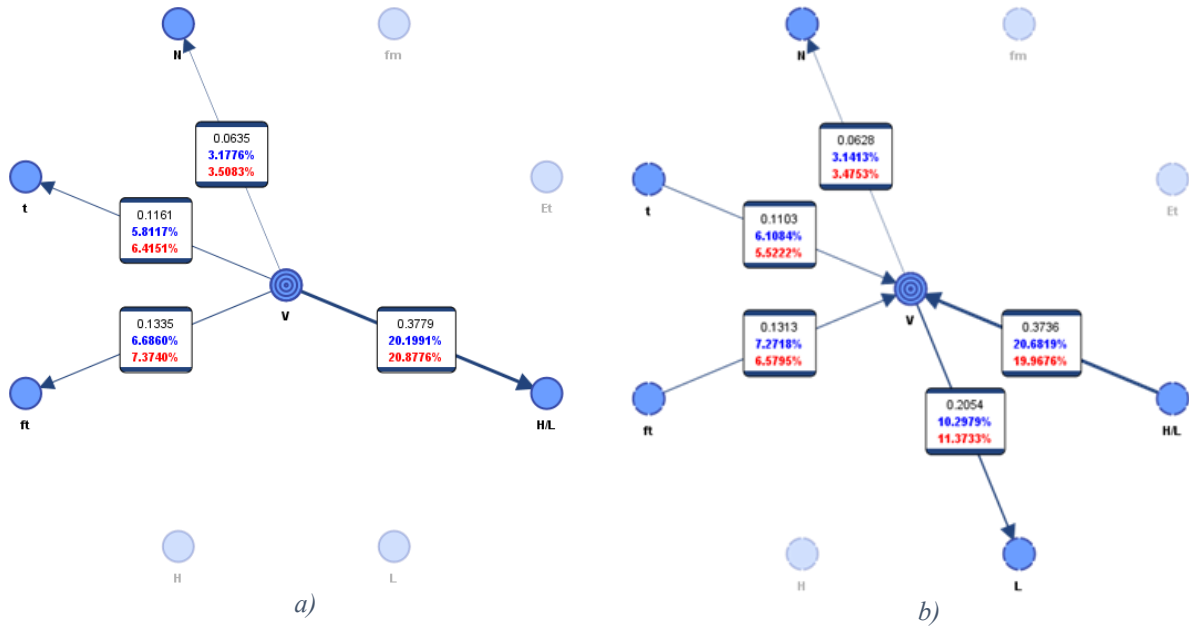


Figure 5.12: a) Markov Blanket model b) Markov Blanket model with $SC=0.2125$

Figures 5.13a and 5.13b shows the Augmented Markov Blanket models with $SC = 1$ and $SC = 0.24$, respectively. With the increase in the internal number of observations, the complexity of the model increased adding connections to between the predictive and the target variable, in addition to the connections between the predictive variables themselves. When we compare the results to the original model, there is no major change in the mutual information. The structural coefficients extracted using the structure/target precision graphs are shown in Figs. 5.14a and 5.14b for the Markov Blanket and the Augmented Markov Blanket, respectively.

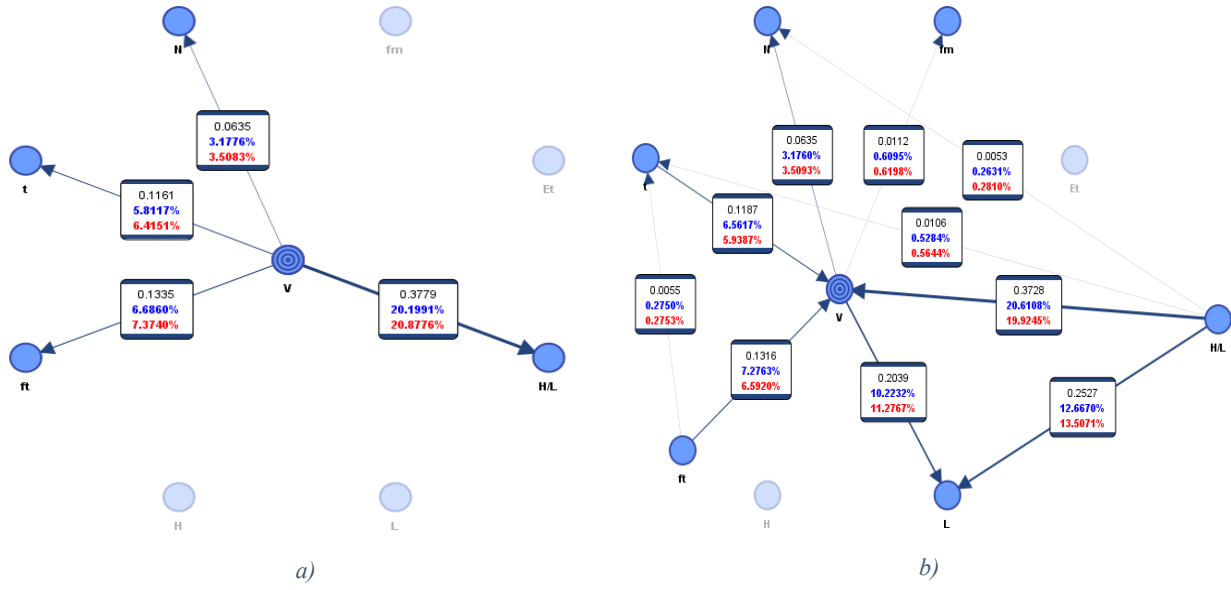


Figure 5.13: a) Augmented Markov Blanket model b) Augmented Markov Blanket model with SC = 0.24

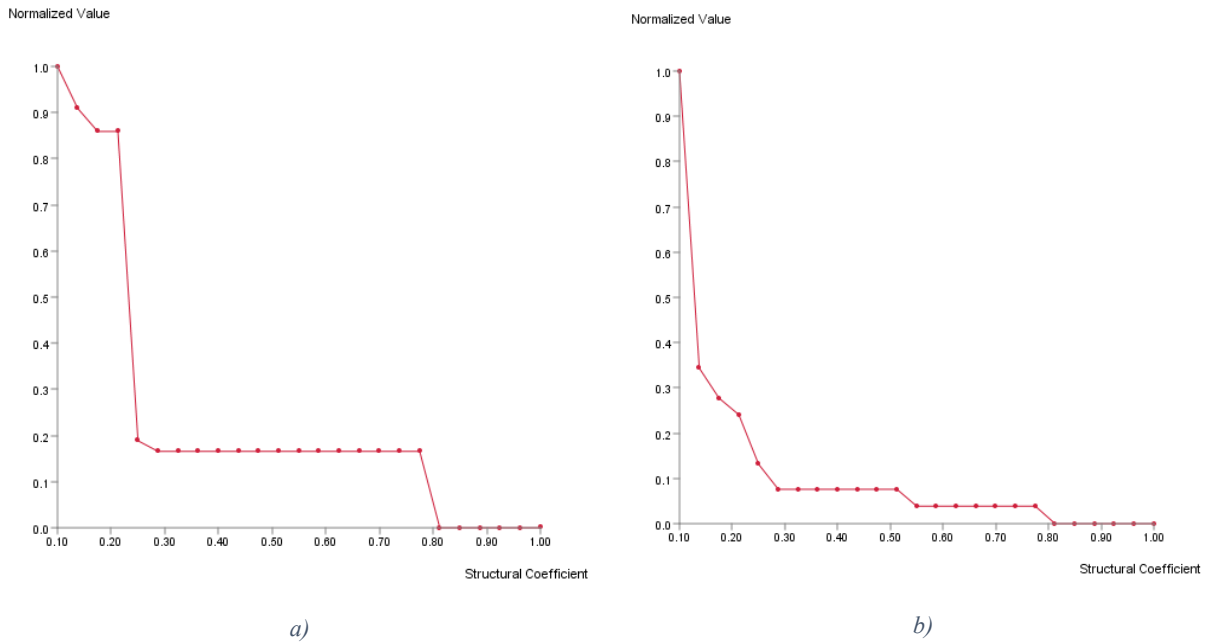


Figure 5.14: a) SC for the Markov Blanket model b) SC for the Aug. Markov Blanket model.

The performance of the models is measured using a 10 Folds cross validation method with 10 testing samples where the aggregated results are presented in Figs. 5.15a, 5.15b and 5.15c for the Naïve Bayes network, Markov Blanket, and the Augmented Markov Blanket models, respectively. Reading the reliability and the precision percentages, the enhanced Augmented Markov Blanket

model performed the best with overall precision of 75.3% and overall reliability of 75.8%. Figure 15.d shows the marginal probabilities of the main variables in the model presenting a general observation of probability distribution using the provided data set. Using the acyclic graph in Fig. 5.41, we can deduce that the best two predictors for the base shear capacity of the piers in the flexural dominant behavior are the aspect ratio, H/L , and the length of the pier, L , with mutual information $I = 0.3728$ and $I = 0.2039$, respectively. The H/L and L are connected at a mutual information $I = 0.2527$ which should be an obvious connection since the length L is part of the aspect ratio. The next two influencing predictors on the strength of the piers are the tensile strength, f_t , and the thickness of the pier, t , with $I = 0.1316$ and $I = 0.1187$, respectively. The f_t and t are connected at a mutual information $I = 0.0055$ which does not constitute a major influence between the variables.

Occurrences				
Value	<=40000 (54)	<=60000 (276)	<=80000 (320)	>80000 (246)
<=40000 (41)	31	10	0	0
<=60000 (274)	23	182	65	4
<=80000 (359)	0	83	209	67
>80000 (222)	0	1	46	175
Reliability				
Value	<=40000 (54)	<=60000 (276)	<=80000 (320)	>80000 (246)
<=40000 (41)	75.6098%	24.3902%	0.0000%	0.0000%
<=60000 (274)	8.3942%	66.4234%	23.7226%	1.4599%
<=80000 (359)	0.0000%	23.1198%	58.2173%	18.6630%
>80000 (222)	0.0000%	0.4505%	20.7207%	78.8288%
Precision				
Value	<=40000 (54)	<=60000 (276)	<=80000 (320)	>80000 (246)
<=40000 (41)	57.4074%	3.6232%	0.0000%	0.0000%
<=60000 (274)	42.5926%	65.9420%	20.3125%	1.6260%
<=80000 (359)	0.0000%	30.0725%	65.3125%	27.2358%
>80000 (222)	0.0000%	0.3623%	14.3750%	71.1382%

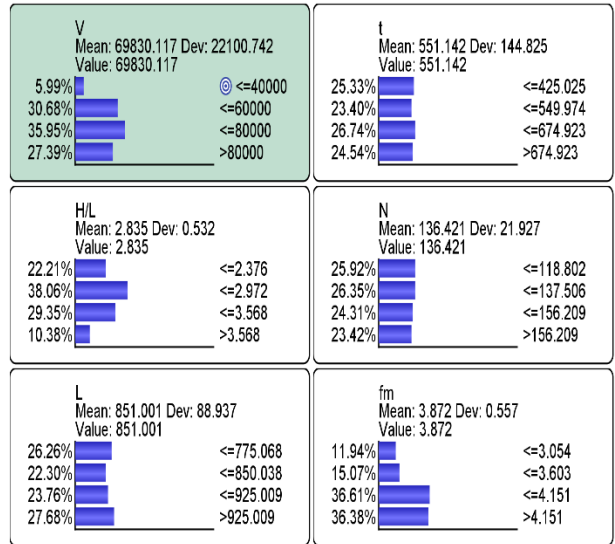
a)

Occurrences				
Value	<=40000 (54)	<=60000 (276)	<=80000 (320)	>80000 (246)
<=40000 (43)	33	10	0	0
<=60000 (273)	21	202	50	0
<=80000 (362)	0	63	243	56
>80000 (218)	0	1	27	190
Reliability				
Value	<=40000 (54)	<=60000 (276)	<=80000 (320)	>80000 (246)
<=40000 (43)	76.7442%	23.2558%	0.0000%	0.0000%
<=60000 (273)	7.6923%	73.9927%	18.3150%	0.0000%
<=80000 (362)	0.0000%	17.4033%	67.1271%	15.4696%
>80000 (218)	0.0000%	0.4587%	12.3853%	87.1560%
Precision				
Value	<=40000 (54)	<=60000 (276)	<=80000 (320)	>80000 (246)
<=40000 (43)	61.1111%	3.6232%	0.0000%	0.0000%
<=60000 (273)	38.8889%	73.1884%	15.6250%	0.0000%
<=80000 (362)	0.0000%	22.8261%	75.9375%	22.7642%
>80000 (218)	0.0000%	0.3623%	8.4375%	77.2358%

b)

Occurrences				
Value	<=40000 (54)	<=60000 (276)	<=80000 (320)	>80000 (246)
<=40000 (44)	34	10	0	0
<=60000 (267)	20	202	45	0
<=80000 (356)	0	63	243	50
>80000 (229)	0	1	32	196
Reliability				
Value	<=40000 (54)	<=60000 (276)	<=80000 (320)	>80000 (246)
<=40000 (44)	77.2727%	22.7273%	0.0000%	0.0000%
<=60000 (267)	7.4906%	75.6554%	16.8539%	0.0000%
<=80000 (356)	0.0000%	17.6966%	68.2584%	14.0449%
>80000 (229)	0.0000%	0.4367%	13.9738%	85.5895%
Precision				
Value	<=40000 (54)	<=60000 (276)	<=80000 (320)	>80000 (246)
<=40000 (44)	62.9630%	3.6232%	0.0000%	0.0000%
<=60000 (267)	37.0370%	73.1884%	14.0625%	0.0000%
<=80000 (356)	0.0000%	22.8261%	75.9375%	20.3252%
>80000 (229)	0.0000%	0.3623%	10.0000%	79.6748%

c)



d)

Figure 5.15: a) Performance of the Naive Bayes b) Markov Blanket c) Aug. Markov Blanket d) Marginal probabilities for Aug. Markov Blanket model

5.3 Nonlinear Data Analysis and Wall Performance

Once the best performing models are selected, the indices of connection that are dependent on the mutual information and entropy reduction ratios are selected. The results for the shear dominant mode regarding the target variable V_{max} are shown in Table 5.3 and Figure 5.16, while those regarding μ are shown in Table 5.4 and Figure 5.17.

Table 5.3: Indices based on mutual information for entropy reduction of the target variable V_{max} for the shear dominant behavior.

Predictive Var.	t	ft	N	L
MI	0.2509	0.0655	0.2044	0.1433
Ent. Red %	12.980	3.390	10.570	7.410
Indices	0.1298	0.0339	0.1057	0.0741

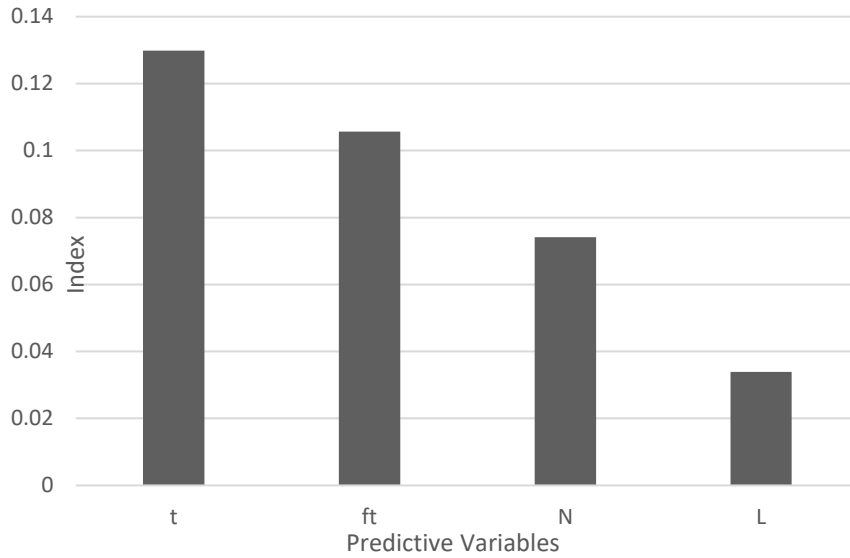


Figure 5.16: Indices for entropy reduction for the target variable V_{max} for shear dominant behavior

Table 5.4: Indices based on mutual information for entropy reduction of the target variable μ for the shear dominant behavior.

Predictive Var.	H	L	ft
MI	0.187	0.0602	0.0306
Ent. Red %	12.29	3.95	2.01
Indices	0.1229	0.0395	0.0201

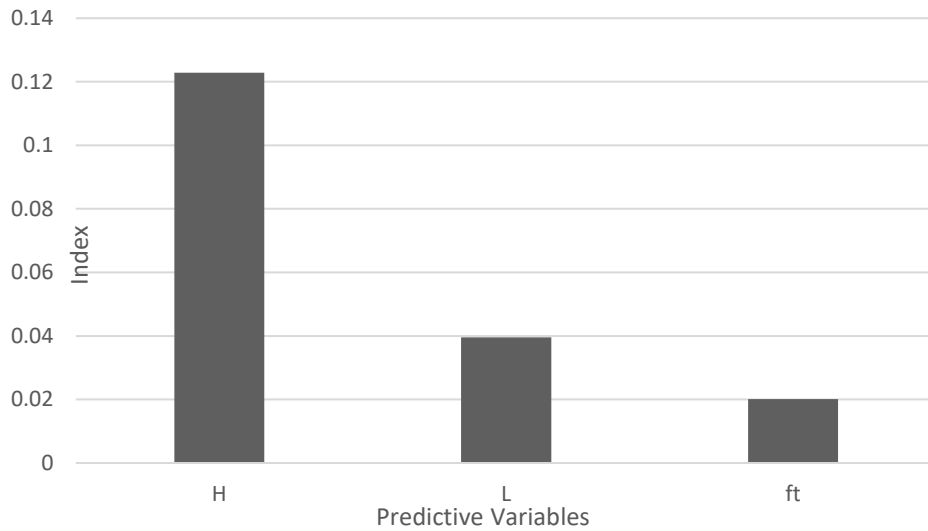


Figure 5.17: Indices for entropy reduction for the target variable μ for shear dominant behavior

The marginal entropy of V_{max} calculated using Equation (2.12), is $H(V_{max}) = 1.93$. Using this value, it was possible to extract the indices presented. It is realized that the most influential parameter on the strength of the pier is the thickness t , followed by the tensile strength f_t . The marginal entropy for μ is $H(\mu) = 1.52$. The most influential parameter on the ductility of the pier is the height H followed by the length L . For any strengthening intervention that takes place, those parameters must be considered as primary targets.

Looking on the flexural dominant mode of failure, the target variable selected is the maximum strength V_{max} . The results are shown in Table 5.5 and Figure 5.18. The marginal entropy of V_{max} is $H(V_{max}) = 1.81$. When extracting the indices, it is noticed that the most influential parameters on the strength of the pier is the aspect ratio H/L followed by the length L . The length of the piers is determined by the size of the openings in the URM walls, which could be a way to tackle the problem during strengthening interventions.

Table 5.5: Indices based on mutual information for entropy reduction of the target variable V_{max} for the flexure dominant behavior.

Predictive Var.	H/L	L	ft	t	N	fm
MI	0.3728	0.2039	0.1316	0.1187	0.0635	0.0112
Ent. Red %	20.6108	11.2767	7.2763	6.5617	3.5093	0.6198
Indices	0.206108	0.112767	0.072763	0.065617	0.035093	0.006198

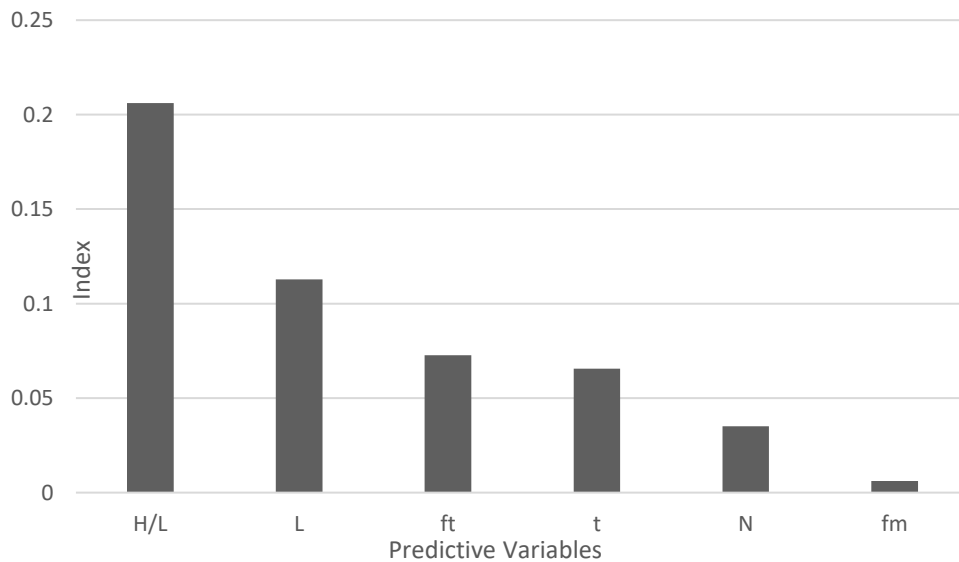


Figure 5.18: Indices for entropy reduction for the target variable V_{max} for flexural dominant behavior

It is worth mentioning that in the last model, there is some established connections between the predictive variables. The most reliable ones between H/L and L with $I = 0.2525$ and reduction in entropy on the length L parameter of 12.67%. This relation is developed due to the length being part of the aspect ratio. The next connection is between H/L and t with $I = 0.0106$ and reduction in entropy on the thickness t parameter of 0.5284 %. The fact that those connections exist reflects the realistic factor in determining the probabilities and the influence of certain parameters on the target variable which could be ignored in the linear correlation study.

5.4 Case Study: Performance Analysis of the Piers Based on the Linear and Nonlinear Data Analysis Models

In the light of Chapter 4, an attempt to propose an improvement in the performance of the piers is made relying on the linear data analysis for single parameters and the nonlinear data analysis for multiple parameters. The data for the shear dominant behavior are used to assess **Pier1** while the data for the flexural dominant behavior are used to assess **Pier2**.

5.4.1 Information for Pier1 with Shear Dominant Behavior

To start with the more comprehensive nonlinear data analysis model, it is evident that the most influential parameters are thickness t , tensile strength f_t , Vertical stresses N , and length L . Observing the current values for Pier1, it puts the pier in the high end in terms of t and L . Also, N is not usually a factor that can be controlled in strengthening interventions. Therefore, the f_t parameter seems like a reasonable way to strengthen the pier given the room for improvement and the feasibility of the application in practice. It is worth noting that the f_t factor showed negligible effect on the strength of the pier in the linear data analysis model. This indicates that the linear model is not capable of capturing the full range of influence of this parameter which may influence other parameters that in turn can improve the strength. Figure 5.19a shows the probability distribution of the capacity V_{max} of Pier1 using the fixed values extracted from the existing parameters of the pier. Figure 5.19b shows the variation in the probability distribution of V_{max} after improving the tensile strength of the pier from less than 0.173MPa to less than 0.243MPa. The probability the pier will have a strength more than 165kN increase from 20.49% to 70.45%. This is considered as a major improvement on the performance which could be achieved using injection of hydraulic mortar into the wall.

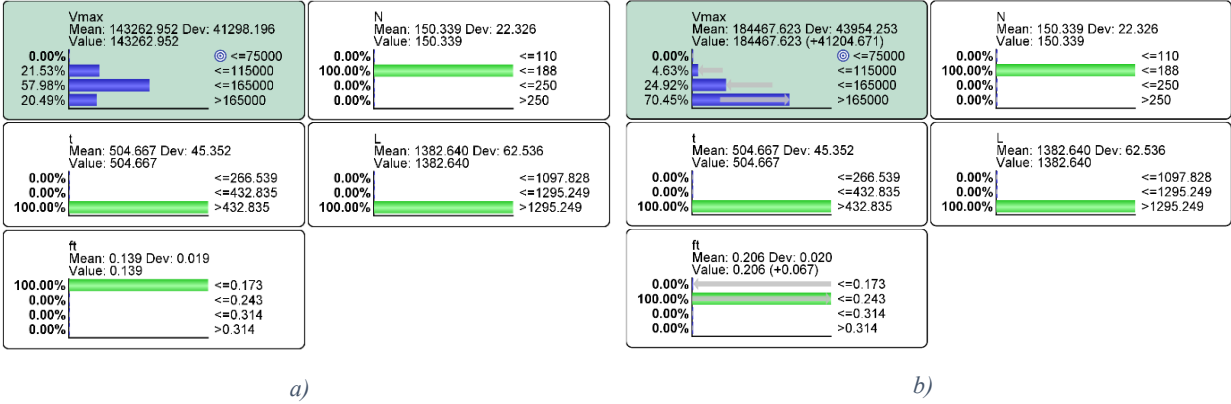


Figure 5.19: a) Probability distribution for V_{max} with the existing parameters extracted from Pier I b) after the improvement of the factor f_t .

We also must check the effect of this alteration of the range of tensile strength on the ductility factor $\mu = D_{ult}/D_{max}$. From Figs. 5.20a and 5.20b we can see a decrease in the ductility larger than 3.6 from 28.24% to 16.76% after moving f_t from less than 0.173MPa to less than 0.243MPa. Since the gain in strength is larger than the loss in ductility, it is reasonable to say that this compromise in the tensile strength is an acceptable strengthening intervention.

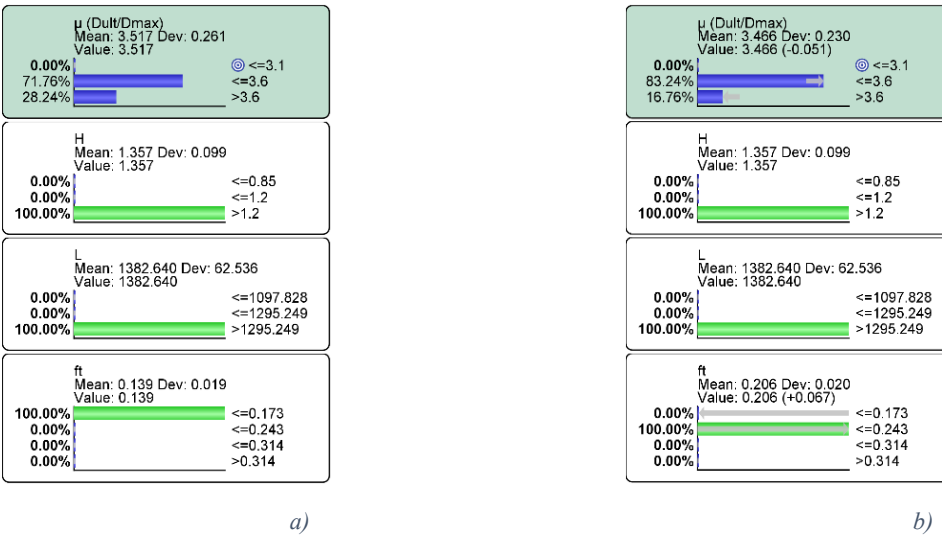


Figure 5.20: a) Probability distribution of μ with the existing parameters extracted from Pier I b) after the improvement of the factor f_t .

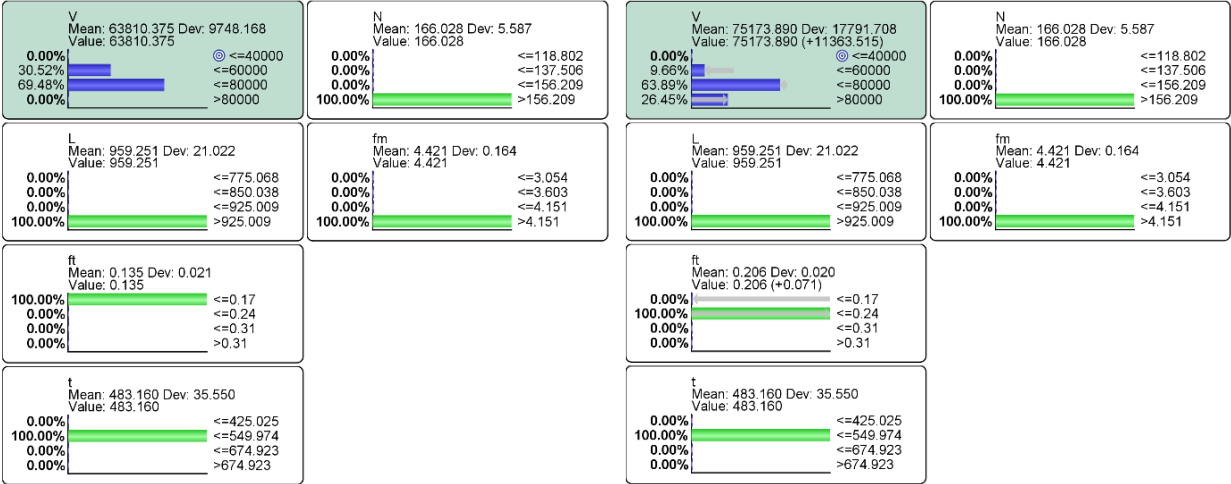
5.4.2 Information for Pier2 with Flexural Dominant Behavior

From the nonlinear data analysis model, it is shown that the most predictive parameters are the aspect ratio H/L , length L , tensile strength f_t , thickness t , vertical stress N , and the compressive strength f_m . Since H/L is only relevant through the variation of L , it would not be included in the analysis of Pier2. The L , N , and f_m are already in the high end of the probability distribution, thus they would be subject to alteration. In Figs. 5.21a, 5.21b, 5.21c, and 5.21d we will see the predictive influence of the variables, f_t and t on the strength of the pier V_{max} .

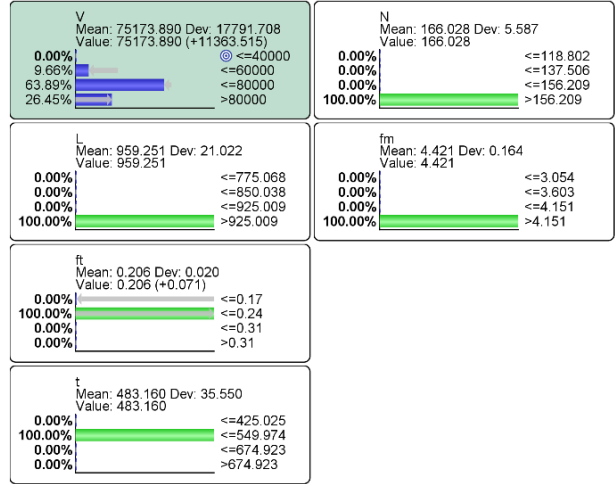
With increasing the range of f_t from less than 0.17MPa to less than 0.24MPa, an increase in the probability of V_{max} to be higher than 80kN increases by 26.45%. Another addition to the range of f_t to be less than 0.31MPa pushes the probability of V_{max} at higher than 80kN to 64.02%.

On the other hand, an increase in the range of t from less than 550mm to less than 675mm increases the probability of V_{max} to be higher than 80kN by 54.19%. Given the limitations on the thickness of the walls in the existing URM structures, increasing f_t also sounds like a reasonable strengthening intervention that can be achieved through hydraulic mortar injections into the wall.

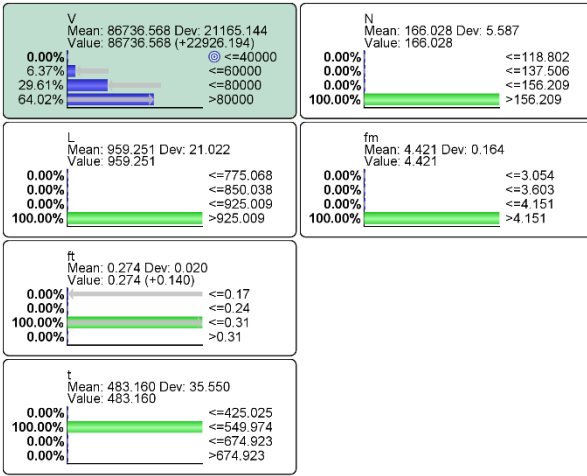
From the linear data analysis model for f_t , it shows the relationship between V_{max} and f_t is developed through the following equation: $y = 62.3x + 56.9$. The high slope value is also an indication of the great influence of this predictive variable on the strength of the pier.



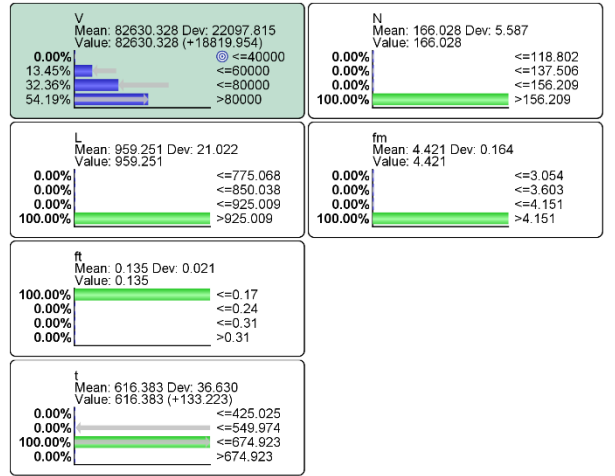
a)



b)



c)



d)

Figure 5.21: a) Probability distribution of the variable V_{max} with the existing parameters of Pier2 b) c) after the improvement of f_t d) after the improvement of t .

In summary, using a sophisticated nonlinear data analysis approach, a more comprehensive evaluation of the influence of certain characteristics of the URM piers is achieved. Probability based models are built using the Bayesian Networks to find relationships between the different parameters and the performance of the walls. Those models are validated using a cross validation method that provides the precision and the reliability of the connections. Indices generated represent the influence on the maximum shear capacities and displacements of the piers.

Chapter 6: Conclusions, Limitations and Scope for Future Work

6.1 Summary and Conclusions

Several formulations in the codes and scientific research are proposed to recognize the shear and flexural capacities in piers which could be easily assigned to the force-displacement back-bone curves in the model. Four shear formulations and five flexural formulations are selected in this work to be analyzed. A parametric study is performed to identify the performance of the capacity formulations for piers in respect to the multiple parameters available within the complex masonry walls where the degree of precision is important. Thus, in this study the number of parameters identified are:

- Four major parameters are identified for the shear capacity comparisons such as: the aspect ratio, the texture of the walls, the vertical stresses, and the scale of the specimens, respectively.
- Seven major parameters were selected for the capacity formulations for flexure dominant behavior such as: the aspect ratio, the boundary conditions, the vertical stresses, the typology, the wall thickness, the scale, and the strengthening through injection.

To simulate the URM piers response under lateral loading, deterministic model is created using the open-source software OpenSees. The model uses distributed plasticity applied through an equivalent frame macro modeling technique and the model was calibrated against experimental tests on piers representing the behavior dominated by shear and flexure. A feasible model was developed, and the simulated hysteresis loops can overlap that from experimental tests.

After the calibration of the deterministic model for the pier, based on experimental testing, the linear data for the major parameters that influence the behavior in the shear and flexural dominant modes of failure was generated and presented hereafter.

- Four parameters were tested for the shear dominant mode of failure represented as the height H , the vertical forces N , the length L and the thickness t .
- The results show that the length of the pier has the most influence on the performance of the pier. Thus, increasing the length of the pier which can be achieved through the limiting of the wall openings could be a good start point for improving the strength.
- Seven parameters are tested for the flexural dominant mode of failure represented as the height of the pier H , the compressive strength f_m , the tensile strength f_t , the tensile modulus of elasticity E_t , the vertical forces N , the length of the pier L , and the thickness of the pier t .
- The results show that the length of the pier and the tensile strength of the pier has the most influence effect on the nonlinear response.

To understand the influence of predictive variables on the strength and deformation capacity of the URM piers under examination, it is important to extract comparative indices that represent their connection to the target variables. In this case the target variables are the maximum shear strength V_{max} and the lateral displacement expressed in terms of displacement ductility μ defined for the purpose of this study. However, the second parameter is not representative because the URM piers are designed to behave elastically. The failure modes of piers are divided between the shear and flexural mode. Using a probabilistic machine learning tool that relies on Bayes theorem, a nonlinear correlation is developed through building acyclic models that is validated through K-Folds Cross validation method.

The façade wall of a building in Montreal is used herein as a case study. Two piers are extracted from the wall each from different floor to represent the major two modes of behavior of URM piers. Pier1 from the second floor experiences a shear dominant behavior due to its squat nature with an aspect ratio $H/L = 1.22$. This is associated with some energy dissipation and high elastic stiffness, shown in the hysteretic loop developed for the in-plane cyclic loading. The maximum shear capacity of the pier is $V_{\max}=161$ kN and the associated lateral deflection is 3.25 mm. Then, the ultimate shear capacity reaches 84.5kN at 10.25mm leading to $\mu = 3.15$. It is worth mentioning that pier's failure is considered when 20% of shear strength is lost, however the analysis can be conducted beyond this value. However, the response of building may be completely different in terms of ductility and experimental studies are required. More data from this analysis are:

- From the probability model, it was shown that the small tensile strength of the Pier1 is a major predictor of the maximum shear capacity V_{\max} of the pier. By shifting the tensile strength from the range less than 0.173MPa to less than 0.243MPa may lead to 50% probability of increasing the maximum shear capacity above 161kN.
- Analyzing the lateral displacement of Pier1 due to improving the tensile strength, shows a decrease of 11.5% in the probability of having μ larger than 3.6.

Pier 2 from the first floor experiences a flexural dominant behavior due to its slender nature with aspect ratio of 2.15. This is associated with low energy dissipation and lower elastic stiffness compared to the squat pier. The maximum shear capacity is 183kN with a plateau in the curve showing at about 7.5mm with a decrease in the stiffness as the elastic capacity is reached at 3.25mm with a value of 139kN:

- From the probability model, it is shown that the tensile strength has good predictive influence on the performance of Pier2. An increase of 64% in the probability of achieving a strength V_{\max} higher than 80kN is achieved by shifting the range of tensile strength from 0.17MPa to 0.24MPa.
- Another predictor is the thickness of the wall which showed an increase of 54% in the probability of achieving a strength V_{\max} higher than 80kN by shifting the range of thickness from less than 550mm to less than 675mm.

6.2 Limitations

Existing URM structures are very complex type of construction that require detailed studies to understand its seismic behavior and provide accurate analysis of results. Unlike concrete and steel structures, there is not an established practice able to tackle the nonlinear response of URM elements even though several techniques are suggested in the literature. Micro-modeling techniques show limited utility for small sized elements due to the enormous amount of details that need to be covered and the unknown parameters required to be extracted from existing structures without imposing any damage. Conversely, macro-models are simple in their approach and useful in representing the behavior of URM if calibrated properly. The main assumption to consider is the box behavior that can be accomplished after the elimination of any local failure in the masonry walls and spandrels.

The purpose of this work was to identify the parameters that contributes to the response of URM building components and no to the whole response of buildings. In addition, this work does not address retrofit techniques for existing URM buildings. It is known that the seismic activity in Montreal shows high demand in low-period ranges that affect the low-rise buildings with URM

structures. Among the existing low-rise buildings in Montreal, a low-to-moderate percentage are URMs, which are especially located in the historical sites of Montreal city.

Regarding modelling, the equivalent frame models can be used. Hence, under the category of macro-modeling approaches, two main subcategories can be defined: the lumped plasticity models and the distributed plasticity models. The failure modes are classified as shear dominant and flexural dominant types depending on the crack propagation within the elements exhibiting failure. It is important to capture both modes in the nonlinear models since they can influence the plasticity and the capacity to great extent. Based on experimental expertise, it is determined that yielding of masonry elements mostly occur at 0.007% interstorey drift ratio, displacement prior failure at 0.2% interstorey drift ratio, and complete failure at 20% decrease in the strength at 0.3% interstorey drift ratio. Those values are a good starting point for calibration.

In the aim of simplifying the modeling procedure for unreinforced masonry structures, utilizing the equivalent frame method with identified hinges at known positions has proven to be valid approach in capturing the capacities of major structural elements in typical masonry walls. However, identifying and assigning hinges in a model may be aleatory. Attention should be given in the modelling procedure and interpretation of results. Experimental testing of URM components is required for properly assigning the input parameters. The 2D analyses have limitations and 3D analyses are more complex. Caution should be given in the selected approach.

In the performed parametric study on capacity formulations, the data available in the literature for the spandrels was not enough to amount for conclusive results regarding their performance and its correlation with the suggested formulations. The conducted parametric study can be used to future simplified models. Such models will be able to run time history analysis without any time burden due to the limited number of degrees of freedom required. More data are required to yield

comprehensive and precise results on the use of the formulations which indicate the need for more experimental campaigns.

Herein, the calibrated model for the pier is 2D. The potential out-of-plane response due to forces that might act simultaneously due to the connection with perpendicular walls is not captured. Also, the effect of flexible horizontal diaphragms that are commonly found in the URM structures is not considered in this work. Extending the nonlinear analysis techniques from 2D to 3D, including flexible horizontal diaphragm is part of the future work.

The linear data analysis of the pier characteristics was a good preliminary approach. However, it lacks the realistic aspect of the conducted study due to the inevitable influence of the parameters on each other. Nevertheless, it can be suggested that implementing strengthening interventions that enhance those factors could be of great benefit to the strength. For example, the replacement of the mortar with newer ones will improve the cohesion and friction of the mortar to the stone units, thus increasing the tensile strength. This technique is expensive and has limits concerning the adherence of new material to the old material. As aforementioned, retrofit techniques are not part of this research work.

The nonlinear data analysis performed using the Bayesian Network is a more realistic approach for understanding the behavior of the URM piers. However, some limitations for such method include the complexity of the data curation that requires a trial-and-error approach and expert opinion to be utilized. This may lead to variation in the data and the yielded indices depending on the preconditions of the study. For future work, it is required to implement such analysis on different projects and use the commonalities to inhibit a more generalized approach that works better for URM structures. From the case study, different recommendations can be made. The thickness of the walls could have some limitations in the practice of strengthening interventions

due to the limited space in the existing structures and the impracticality of adding additional layers to the wall that might not be compatible with the existing layers. More advanced strengthening interventions that have the same influence on the walls can be applied. Those practices should be tested to yield their efficiency.

6.3 Scope for Future Work

In future work, more data can be collected to expand the range of information included for this conducted parametric study. The wall characteristics used in the study would be more comprehensive to allow more precision in determining the preferable capacity formulation for predicting wall strength. The study can expand to include more elaborated analysis of the spandrels which demand more experimental campaigns in that domain.

The calibrated pier model can be expanded to a full scaled wall. Understanding the connections between the piers and the spandrels and the stiffness relationship between those elements is important in capturing the behavior of the wall along the building height. A dynamic seismic analysis could be conducted for a more realistic assessment. Calibration is required for such 2D structures. Analysing models as 3D need experimental data.

The nonlinear data analysis using the machine learning algorithms must be scaled for larger data sets. Based on the trial-and-error approach in the data discretization, the conduction of repetitive studies would be important. Such repetition would form a benchmark that may be used to understand the validity of yielded information. The data distribution, the calibration methods and the algorithms used to learn the connections between the predictive variables can vary to a great extent depending on the given models.

References

- A. Goulet, J. (2020). *Probabilistic Machine Learning for Civil Engineers*. The MIT press.
http://profs.polymtl.ca/jagoulet/Site/Goulet_web_page_BOOK.html
- Abo-El-Ezz, A., Nollet, M.-J., & Nastev, M. (2013). Seismic fragility assessment of low-rise stone masonry buildings. *Earthquake Engineering and Engineering Vibration*, 12(1), 87–97.
<https://doi.org/10.1007/s11803-013-0154-4>
- Abrams, D. P. (2001). Performance-based engineering concepts for unreinforced masonry building structures. *Progress in Structural Engineering and Materials*, 3(1), 48–56.
<https://doi.org/10.1002/pse.70>
- Ademović, N., & Oliveira, D. V. (2012). *Seismic assessment of a typical masonry residential building in Bosnia and Herzegovina*. Fifteenth World Conference on Earthquake Engineering, Lisbon, Portugal. <http://repositorium.sdum.uminho.pt/>
- Andrea, P. (2015). *Seismic assessment of existing and strengthened stone-masonry buildings: Critical issues and possible strategies*. 13, 1051–1071.
- Ang, A., and Tang, W. (1975). *Probability concepts in engineering planning and design*. Vol. 1, *Basic principles*.
- Anthoine, A., Magonette, G., & Magenes, G. (1994, September 28). Shear-compression testing and analysis of brick masonry walls. *ResearchGate*. 10th European Conference on Earthquake Engineering, Vienna, Austria.
https://www.researchgate.net/publication/303168220_Shear-compression_testing_and_analysis_of_brick_masonry_walls
- ASTM 519-02. (2002). *Standard test method for diagonal tension (shear) in masonry assemblages*.

- ASTM International. (2020). *ASTM C109 / C109M-20b, Standard Test Method for Compressive Strength of Hydraulic Cement Mortars (Using 2-in. Or [50 mm] Cube Specimens)* (p. West Conshohocken, PA). ASTM International. https://doi.org/10.1520/C0109_C0109M-20B
- Benedetti, A., & Steli, E. (2008). Analytical models for shear–displacement curves of unreinforced and FRP reinforced masonry panels. *Construction and Building Materials*, 22(3), 175–185. <https://doi.org/10.1016/j.conbuildmat.2006.09.005>
- Betti, M., Galano, L., & Vignoli, A. (2008, July). Seismic Response Of Masonry Plane Walls: A Numerical Study On Spandrel Strength. *AIP*. 2008 seismic engineering conference commemorating the 1908 Messina and Reggio Calabria earthquake, Reggio Calabria, Italy.
- Betti, M., Galano, L., & Vignoli, A. (2014). Comparative analysis on the seismic behaviour of unreinforced masonry buildings with flexible diaphragms. *Engineering Structures*, 61, 195–208. <https://doi.org/10.1016/j.engstruct.2013.12.038>
- Beyer, K. (2012). Peak and residual strengths of brick masonry spandrels. *Engineering Structures*, 41, 533–547. <https://doi.org/10.1016/j.engstruct.2012.03.015>
- Beyer, K., & Dazio, A. (2012). Quasi-Static Cyclic Tests on Masonry Spandrels. *Earthquake Spectra*, 28(3), 907–929. <https://doi.org/10.1193/1.4000063>
- Beyer, K., & Mangalathu, S. (2013). Review of strength models for masonry spandrels. *Bulletin of Earthquake Engineering*, 11(2), 521–542. <https://doi.org/10.1007/s10518-012-9394-3>
- Binda, L., Cardani, G., & Saisi, A. (2005, January 26). *A classification of structures and masonries for the adequate choice of repair*. International RILEM Workshop on Repair Mortars for Historic Masonry, Delft, Netherlands.

- Bosiljkov, V., Page, A., Bokan- Bosiljkov, V., & Zarnic, R. (2003). Performance based studies of in-plane loaded unreinforced masonry walls. *Journal Masonry International, Vol. 16, No. 2, Pp. 39-50., 16(2), 39–50.*
- Bosiljkov, V., & Tomažević, M. (2006). *Optimization of shape of masonry units and technology of construction for earthquake resistant masonry buildings.* Zavod za gradbeništvo Slovenije.
- Brignola, A., Frumento, S., Lagomarsino, S., & Podestà, S. (2008). Identification of Shear Parameters of Masonry Panels Through the In-Situ Diagonal Compression Test. *International Journal of Architectural Heritage, 3(1), 52–73.*
<https://doi.org/10.1080/15583050802138634>
- Bucchi, F., Arangio, S., & Bontempi, F. (2013). *Seismic assessment of historical masonry buildings with nonlinear static analysis. 102.*
- Canadian Standard Association, Design of Masonry Structures. (R2010).* CSA Group.
- Cardoso, R., Lopes, M., & Bento, R. (2005). Seismic evaluation of old masonry buildings. Part I: Method description and application to a case-study. *Engineering Structures, 27(14), 2024–2035.* <https://doi.org/10.1016/j.engstruct.2005.06.012>
- Cattari, S., & Lagomarsino, S. (2008, October 12). A strength criterion for the flexural behaviour of spandrels in un-reinforced masonry walls. *14th World Conference on Earthquake Engineering.*
- Chen, S., Webb, G. I., Liu, L., & Ma, X. (2020). A novel selective naïve Bayes algorithm. *Knowledge-Based Systems, 192,* 105361. <https://doi.org/10.1016/j.knosys.2019.105361>
- Churilov, S., & Dumova-Jovanoska, E. (2012). *In-plane shear behaviour of unreinforced masonry walls.* 14th European Conference on Earthquake Engineering.

- Conrady, S., & Jouffe, L. (2015). *Bayesian Networks & Bayesialab—A Practical Introduction for Researchers*. https://library.bayesia.com/articles/#!/bayesialab-knowledge-hub/book/a/h2__1778758044
- CSA. (2014). *S304: 2014 DESIGN OF MASONRY STRUCTURES*.
- Dash, R., Paramguru, R. L., & Dash, R. (2011). Comparative analysis of supervised and unsupervised discretization techniques. *International Journal of Advances in Science and Technology*, 2(3), 29–37.
- Davenport, W. B., & Root, W. L. (1987). Random Variables and Probability Distributions. In *An Introduction to the Theory of Random Signals and Noise* (pp. 19–44). IEEE. <https://doi.org/10.1109/9780470544143.ch3>
- Dolce, M. (1991). Schematizzazione e modellazione degli edifici in muratura soggetti ad azioni sismiche. *Schematizzazione e Modellazione Degli Edifici in Muratura Soggetti Ad Azioni Sismiche*, 25(242), 44–57.
- Elmenschawi, A., & Shrive, N. (2015). Assessment of Multi-Wythe Stone Masonry Subjected to Seismic Hazards. *Journal of Earthquake Engineering*, 19(1), 85–106.
- Elmenschawi, A., Sorour, M., Mufti, A., Jaeger, L. G., & Shrive, N. (2010). Damping mechanisms and damping ratios in vibrating unreinforced stone masonry. *Engineering Structures*, 32(10), 3269–3278. <https://doi.org/10.1016/j.engstruct.2010.06.016>
- EN 1015-11. (2019). *Methods of test for mortar for masonry—Part 11: Determination of flexural and compressive strength of hardened mortar*. ITeh Standards Store. <https://standards.iteh.ai/catalog/standards/cen/14596d4c-119b-4a78-94e1-3fe481a29bde/en-1015-11-2019>

- EN08-3. (2005). CEN. *Eurocode 8: Design of Structures for Earthquake Resistance. Part 3: Assessment and retrofitting of buildings.*
- FEMA 306. (1998). *Evaluation of Earthquake-Damaged Concrete and Masonry Wall Buildings.* ATC.
- FEMA 356. (2000). *Prestandard for the seismic rehabilitation of buildings.*
- Foraboschi, P. (2009). Coupling effect between masonry spandrels and piers. *Materials and Structures*, 42(3), 279–300. <https://doi.org/10.1617/s11527-008-9405-7>
- Frumento, S., Magenes, G., Morandi, P., & Calvi, G. M. (2009). *Interpretation of experimental shear tests on clay brick masonry walls and evaluation of q-factors for seismic design.* <http://rgdoi.net/10.13140/RG.2.2.13998.61766>
- Fu, S., & Desmarais, M. C. (2010). Markov blanket based feature selection: A review of past decade. *Proceedings of the World Congress on Engineering*, 1, 321–328.
- Gelman, A., Carlin, J. B., Stern, H. S., Dunson, D. B., Vehtari, A., & Rubin, D. B. (2013). *Bayesian Data Analysis, Third Edition.* CRC Press.
- Graziotti, F., Magenes, G., & Penna, A. (2012). *Experimental cyclic behaviour of stone masonry spandrels.* 10.
- Graziotti, F., Penna, A., & Magenes, G. (2014). *Influence of timber lintels on the cyclic behaviour of stone masonry spandrels.* 9th International Masonry Conference, Guimaraes.
- Graziotti, F., Rossi, A., Mandirola, M., Penna, A., & Magenes, G. (2016, June 26). *Experimental characterisation of calcium-silicate brick masonry for seismic assessment.* Proceedings of the 16th International Brick and Block Masonry Conference, Padova, Italy.
- Hekimi, B. (2012). *The Physical and Mechanical Properties of an Argillaceous Limestone.* McGill University.

- Izaguirre, A., Lanas, J., & Álvarez, J. I. (2010). Ageing of lime mortars with admixtures: Durability and strength assessment. *Cement and Concrete Research*, 40(7), 1081–1095. <https://doi.org/10.1016/j.cemconres.2010.02.013>
- Kent, C., & Park, R. (1971). Flexural Members With Confined Concrete. *Journal of the Structural Division*, 97(ST7). <https://www.scribd.com/document/360345179/Kent-Park-Flexural-Members-With-Confined-Concrete>
- Knox, C. L., Dizhur, D., & Ingham, J. M. (2017). Experimental Cyclic Testing of URM Pier-Spandrel Substructures. *Journal of Structural Engineering*, 143(2), 04016177. [https://doi.org/10.1061/\(ASCE\)ST.1943-541X.0001650](https://doi.org/10.1061/(ASCE)ST.1943-541X.0001650)
- Krefeld, W. J. (1938). Effect of shape of specimen on the apparent compressive strength of brick masonry. *Proceedings of the American Society of Materials, Philadelphia* p, 363–369.
- Lagamarsino, S. (2012). Damage assessment of churches after L'Aquila earthquake (2009). *Bulletin of Earthquake Engineering*, 10(1), 73–92. <https://doi.org/10.1007/s10518-011-9307-x>
- Lagamarsino, S., & Cattari, S. (2015). PERPETUATE guidelines for seismic performance-based assessment of cultural heritage masonry structures. *Bulletin of Earthquake Engineering*, 13(1), 13–47. <https://doi.org/10.1007/s10518-014-9674-1>
- Lagamarsino, S., Penna, A., Galasco, A., & Cattari, S. (2013). TREMURI program: An equivalent frame model for the nonlinear seismic analysis of masonry buildings. *Engineering Structures*, 56, 1787–1799. <https://doi.org/10.1016/j.engstruct.2013.08.002>
- Lang, K. (2002). *Seismic vulnerability of existing buildings. A dissertation submitted in fulfilment of the requirements for the degree of Doctor of Technical Sciences*. Swiss Federal Institute of Technology.

- Lee, J.-H., Li, C., Oh, S.-H., Yang, W.-J., & Yi, W.-H. (2008). Evaluation of Rocking and Toe Crushing Failure of Unreinforced Masonry Walls. *Advances in Structural Engineering*, *11*(5), 475–489. <https://doi.org/10.1260/136943308786411998>
- Lima, F. B., Lima, A. N., & Assis, W. S. (2012). Study of the influence of compressive strength and thickness of capping-mortar on compressive strength of prisms of structural clay blocks. *15th International Brick and Block Masonry Conference, Florianopolis, Brazil*.
- Lourenco, P. B. (2002). Computations on historic masonry structures. *Prog. Struct. Engng Mater.*, *4*, 301–309. <https://doi.org/10.1002/pse.120>
- Lourenço, P. B., Oliveira, D. V., Roca, P., & Orduña, A. (2005). Dry joint stone masonry walls subjected to in-plane combined loading. *Journal of Structural Engineering*, *131*(11), 1665–1673.
- Lourenço, P. B., & Ramos, L. F. (2004). Characterization of Cyclic Behavior of Dry Masonry Joints. *Journal of Structural Engineering*, *130*(5), 779–786.
- Magenes, G. (1999). *Simplified models for the seismic analysis of masonry buildings*, G.N.D.T. Report.
- Magenes, G. (2006). *Masonry building design in seismic areas: Recent experiences and prospects from a European standpoint*. First European Conference on Earthquake Engineering and Seismology, Geneva, Switzerland.
- Magenes, G., & Calvi, G. M. (1997a). In-plane seismic response of brick masonry walls. *Earthquake Engineering & Structural Dynamics*, *26*(11), 1091–1112.
- Magenes, G., & Calvi, G. M. (1997b). In-plane seismic response of brick masonry walls. *Earthquake Engineering & Structural Dynamics*, *26*(11), 1091–1112.

[https://doi.org/10.1002/\(SICI\)1096-9845\(199711\)26:11<1091::AID-EQE693>3.0.CO;2-6](https://doi.org/10.1002/(SICI)1096-9845(199711)26:11<1091::AID-EQE693>3.0.CO;2-6)

- Magenes, G., & Della Fontana, A. (1998). *Simplified non-linear seismic analysis of masonry buildings*. 8.
- Magenes, G., Morandi, P., & Penna, A. (2008a). *D 7.1c Test results on the behaviour of masonry under static cyclic in plane lateral loads* (p. 129). ESECMaSE.
- Magenes, G., Morandi, P., & Penna, A. (2008b). *In plane cyclic tests of calcium silicate masonry walls*. 12th International Brick/Block Masonry Conference, Sydney.
- Magenes, G., Penna, A., Galasco, A., & Da Paré, M. (2010, January 1). *In-plane cyclic shear tests of undressed double-leaf stone masonry panels*. 8th International Masonry Conference, Dresden.
- Magenes, G., Penna, A., Galasco, A., & Rota, M. (2010, January 1). *Experimental Characterisation of Stone Masonry Mechanical Properties*. 8th International Masonry Conference, Dresden.
- Maglogiannis, I. G. (2007). *Emerging Artificial Intelligence Applications in Computer Engineering: Real Word AI Systems with Applications in EHealth, HCI, Information Retrieval and Pervasive Technologies*. IOS Press.
- Mann, W., & Müller, H. (1982). Failure of Shear-Stressed Masonry- an Enlarged Theory, Tests and Application to Shear Walls. *British Ceramic Society*, 30, 223–235.
- Marini, A., & Spacone, E. (2006). Analysis of Reinforced Concrete Elements Including Shear Effects. *ACI Structural Journal*, 103(5). <https://doi.org/10.14359/16916>
- Mario Como. (2013). *Statics of Historic Masonry Constructions*. Springer.

- Martino R., Spacone E., & Kingsley G. (2000). Nonlinear Pushover Analysis of RC Structures. *Advanced Technology in Structural Engineering*, 1–8.
[https://doi.org/10.1061/40492\(2000\)38](https://doi.org/10.1061/40492(2000)38)
- McKenna, F., Fanves, G. L., Scott, H. M., & Jeremic, B. (2000). *Open system for earthquake engineering simulation (OpenSees)*.
- Milosevic, J., Gago, A., Lopes, M., & Bento, R. (2012). Experimental Tests on Rubble Masonry Specimens–Diagonal Compression, Triplet and Compression Tests. *15th World Conference on Earthquake Engineering*.
- Mohd Yassin, M. H. (1994). *Nonlinear analysis of prestressed concrete structures under monotonic and cyclic loads*. Berkeley, Univ. of California, Ph. D. Thesis.
- Mondkar, D. P., & Powell, G. H. (1977). ANSR - a general purpose computer program for analysis of nonlinear structural response. *Structural Mechanics in Reactor Technology*.
http://inis.iaea.org/Search/search.aspx?orig_q=RN:10459235
- Nielsen, T. D., & JENSEN, F. V. (2009). *Bayesian Networks and Decision Graphs*. Springer Science & Business Media.
- Nollet, M.-J., Lefebvre, K., & Chaallal, O. (2004). *Structural Characteristics of Historical Buildings in Old Montreal*. 11.
- NRC. (2015). *National Building Code of Canada: 2015*. National Research Council of Canada. Canadian Commission on Building and Fire Codes.
- NTC08. (2008). *Italian Building Code. D.M. 14.01.2008: Norme Tecniche per le Costruzioni*. Italian Ministry of Infrastructures and Transportation: Rome.

- Oliveira, D. V. (2003). *Experimental and numerical analysis of blocky masonry structures under cyclic loading. Thesis submitted in fulfilment of the requirements for the degree of Doctor of Philosophy in Civil Engineering.* University of Minho.
- OPCM 3431. (2005). *Ulteriori modifiche ed integrazioni all OPCM 3274/03 (in Italian).*
- Paninski, L. (2003). Estimation of Entropy and Mutual Information. *Neural Computation*, 15(6), 1191–1253. <https://doi.org/10.1162/089976603321780272>
- Parks Canada Agency. (1998). *Monklands / Villa Maria Convent National Historic Site of Canada* (No. 1974-H, 2009-SDC-CED-068). https://www.pc.gc.ca/apps/dfhd/page_nhs_eng.aspx?id=651
- Pasticier, L., Amadio, C., & Fragiaco, M. (2008). Non-linear seismic analysis and vulnerability evaluation of a masonry building by means of the SAP2000 V.10 code. *Earthquake Engineering & Structural Dynamics*, 37(3), 467–485.
- Pearl, J. (1988). *Probabilistic Reasoning in Intelligent Systems: Networks of Plausible Inference* Morgan Kaufmann, San Mateo, California 19882. *Guttman EA Suchman PF Lazarfeld SA Star and JA Classen Wiley New York 1966.*
- Penna, A. (2015). Seismic assessment of existing and strengthened stone-masonry buildings: Critical issues and possible strategies. *Bulletin of Earthquake Engineering*, 13(4), 1051–1071. <https://doi.org/10.1007/s10518-014-9659-0>
- Penna, A., Senaldi, I., Magenes, G., & Galasco, A. (2014). *Pushover analysis of unreinforced masonry buildings with different levels of diaphragm stiffness.* Second European Conference on Earthquake Engineering and Seismology, Istanbul.

- Peruch, M., Spacone, E., & Camata, G. (2019). Nonlinear analysis of masonry structures using fiber-section line elements. *Earthquake Engineering & Structural Dynamics*, 48(12), 1345–1364. <https://doi.org/10.1002/eqe.3188>
- Peruch Matteo, Spacone Enrico, & Shing P. Benson. (2019). Cyclic Analyses of Reinforced Concrete Masonry Panels Using a Force-Based Frame Element. *Journal of Structural Engineering*, 145(7), 04019063. [https://doi.org/10.1061/\(ASCE\)ST.1943-541X.0002335](https://doi.org/10.1061/(ASCE)ST.1943-541X.0002335)
- Petrovčič, S., & Kilar, V. (2013). Seismic failure mode interaction for the equivalent frame modeling of unreinforced masonry structures. *Engineering Structures*, 54, 9–22. <https://doi.org/10.1016/j.engstruct.2013.03.050>
- Petry, S., & Beyer, K. (2014a). Influence of boundary conditions and size effect on the drift capacity of URM walls. *Engineering Structures*, 65, 76–88. <https://doi.org/10.1016/j.engstruct.2014.01.048>
- Petry, S., & Beyer, K. (2014b). Scaling unreinforced masonry for reduced-scale seismic testing. *Bulletin of Earthquake Engineering*, 12(6), 2557–2581. <https://doi.org/10.1007/s10518-014-9605-1>
- Petry, S., & Beyer, K. (2015a). Force–displacement response of in-plane-loaded URM walls with a dominating flexural mode. *Earthquake Engineering & Structural Dynamics*, 44(14), 2551–2573. <https://doi.org/10.1002/eqe.2597>
- Petry, S., & Beyer, K. (2015b). Limit states of modern unreinforced clay brick masonry walls subjected to in-plane loading. *Bulletin of Earthquake Engineering*, 13(4), 1073–1095. <https://doi.org/10.1007/s10518-014-9695-9>

- Raka, E., Spacone, E., Sepe, V., & Camata, G. (2015). Advanced frame element for seismic analysis of masonry structures: Model formulation and validation. *Earthquake Engineering & Structural Dynamics*, *44*(14), 2489–2506. <https://doi.org/10.1002/eqe.2594>
- Richardson, D. H. (1968). The Exact Distribution of a Structural Coefficient Estimator. *Journal of the American Statistical Association*, *63*(324), 1214–1226. <https://doi.org/10.1080/01621459.1968.10480921>
- RILEM, T. C. (1994). *LUM B6 Diagonal tensile strength tests of small wall specimens, 1991. RILEM Recommendations for the testing and use of constructions materials*, 488–489.
- Rinaldin, G., Amadio, C., & Macorini, L. (2016). A macro-model with nonlinear springs for seismic analysis of URM buildings. *Earthquake Engineering & Structural Dynamics*, *45*(14), 2261–2281. <https://doi.org/10.1002/eqe.2759>
- Rodriguez, J. D., Perez, A., & Lozano, J. A. (2010). Sensitivity Analysis of k-Fold Cross Validation in Prediction Error Estimation. *IEEE Transactions on Pattern Analysis and Machine Intelligence*, *32*(3), 569–575. <https://doi.org/10.1109/TPAMI.2009.187>
- Rota, M., Penna, A., Strobbia, C., & Magenes, G. (2011). Typological Seismic Risk Maps for Italy. *Earthquake Spectra*, *27*(3), 907–926. <https://doi.org/10.1193/1.3609850>
- Sekhon, J. (2009). *The Neyman—Rubin Model of Causal Inference and Estimation Via Matching Methods* (J. M. Box-Steffensmeier, H. E. Brady, & D. Collier, Eds.; Vol. 1). Oxford University Press. <https://doi.org/10.1093/oxfordhb/9780199286546.003.0011>
- Silva, B., Dalla Benetta, M., da Porto, F., & Modena, C. (2014). Experimental assessment of in-plane behaviour of three-leaf stone masonry walls. *Construction and Building Materials*, *53*, 149–161. <https://doi.org/10.1016/j.conbuildmat.2013.11.084>

- Thamboo, J., & Dhanasekar, M. (2019). Correlation between the performance of solid masonry prisms and wallettes under compression. *Journal of Building Engineering*, 22. <https://doi.org/10.1016/j.jobbe.2019.01.007>
- Tomazevic, M. (1978). *The Computer Program POR* [Report ZRMK].
- Tomazevic, M. (1996). *Recent Advances in Earthquake-Resistant Design of Masonry Buildings: European Prospective*. 11th World Conference on Earthquake Engineering, Acapulco.
- Tomažević, M. (2000). Some aspects of experimental testing of seismic behavior of masonry walls and models of masonry buildings. *Journal of Earthquake Technology*, 37(404), 101–117.
- Turnšek, V., & Čačovič, F. (1971). *Some experimental results on the strength of brick masonry walls*. 2nd International Brick-Masonry Conference, British Ceramic Society, Stoke-on-Trent.
- Vasconcelos, G., & Lourenço, P. B. (2006). *Assessment of the in-plane shear strength of stone masonry walls by simplified models*. <http://repositorium.sdum.uminho.pt/handle/1822/6547>
- Vasconcelos, G., & Lourenço, P. B. (2009). Experimental characterization of stone masonry in shear and compression. *Construction and Building Materials*, 23(11), 3337–3345.
- Yi Tianyi, Moon Franklin L., Leon Roberto T., & Kahn Lawrence F. (2006). Lateral Load Tests on a Two-Story Unreinforced Masonry Building. *Journal of Structural Engineering*, 132(5), 643–652. [https://doi.org/10.1061/\(ASCE\)0733-9445\(2006\)132:5\(643\)](https://doi.org/10.1061/(ASCE)0733-9445(2006)132:5(643))

Appendix A

Cyclic Response for Piers with Dominant Shear Failure

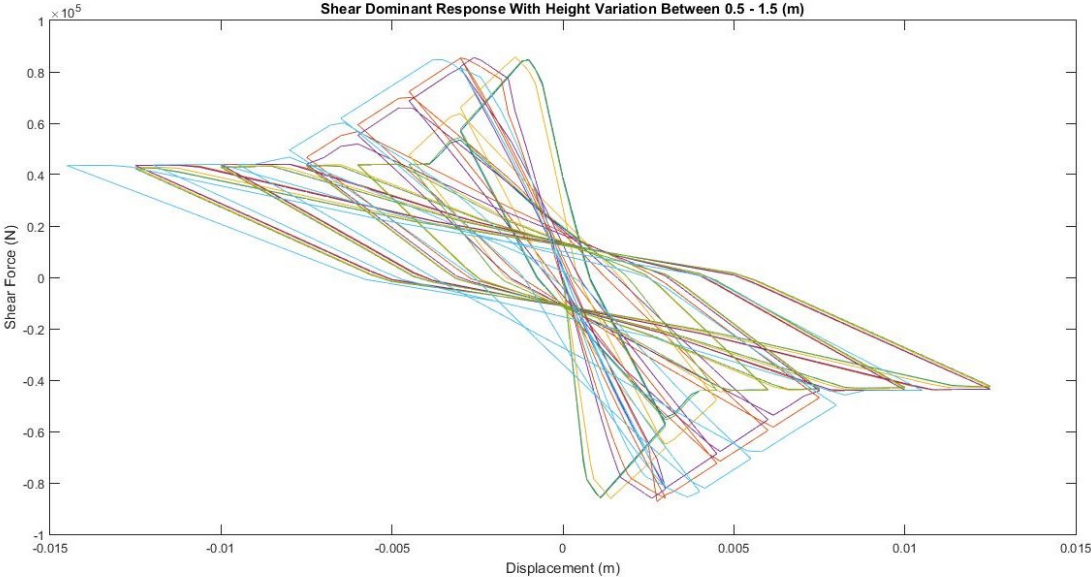


Figure A-1: Shear force vs displacement with height variation

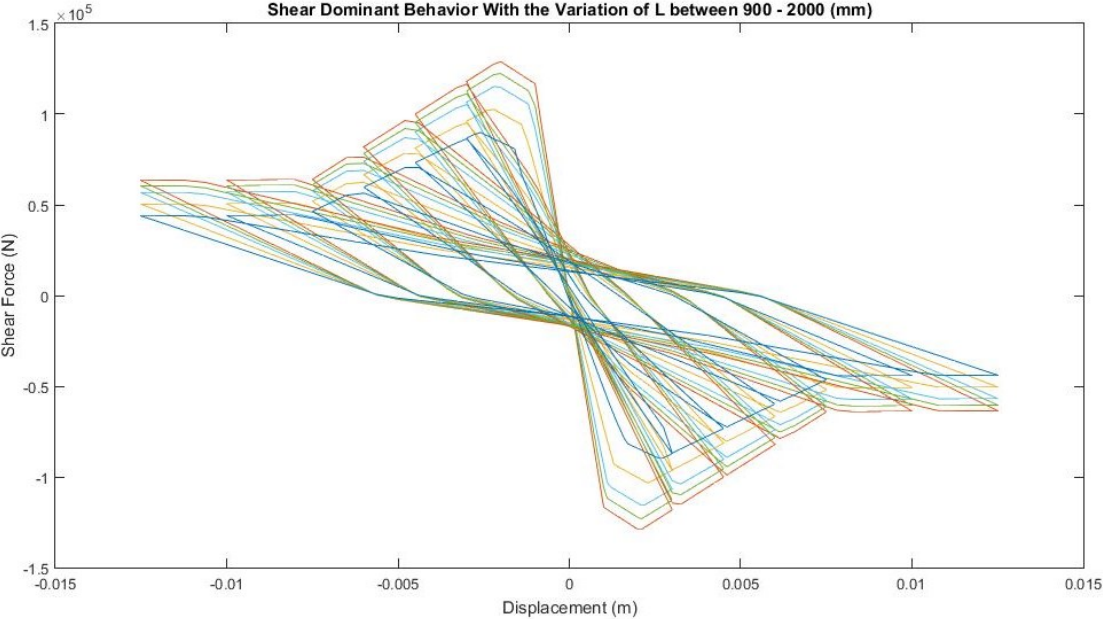


Figure A-2: Shear force vs displacement with length variation

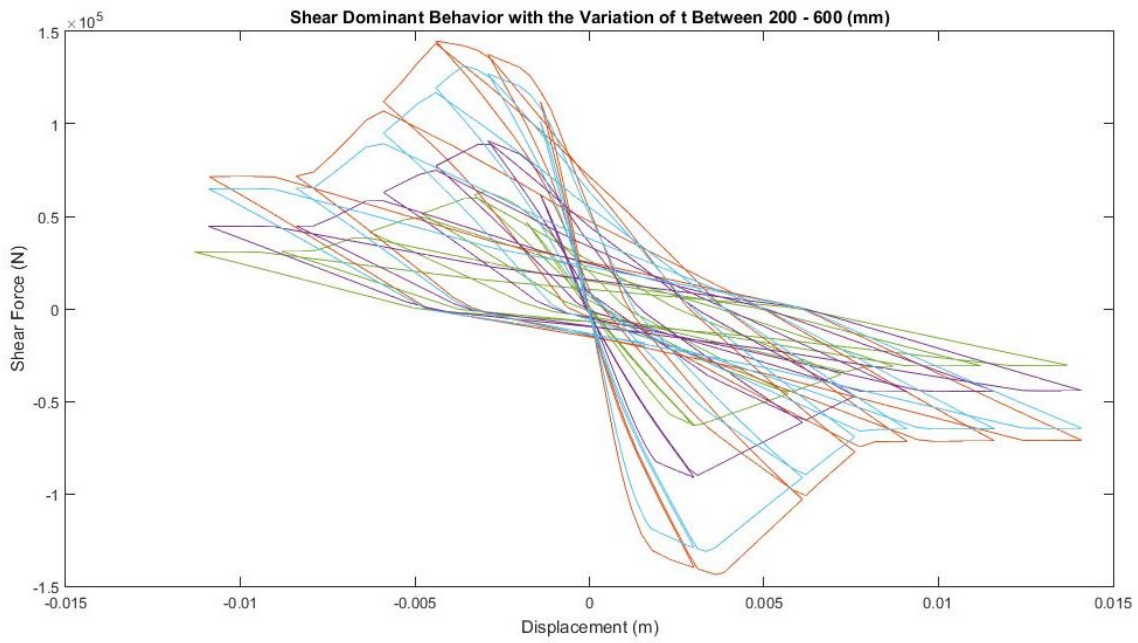


Figure A-3: Shear force vs displacement with thickness variation

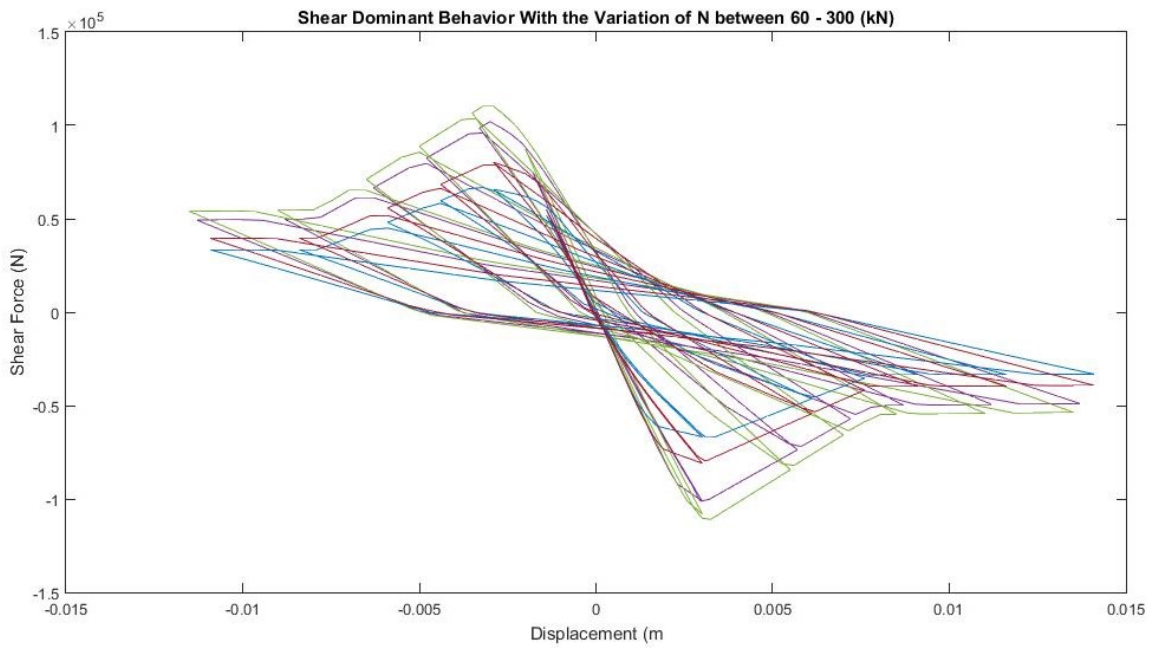


Figure A-4: Shear force vs displacement with vertical force variation

Cyclic Response for Piers with Dominant Flexural Failure

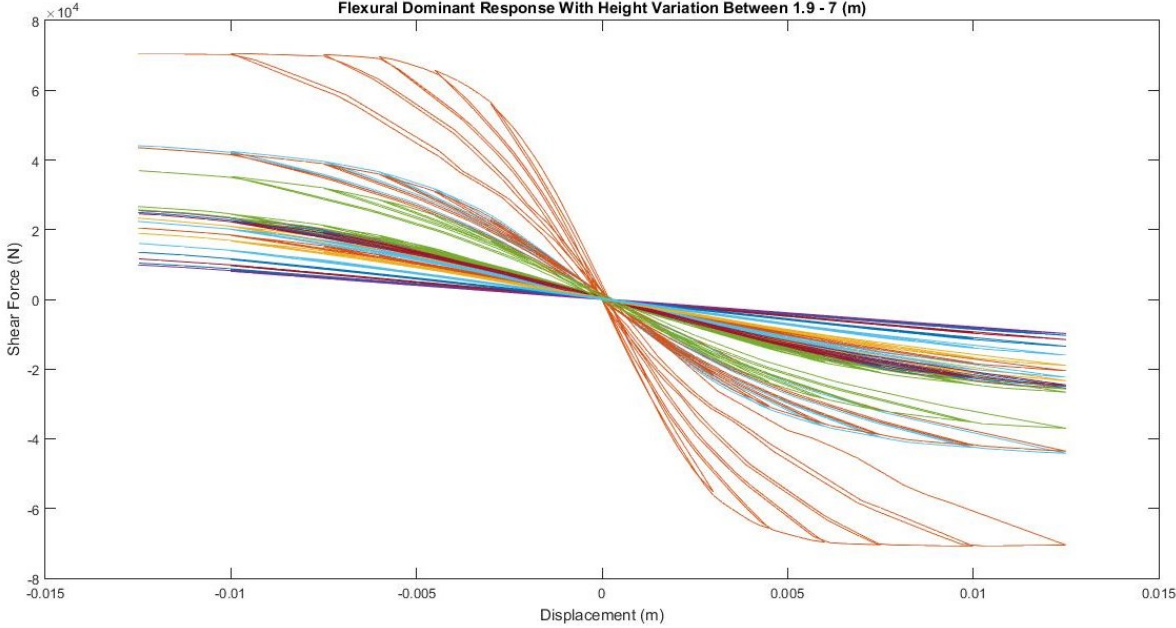


Figure A-5: Shear force vs displacement with height variation

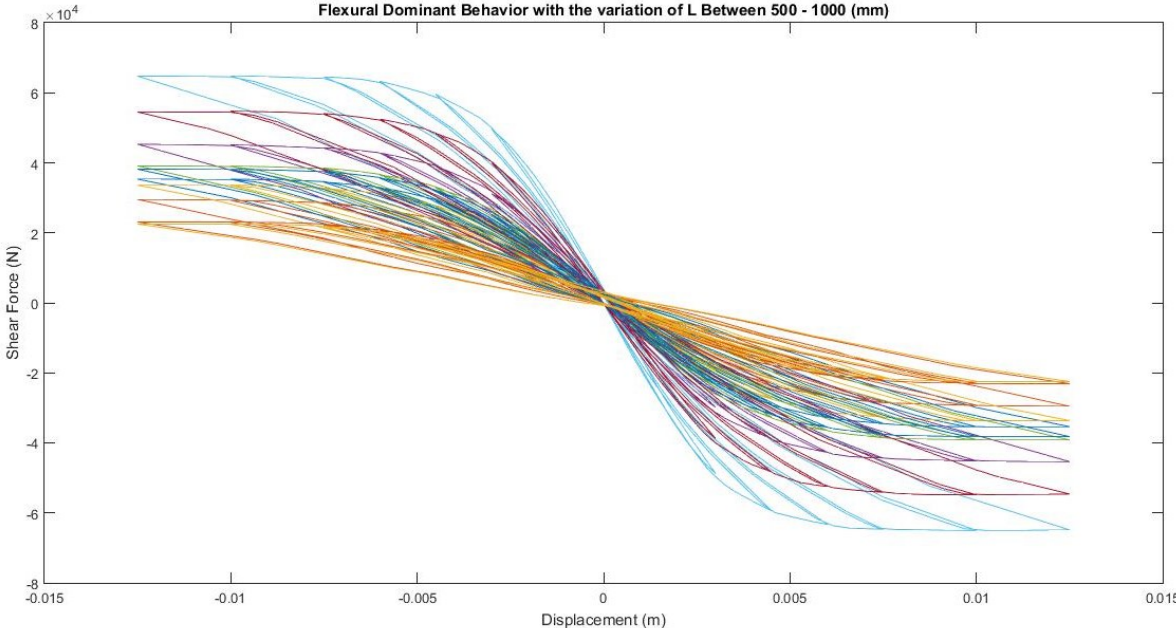


Figure A-6: Shear force vs displacement with length variation

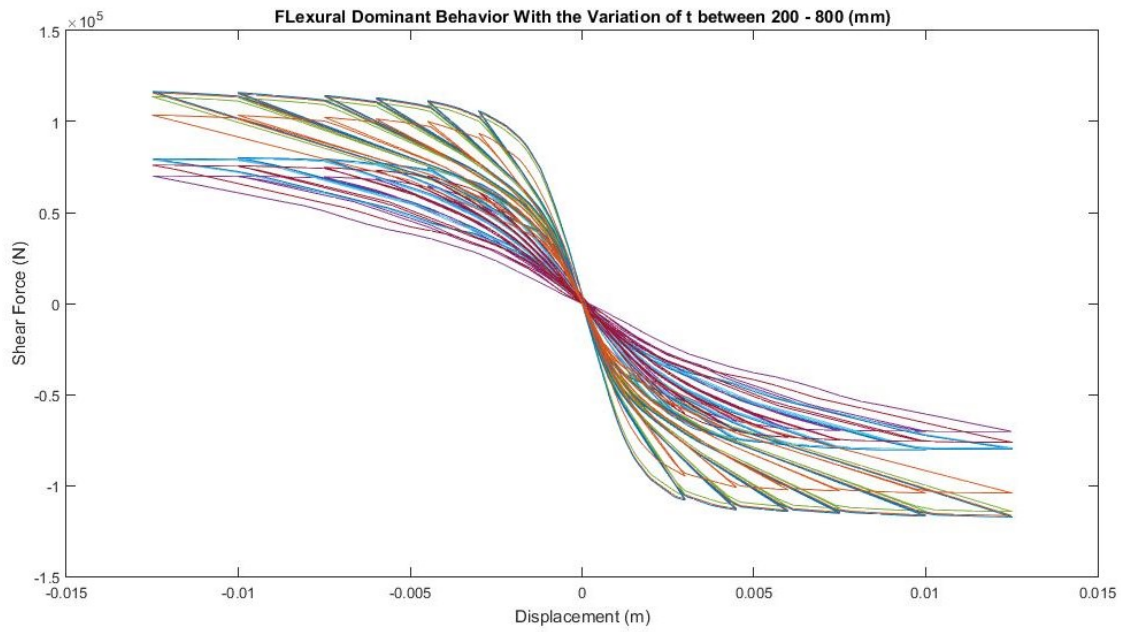


Figure A-7: Shear force vs displacement with thickness variation

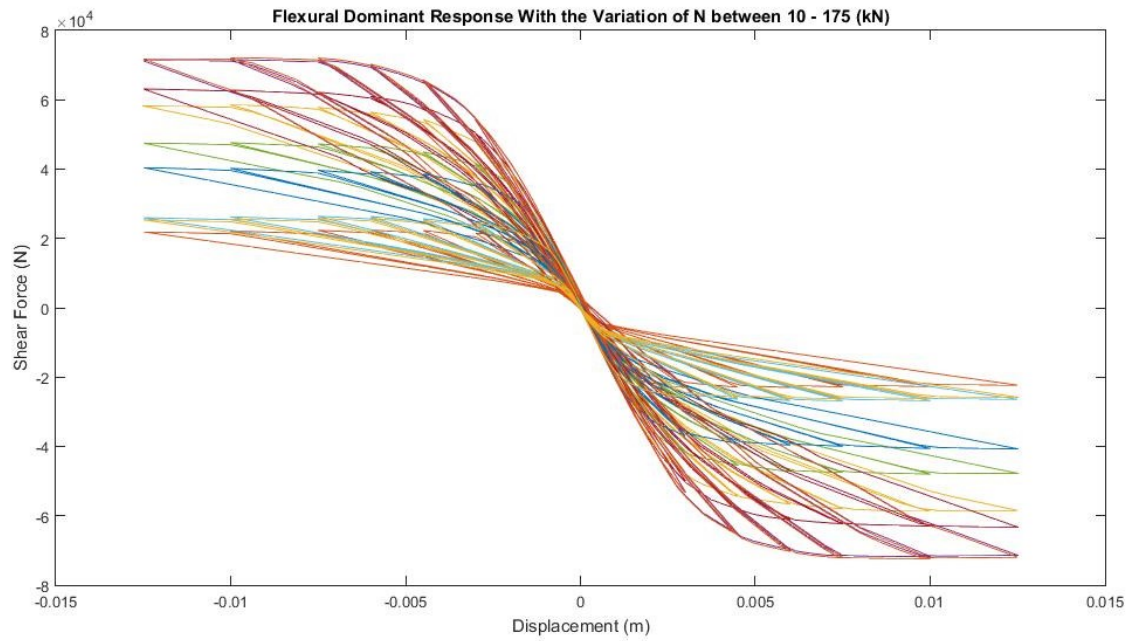


Figure A-8: Shear force vs displacement with vertical force variation

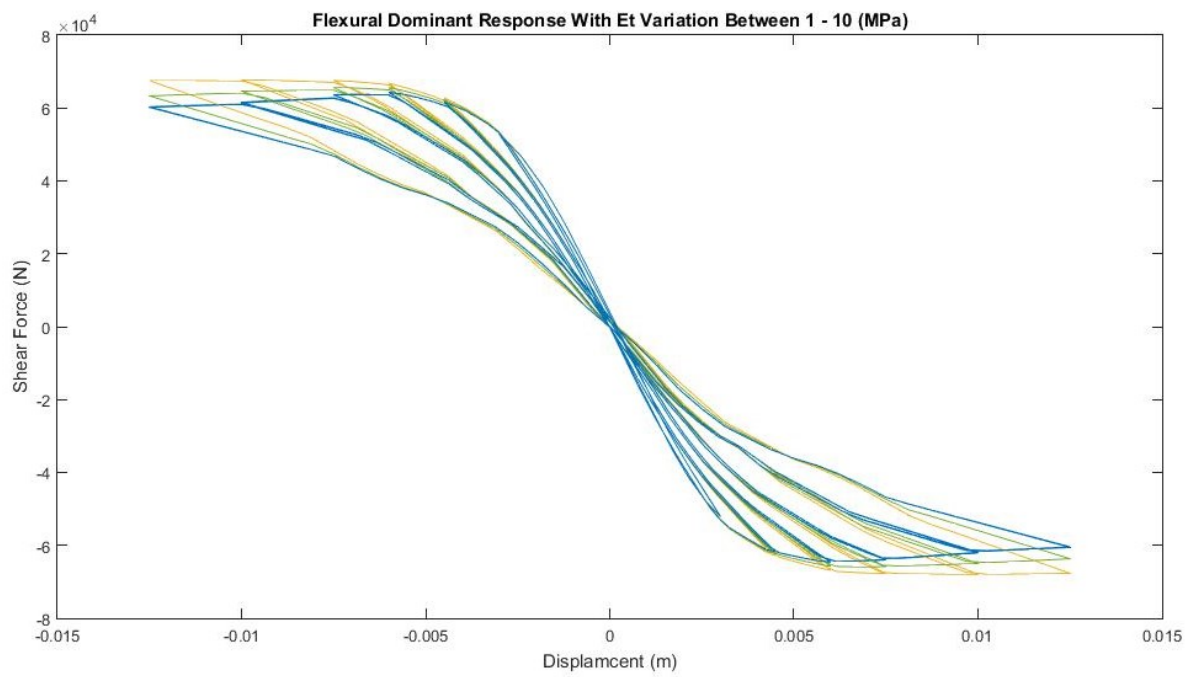


Figure A-9: Shear force vs displacement with tensile modulus variation